

# CFD analysis of current drag on the Floating Power Plant platform P80

Master thesis

Daniel Rothwell Pedersen & Martin Kirk Hoffmann

Structural and Civil Engineering

7 June 2019



**AALBORG UNIVERSITY**  
STUDENT REPORT





**AALBORG UNIVERSITY**  
STUDENT REPORT

**School of Engineering and Science**

Study Board of Civil Engineering

Thomas Manns Vej 23

9220 Aalborg Øst

[www.en.engineering.aau.dk](http://www.en.engineering.aau.dk)

**Title:**

CFD analysis of current drag on the Floating Power Plant platform P80

**Project type:**

Master thesis

**Project period:**

February 2019 - June 2019

**Members:**

Daniel Rothwell Pedersen  
Martin Kirk Hoffmann

**Supervisors:**

Morten Kramer  
Claes Eskilsson  
Sarah Thomas

**Total number of pages: 60**

**Submitted: June 7, 2018**

**Abstract:**

This report concerns drag forces acting on a new design of a semi-submersible, combined wave energy converter and wind turbine generator by Floating Power Plant. The functionality of the platform depends on its orientation towards incoming waves, as the mooring turret enables the platform P80 to rotate freely. It is therefore of interest to determine the current forces effect on the orientation of the P80.

The P80 has been the subject of CFD analysis to investigate the current induced forces acting on the structure. Full scale simulations have been performed at  $Re \approx 50e6$ . A main outcome of this report is drag coefficients in line with and transverse to the current direction for different current angles of attack, in order to determine the yawing moment created by the current.

Experiments have been performed in the flume at AAU on small scale models of a floating power plant. Results from these experiments have been used to validate the CFD model, which is used for determining current induced drag forces.

Other outcomes are current induced forces on a model scale of a FPP and a single Leg of this model. These forces are calculated with CFD and are both supported by experimental measurements. The experiments are performed as part of the project by the authors of this report and presented in detail in this report.

## Resume

Denne rapport omhandler påvirkningen af dragkræfter på et nyt design af en flydende, kombineret bølgegenerator og vindturbin fundament af Floating Power Plant. Funktionaliteten af platformen P80 afhænger af dens orientering i forhold til bølgeretningen, da den frit kan rotere om forløjningspunktet. Det er derfor nødvendigt at bestemme strømningens indvirkning på orienteringen af P80.

P80'eren er blevet undersøgt via CFD analyser for at undersøge de virkende strømningsskræfterne på strukturen. Fuldskala simuleringer er blevet kørt ved Reynolds tal på  $Re \approx 50e6$ . Et nøgleresultat af denne rapport er drag koefficienter, som sammenfalder med retningen af strømningen og ortogonalt på samme, når strømningens retning angrebsvinkel ændres, med henblik på at bestemme krøjningsmomentet, som strømningen forudsager.

Eksperimenter er blevet lavet i renden på AAU på nedskalerede modeller af en floating power plant. Resultater fra disse eksperimenter er blevet anvendt til at validere CFD modellen, som er anvendt til at bestemme dragkræfter forårsaget af strømningen.

Andre udfald af projektet inkluderer strømningsskræfter på en nedskaleret model af en floating power plant og et af dens ben. Disse kræfter er beregnet ved brug af CFD og er begge understøttet af eksperimentale målinger. Eksperimenterne er udført som en del af dette projekt af forfatterne til denne rapport og er beskrevet i rapporten.

## **Preface**

This Master's thesis in Structural and Civil Engineering at Aalborg University is written by Daniel Rothwell Pedersen and Martin Kirk Hoffmann. The thesis consists of a main report and appendices.

The authors of this report would like to thank our supervisors Morten Bech Kramer from AAU/Floating Power Plant, Claes Eskilsson from AAU and Sarah Thomas from Floating Power Plant for their excellent supervision and input to this project. We are also very grateful to Floating Power Plant for providing not just one, but two desktop computers for CFD simulations. We would also like to thank technician at the AAU laboratory Nikolaj Holk and co. for their help in providing and setting up equipment for our experiments in the flume at AAU.

---

## Notation table

$\varepsilon$	Turbulent dissipation rate
$\kappa$	von Karman constant
$\rho$	Density
$\mu$	Dynamic viscosity
$\mu_t$	Turbulent viscosity (Eddy viscosity)
$\nu$	Kinematic viscosity
$\tau_{ij}$	Reynolds stress
$\omega$	Specific turbulence dissipation rate
$A_{ref}$	Reference area
$B$	Fitting constant for logarithmic velocity profile
$C_\mu$	Empirical constant
$C_{D,x}, C_{D,y}$	Drag coefficient in current direction and transverse to same in the horizontal plane ( $x$ and $y$ )
$D$	Diameter
$f_x, f_y, f_z$	Forces in $x, y, z$ -direction respectively
$F_x, F_y, F_z$	Mean forces in $x, y, z$ -direction respectively
$h$	Water depth
$k$	Turbulent kinetic energy
$\ell$	Turbulence length scale
$m_x, m_y, m_z$	Moments around $x, y, z$ -axis respectively
$M_x, M_y, M_z$	Mean moments around $x, y, z$ -axis respectively
$N_z$	Mesh refinement scale for blockMesh
$Q$	Current generation capacity in %
$S$	Source term
$u_\tau$	Shear velocity
$u, v, w$	Velocity in $x, y, z$ -direction respectively
$\mathbf{u}$	Velocity vector
$u', v', w'$	Fluctuating components in $x, y, z$ -direction respectively
$\mathbf{u}'$	Fluctuating components velocity vector
$U, V, W$	Mean velocity in $x, y, z$ -direction respectively
$\mathbf{U}$	Mean velocity vector
$y^+$	Normalised distance normal to surface
Re	Reynolds number

---

# Contents

<b>1</b>	<b>Introduction</b> .....	<b>1</b>
1.1	Project structure	4
<b>2</b>	<b>CFD</b> .....	<b>5</b>
2.1	Governing equations	5
2.2	OpenFOAM	5
2.3	Meshing	6
2.4	General settings	7
<b>3</b>	<b>Current profile in AAU flume</b> .....	<b>9</b>
3.1	Flume description	9
3.2	Setup and data processing	10
3.3	Current Data Analysis	12
3.4	Summary	15
<b>4</b>	<b>Experimental force measurements</b> .....	<b>17</b>
4.1	Setup and equipment for force measurement	17
4.2	Data analysis	19
4.3	Summary	23
<b>5</b>	<b>Numerical validation - Model Leg</b> .....	<b>25</b>
5.1	Computational domain	25
5.2	General flow description	27
5.3	Convergence analysis	30
5.4	Sensitivity analysis	32
5.5	Experiment comparisons	36
5.6	Summary	38
<b>6</b>	<b>Numerical validation - Full Model</b> .....	<b>41</b>
6.1	Computational domain and settings	41
6.2	General flow description	43
6.3	Convergence analysis	45
6.4	Transient analysis	45
6.5	Experiment comparisons	47
6.6	Summary	47

---

---

<b>7</b>	<b>Analysis of FPP P80</b> .....	<b>49</b>
7.1	Computational domain	49
7.2	General flow description	52
7.3	Results	54
7.4	Estimation of drag coefficients	56
<b>8</b>	<b>Conclusion</b> .....	<b>59</b>
8.1	Further work	59
	<b>References</b> .....	<b>62</b>

**I****Appendices**

<b>A</b>	<b>Theory</b> .....	<b>65</b>
<b>B</b>	<b>Numerical settings</b> .....	<b>71</b>
<b>C</b>	<b>Flume velocity profiles</b> .....	<b>73</b>
<b>D</b>	<b>Force sensor</b> .....	<b>79</b>
<b>E</b>	<b>Forces from experiments</b> .....	<b>81</b>
<b>F</b>	<b>Simulation results</b> .....	<b>83</b>
<b>G</b>	<b>Drag coefficients from DNV</b> .....	<b>93</b>

---

# 1. Introduction

In a world where climate change lies higher than ever on the global agenda, one of the larger CO<sub>2</sub> emission sources continues to be the power production sector, where fossil fuels long have been the primary source of power. This is a tendency which, according to UN Environment, 2019, must be addressed immediately to reduce the severity of the impact of future climate changes, as power demand also increases due to a predicted rise in global population.

As an answer to this call, much focus has been shifted to producing alternative sources of energy. In particular renewable energy sources such as wind turbine generators (WTG) are experiencing a rise in production, see Figure 1.1. Yet, this tendency has only recently come into effect, as can also be seen when comparing the renewable energy sources to the fossil fuels; coal, oil and gas [IEA, 2019].

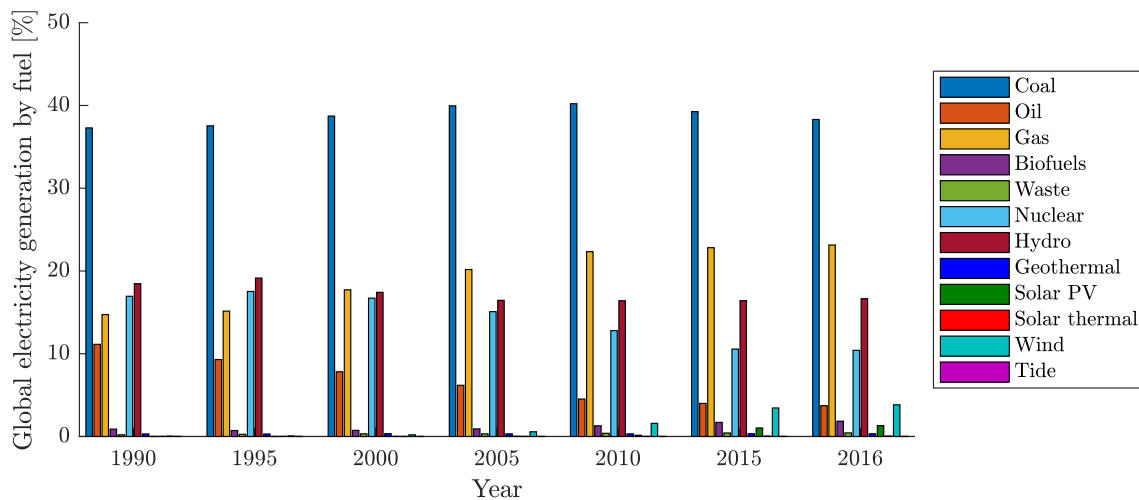


**Figure 1.1:** Global electricity generation by fuel. [IEA, 2019]

In Denmark, WTG contributed to 42 % of the country's electricity supply in 2016 [IEA, 2019] with more wind farms in the pipeline [Energistyrelsen, 2019]. This is in large due to the shallow waters in the North Sea that make it possible to install fixed foundations for offshore WTG directly into the seabed in the shape of e.g. monopiles. Monopiles can be placed in water depths of up to 40-50 m [EWEA, 2013]. But in order to exploit the potential of extracting energy at larger water depths, research has started to expand its attention to include floating structures.

Today only one commercial floating offshore wind farm is in operation, namely the 30MW Hywind Scotland spar-buoy [Clean Technica, 2018], but many more are under development [Carbon Trust, 2015]. One of these new floating offshore structures are being developed by Floating Power Plant.

At Floating Power Plant, research is ongoing into a new concept of extracting energy from a combined wave energy converter (2-3.6 MW) and wind turbine generator (5-8 MW) on a semi-submersible platform of the same name as the company; a floating power plant (FPP), see Figure 1.2. The FPP is designed in such a way that the platform is allowed to rotate freely around the mooring turret located at the fore part of the hull. This enables the platform to face the direction of the

incoming waves. The wind turbine is also placed at the fore part of the hull in a bearing, which enables it to rotate independently of the platform. The platform beyond the fore part of the hull consists of the wave energy converters (WEC) and heave plates for stability, see Figure 1.2. A few significant prospected advantages of the FPP compared to other floating foundations are given below.

- Combining wind and wave energy makes it possible to access new geographical markets where the wave power exceeds 25 kW/m and surpassing the capacity of other competitive floaters.
- The turret mooring is disconnectable, enabling easy relocation of the platform.
- FPP generates a more stable power source, as both wind and waves contribute to the power generation, making it easier to predict the power load.
- The wave absorbers provide safer access for maintenance vessels behind the floating structure. The uptime for the power supply is thereby increased. [FPP, 2019]

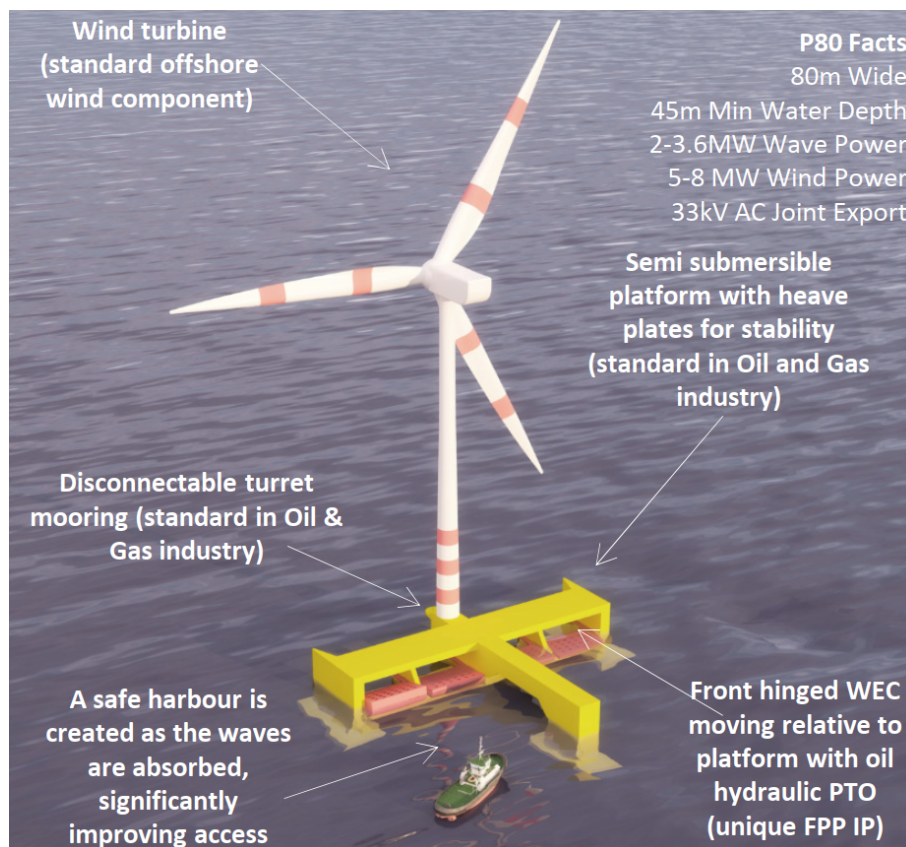


**Figure 1.2:** Floating Power Plant's P80. [FPP, 2019]

The FPP is not yet put into production as further research is still needed on this new concept. One of the research areas concerns the orientation of the structure. The FPP should always be facing towards the incoming waves in order to enable its wave absorbers to utilise its wave energy generation and the safer access potential behind the structure. For that reason, it is relevant to examine whether the current forces will cause the FPP to face the incoming current, instead of the incoming waves. The wind turbine would also contribute with a yawing moment. This contribution

will however have little influence on the platform direction due to its position close to the mooring turret and the design of the connection piece.

This report concerns the current generated forces acting on the FPP from different current angles of attack (current directions). In particular, the yawing moment, and thereby the forces acting in the current direction and transverse to same, are of interest. The scope of this report is thus formulated as:

**Estimate the current induced drag on a Floating Power Plant P80 from multiple current directions.**

Wind, wave and current forces will all influence the orientation of the Floating Power Plant P80 (hereafter referred to as: P80). In reality these interactions will be coupled. This report will only be considering the loads from a steady current from different directions. Wind and wave forces will not be investigated.

The fluid dynamic problem that this report aims to solve consists of a constant current in water acting on a stationary structure. It is thereby also assumed that the wave absorber paddles are set in a fixed position, and the whole structure is considered a single, solid body. For this reason, it is assumed that the flow problem can be solved as a single-phase, incompressible, steady state solution of a Newtonian fluid.

The design of the P80 itself is complex and differs from other floating structures. Therefore, forces on the structure will be determined by numerical analysis in the form of computational fluid dynamics (CFD), because of its ability to solve large complex problems. The use of CFD analysis has grown exponentially since 2006 because of this [Rønby, 2019].

In short, CFD is used to calculate and visualise the behaviour of fluids and their effect on structures. This is done based on a governing equation system for the flow problem, see section 2.1. A CFD analysis entails the following three steps:

1. **Pre-processing:** Concerns breaking down a physical domain into finite volumes or cells, which collectively are known as a mesh. Also, boundary and initial conditions are applied in this step.
2. **Solving:** The properties of each cell, e.g. velocities and pressure, are calculated from the relevant equations for the fluid problem. The calculated values are logged and can be interpreted in the final step.
3. **Post-processing:** The user interprets the flow properties. This can for example be calculating forces from pressure in cells edging onto a structure, or visualising streamlines of the flow.

The software OpenFOAM will be used for the CFD analysis.

The results of a CFD analysis is very dependent on the quality of the input. Thus, in order to verify that feasible results are obtained in the CFD analysis, experimental results on small scale models of an FPP are compared to CFD analysis of the same small scale models.

---

## 1.1 Project structure

This report includes CFD analysis of the the P80 to determine the current induced drag acting on the structure. CFD analysis supported by experimental work is performed on small scale models of a FPP in order to obtain an understanding of the flow dynamics of a steady current and to validate the use of CFD on the P80 platform.

Experiments on small scale models provided by Floating Power Plant are performed in the flume at Aalborg University (AAU). This is done in order to determine the forces acting on the models, when subjected to a steady current. The experiments are performed on a model scale of a FPP and a single Leg of this model (hereafter referred to as: Full Model and Model Leg respectively).

The flow field in the flume is investigated initially at certain locations in the flume by the authors of this report. The flow field is in turn used to determine the optimal location for model tests as well as serving as input to the CFD model.

Numerical models of the experiments are set up in OpenFOAM. The numerical models are made to resemble a part of the flume used for the experiments, and are calibrated to match the experimental results to a satisfactory extent.

Settings and parameters from the validated small scale CFD models are used to calculate the effect of currents on the P80, though in a larger domain resembling open water conditions. Forces acting on the structure are calculated in the simulations. Coefficients for current induced drag are calculated from the simulation results.

---

## 2. CFD

This chapter concerns the program and tools used in this report to build the CFD models. This includes the overall structure of the program, and a short presentation of how fluid dynamic problems are processed in the program.

### 2.1 Governing equations

The flow is solved as a single-phase, incompressible, steady state Newtonian fluid. The equation system that governs this flow problem are listed in equations (2.1)-(2.4). Appendix A shows how these equations are acquired from the made assumptions.

As only the mean flow properties are of interest for this project, the turbulence is modelled with the Reynolds-averaged Navier-Stokes (RANS) equations, see (2.2)-(2.4).

$$\text{Continuity} \quad \rho \operatorname{div}(\mathbf{U}) = 0 \quad (2.1)$$

$$x \text{ momentum} \quad \rho \operatorname{div}(U\mathbf{U}) + \rho \operatorname{div}(\overline{u'\mathbf{u}'}) = -\frac{\partial P}{\partial x} + \mu \operatorname{div}(\operatorname{grad}(U)) + S_{Mx} \quad (2.2)$$

$$y \text{ momentum} \quad \rho \operatorname{div}(V\mathbf{U}) + \rho \operatorname{div}(\overline{v'\mathbf{u}'}) = -\frac{\partial P}{\partial y} + \mu \operatorname{div}(\operatorname{grad}(V)) + S_{My} \quad (2.3)$$

$$z \text{ momentum} \quad \rho \operatorname{div}(W\mathbf{U}) + \rho \operatorname{div}(\overline{w'\mathbf{u}'}) = -\frac{\partial P}{\partial z} + \mu \operatorname{div}(\operatorname{grad}(W)) + S_{Mz} \quad (2.4)$$

### 2.2 OpenFOAM

The program used to set up CFD models is the open source program OpenFOAM [Weller et al., 1998]. The software was released in 2004 by OpenCFD Ltd. In 2012 Engineering System International (ESI) acquired OpenCFD Ltd and has actively developed the software since, with a new release published every six months [esi, 2019]. The version used in this project is OpenFOAM v1806.

OpenFOAM is a library containing scripts developed in C++ for the finite volume method to discretise partial differential equations. These scripts can be categorised as `solvers`, which solve the continuum mechanic problem, and `utilities` which are used to pre- and post-process the data. Many different `solvers` have been developed and implemented in the program e.g. incompressible and compressible flow solvers. The object-oriented code language also makes it possible for users to develop their own `solvers`.

As part of the post-processing the third-party software ParaView is used to visualise the mesh and flow in a three dimensional space [Kitware, 2019].

---

## 2.3 Meshing

The discretisation of the fluid domain is done using the meshing tools `blockMesh` and `snappyHexMesh`. These tools are a part of the OpenFOAM framework.

The initial hexahedral background mesh of the fluid domain for the investigated flow problem is initially built with the utility `blockMesh`. For this application to run, an input file is needed, in which the key nodes for the blocks defining the domain are specified. Furthermore, the division of the blocks into cells and grading of the cell size in certain directions, specified by an expansion ratio, are defined in `blockMesh`, see Figure 2.1(a).

`snappyHexMesh` is a hexahedral dominant mesh tool using a octree-based approach to refine the mesh [Aldegunde, J Pombo, and Garcia Loureiro, 2019], and is used to implement the model into the domain and refine the mesh in regions of interest. Specifying the model as an .STL file format enables `snappyHexMesh` to register cells upon the geometry.

Cell vertices are fitted to the geometry surface using the feature `snapControls`. The refinement of the mesh is mainly governed by two features, `refinementLevel` (RL) and `addLayers`, illustrated in Figure 2.1(b). The `refinementLevel` describes the amount of subdivisions applied to a cell in all three directions. The cells defined with `blockMesh` correspond to a `refinementLevel` of zero. As a consequence of cell fitting and refinement, some hexahedral cells are altered into polyhedrals, which are also manageable in OpenFOAM. The feature `addLayers` is used for further refinement near the model surface to resolve the boundary layers without increasing the amount of cells significantly. The degree of refinement is determined by the dimensionless parameter  $y^+$ , which is used to describe the normalised distance between the surface and the closest cell centre. The  $y^+$  parameter is described in more detail in Appendix A. The feature creates a thin film around the model surface, which is then divided into a specified amount of layers normal to the surface. Consequently the cells in these layers will have a high aspect ratio, see Figure 2.1(b).

Many settings have been adjusted in order to make `snappyHexMesh` build the mesh properly. As seen in Figure 2.1(c), the bottom left corner of the Model Leg illustrates that layers are not resolved perfectly in all cases.

$$\frac{\Delta x_e}{\Delta x_s} = \text{Expansion ratio}$$

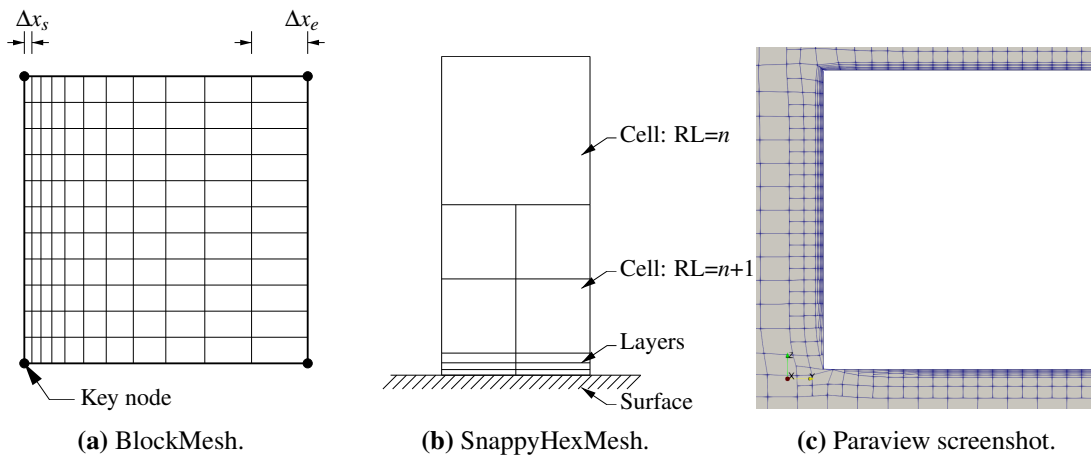


**Figure 2.1:** Illustration of features in `blockMesh` and `snappyHexMesh`.

## 2.4 General settings

The SIMPLE algorithm is used in this project to solve the flow field. This is done by using the solver `simpleFoam` which is a solver for single-phase, incompressible, steady state, turbulent flows and is therefore assumed to be applicable for this study.

Throughout the project, the  $k - \omega$  SST turbulence model is used.  $k - \omega$  SST is a standard model used in hydrodynamic modelling. The  $k - \omega$  SST model is used to compute the turbulent viscosity,  $\mu_t$ , along with the turbulent kinetic energy per unit mass,  $k$ , and the rate of dissipation of turbulence kinetic energy,  $\omega$  [Menter, 1994]. These parameters are inputs to the Boussinesq expression, which is used to calculate the Reynolds stresses [Versteeg and Malalasekera, 2007]. Further description of this turbulence model is present in Appendix A.2.

For the integration of the transport equation the Gauss's divergence theorem is used, see Appendix A. The diffusion terms are discretised with a central differencing scheme. For the convection terms upwind schemes are used, where the velocity equations uses a linear upwind scheme. The schemes and solution settings used in this report are given in Appendix B.

Tool	Setting
Solver	<code>simpleFoam</code>
Simulation type	RAS
Turbulence model	<code>k-omega SST</code>
k-wall	<code>kLowReWallFunction</code>
nut-wall	<code>nutUBlendedWallFunction</code>
omega-wall	<code>omegaWallFunction</code>

**Table 2.1:** Computational settings.

In Table 2.2 the fluid properties for the experimental and open water conditions are shown.

	Experiments	Open water
Density of water, $\rho$	1000 kg/m <sup>3</sup>	1025 kg/m <sup>3</sup>
Dynamic viscosity of water, $\mu$	1.00e-3 Pa/s	1.08e-3 Pa/s

**Table 2.2:** Fluid properties.



## 3. Current profile in AAU flume

Laboratory experiments have been performed in the flume at AAU for the purpose of validation of the CFD analysis.

The first part of the experiments examines the current generated velocity field in the flume through a series of test measurements. This is done to determine parameters of the undisturbed flow in the flume, which will serve as input to the CFD analysis, and to find the most ideal location for the model tests. The parameters concerned are the shape and magnitude, i.e. the velocity profile, in the flume, and the turbulent parameters  $k$  and  $\omega$ . It will be mainly the velocity profile acting parallel to the flume length, shown as the  $x$ -direction in Figure 3.1, that will be examined in this chapter.

AAU also have an interest in knowing the velocity profiles at different locations in the flume for future experiments and to check that changes made to the flume provide the expected velocity field, as determined in the report by Christiansen and Lausten, 2017. Figures of the velocity profiles at all test locations shown in Figure 3.1 are shown in Appendix C.

### 3.1 Flume description

The layout of the flume at AAU is shown in Figure 3.1. The flume is 1.5 m wide, has a height of 1.5 m and ranges 13 m from the current inlet to the absorbers. The origin of the coordinate system for the experiments is placed at the current inflow, with  $x$  and  $y$  in the longitudinal and transverse directions respectively, and  $z$  indicating the vertical distance from the bottom of the flume. The pump driving the water flow has a maximum driving frequency of 50 Hz (100 %), and will be shown as %-capacity of the current generation,  $Q$ .

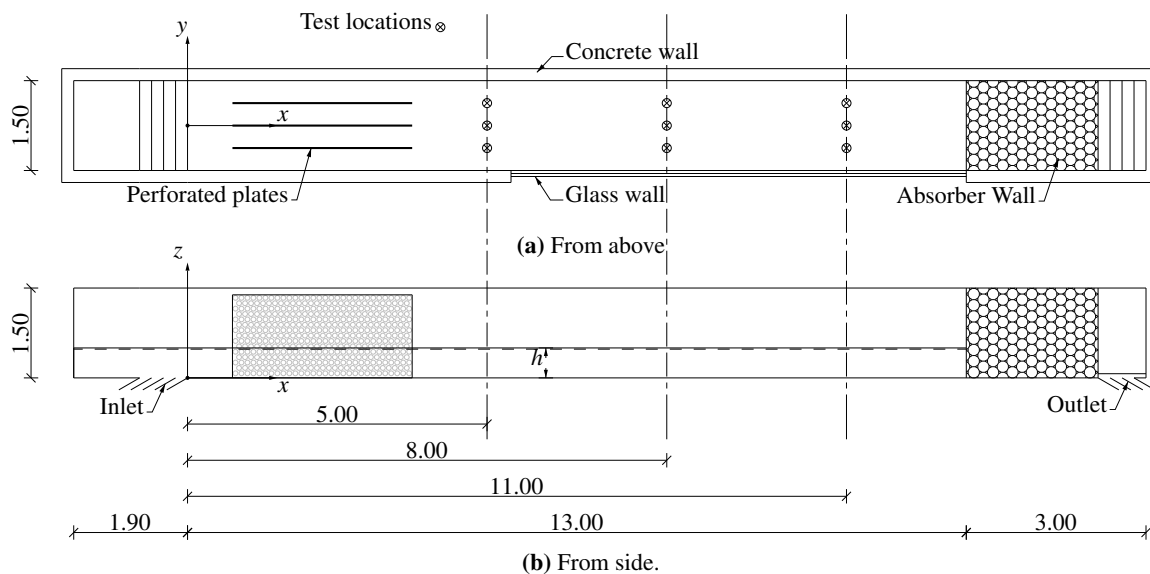


**Figure 3.1:** Flume layout and dimensions. Positions of test locations are also shown.

### 3.2 Setup and data processing

Current measurements have been carried out for nine different locations in the  $xy$ -plane of the flume, shown in Figure 3.1. In total, 25 experiments were performed which are listed in Appendix C. For every experiment, the velocity is measured every 4 cm throughout the water depth while the pump is running continuously.

The current velocity is measured with the Vectrino Velocimeter Cable Probe from Nortek A/S [NORTEK, 2019], see Figure 3.2. The device measures the velocities in the  $x$ -,  $y$ - and  $z$ -directions ( $u$ ,  $v$  and  $w$ ), 5 cm below the tip of the device with a sampling rate of 25 Hz. The following velocities will also be presented as being at the height 5 cm below the tip of the device. The coordinate axis for the Vectrino is orientated in the same manner as for the flume, see Figure 3.1.

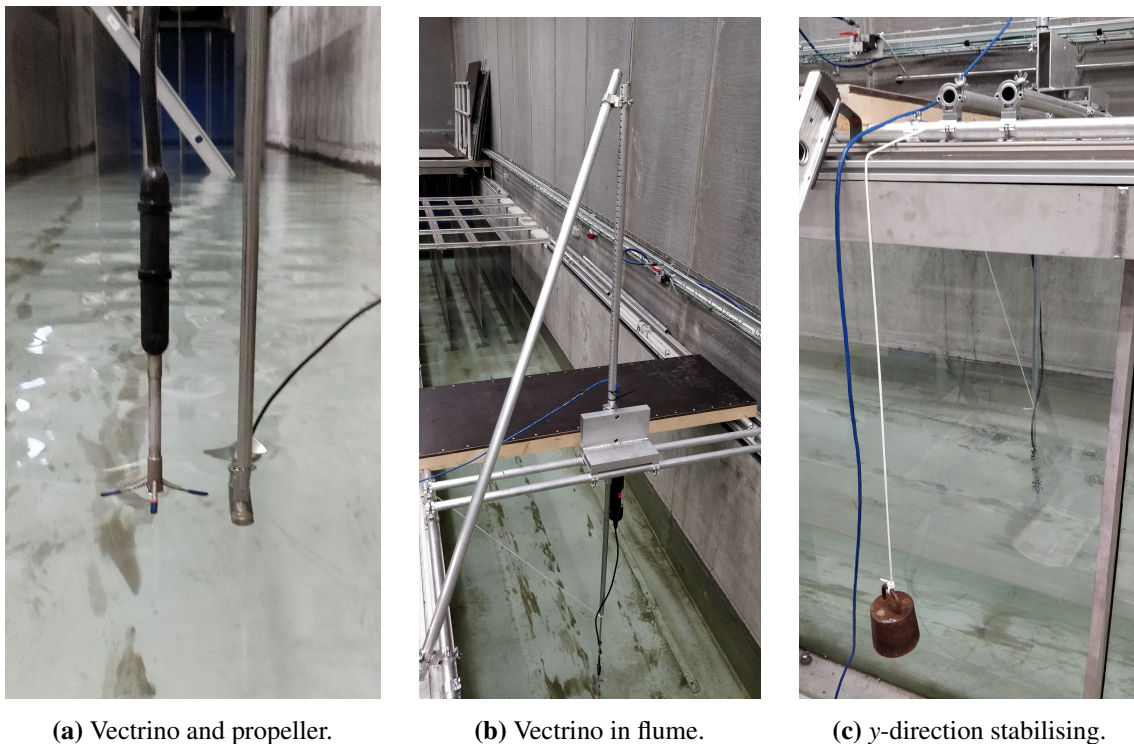


**Figure 3.2:** Vectrino, propeller and stabilising setup. Rod mounted to the top of the setup to stabilise the  $x$ -direction and a load attached to a string connected at a lower point on the setup to stabilise in the  $y$ -direction.

To minimise sources of error, the following considerations and modifications have been carried out for the experimental setup.

- Steady state flow should be achieved for data series where a mean value is desired. To ensure this, the time response was analysed to see for how long the pump should be running before the flow reaches a steady velocity. From Figure 3.3 it is judged that the flow is steady after the pump has been running for approximately 180 s.
- Attempts to minimise vibrations of the setup have been made by stiffening the Vectrino probe. A truss is attached in the  $x$ -direction and gravity load is applied in  $y$ -direction, see Figure 3.2.

- Data recorded through Vectrino's own software and cables directly plugged to a computer USB-port has been compared with data recorded in WaveLab [Lykke Andersen, 2018] through an analog filter to check for noise differences. The difference between the two signals are very small and is assumed to have no influence on the results, see Figure 3.4.
- The velocities measured with the Vectrino device is compared with a mechanical propeller flowmeter, which is shown in Figure 3.2 (a). This is done to verify the Vectrino measurements, see Figure 3.6. The measurements with the propeller were conducted over a period of 40 s.
- The orientation of the device has been placed so that the measurements in the  $x$ -direction in the Vectrino device are parallel with the flow direction. This is secured by visual examination and by comparing the velocity resultant of the  $x$ - and  $y$ -direction with the velocity in the  $x$ -direction, as these should be the same size.
- Powder was frequently added to the water in the flume, as the Vectrino uses the reflected signal from particles in the water to measure velocities.

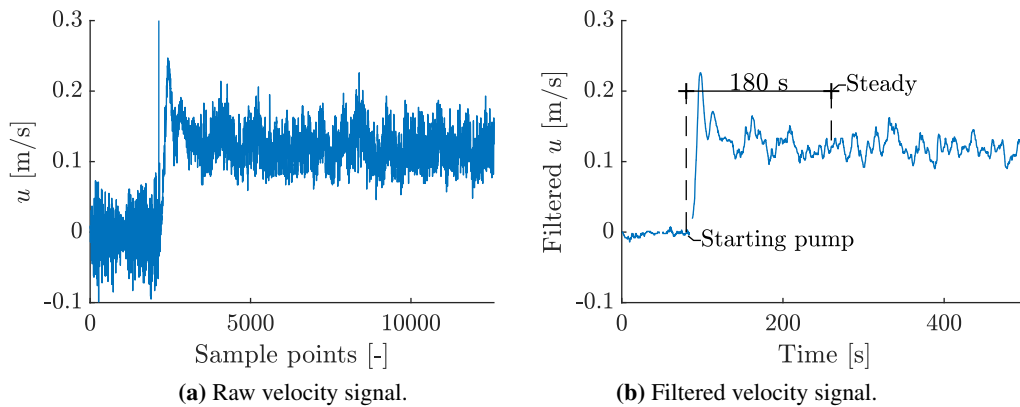


**Figure 3.3:** Steady state analysis.

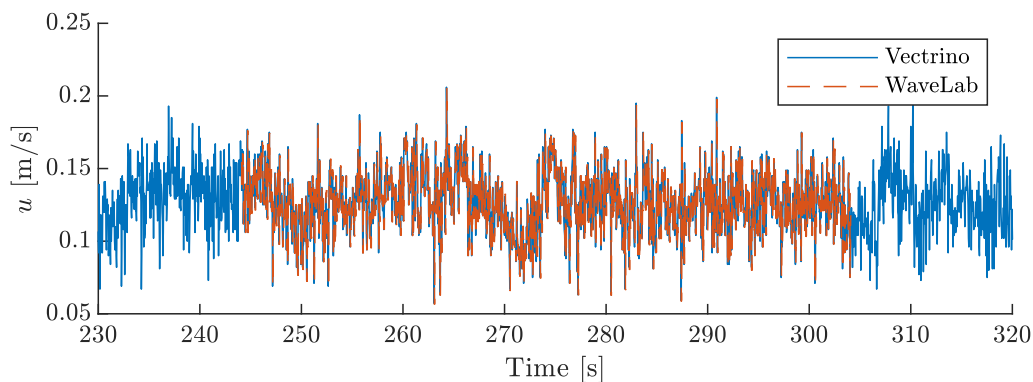
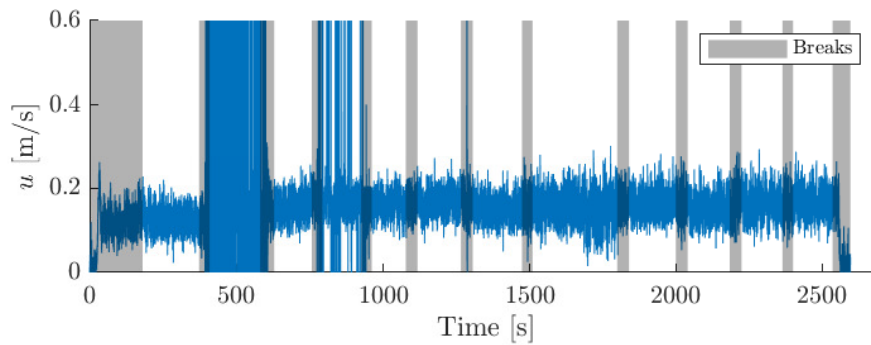


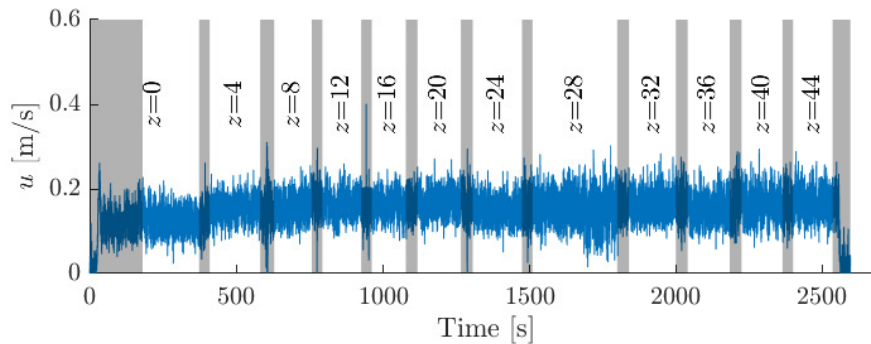
**Figure 3.4:** Comparison of WaveLab and Vectrino results.

When altering the  $z$ -position of the Vectrino, it is assumed that no major disturbances to the flow are caused. The time intervals where the  $z$ -position of the Vectrino is changed are logged and sorted when treating the data. The measuring duration at each  $z$ -position is minimum 60 s. The grey areas in Figure 3.5 indicate the time interval when the Vectrino's position has been adjusted, referred to as breaks. The measurements outside the breaks, are averaged to create a mean velocity at each  $z$ -position ( $U$ ,  $V$  and  $W$ ).

Some uncertainties were encountered, especially when the Vectrino was measuring 4 cm above the bottom of the flume. At this height the Vectrino consistently displayed a large number of voltage/velocity peaks outside of the specified range of the data collection, see Figure 3.5(a). This problem also occurred at other heights but to a lesser extent. Because of this issue, a range from  $-0.1$  to  $0.5$  m/s in the  $x$ -direction is defined to detect outliers. Measurements outside that range are filtered out and produce the corrected signal in the bottom of Figure 3.5. For the  $y$ - and  $z$ -direction the range was set from  $-0.3$  to  $0.3$  m/s and  $-0.1$  to  $0.1$  m/s respectively, the corrected signal for these directions are found in Appendix C.



(a) Unfiltered results.



(b) Range from  $-0.1$  to  $0.5$  m/s in the  $x$ -direction is applied.

**Figure 3.5:** Data filtering example. Shown data is for  $x = 5$  m,  $y = 0$  m,  $h = 0.5$  m and  $Q = 50$  %.

### 3.3 Current Data Analysis

The data obtained from the experiments is used to determine the velocity field in the flume and to calculate the flow properties of the current, i.e. the velocity profiles and turbulent parameters. The latter two elements are used as input in the CFD analysis.

#### 3.3.1 Velocity field

By assuming that flow in the flume corresponds to theory for flow over a flat plate, the critical Reynolds number,  $Re_{xcr} = Ux/\nu = 5e5$ . This means that a flow with a mean velocity of  $0.1$  m/s at

$x = 5$  m will be turbulent [Munson et al., 2013]. The flow for all experiments is thus expected to be turbulent and accordingly have a logarithmic relation between the velocity and the distance from the bottom surface of the flume. Based on this argument, the measured velocities are assumed to follow equation (3.1) [Versteeg and Malalasekera, 2007].

$$U = \frac{u_\tau}{\kappa} \ln(y) + D \quad (3.1)$$

The von Kármán constant is  $\kappa = 0.41$ . The parameters  $u_\tau$  and  $D$  are found in Table 3.1 and have been calculated by fitting a polynomial with the least squares method to the measured profiles, see Figure 3.6.

$Q$	50 %	75 %	100 %
$u_\tau$ [m/s]	0.0049	0.0083	0.0105
$D$ [m/s]	0.1960	0.3003	0.3736

**Table 3.1:** Parameters to determine velocities.

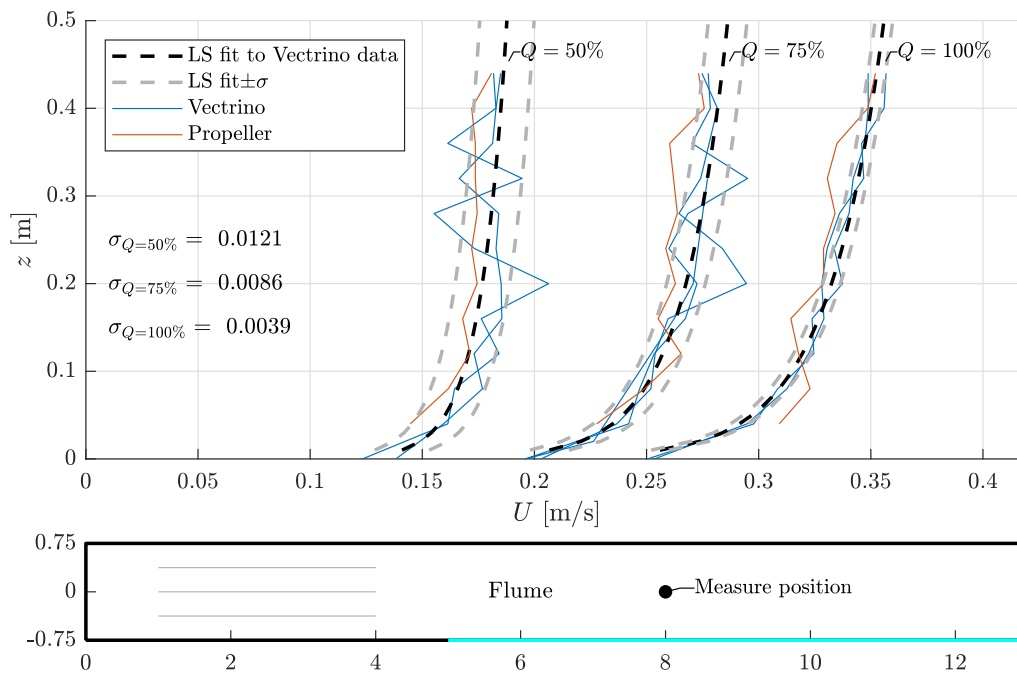


**Figure 3.6:** Least square fit of Vectrino velocity profiles.

As shown in Figure 3.6 the velocities in the centre at  $x = 8$  m are complying well with theory in that they follow a logarithmic shape. However, the fluctuations at 50% and 75% pump capacity are fairly noticeable, which is also seen from the increase in the standard deviation,  $\sigma$ .  $\sigma$  is calculated from the difference between the experimental mean velocities and fitted profile. A longer time logging at each  $z$ -position may have smoothed the velocity profiles.

From Figure 3.7 it can be seen that the velocity profiles are not the same across the cross-section of the flume. The current velocity near the concrete wall is higher than both in the centre and near the glass wall. This is also the case for both  $x=5$  and  $x=11$  m, which can be seen in Appendix C.

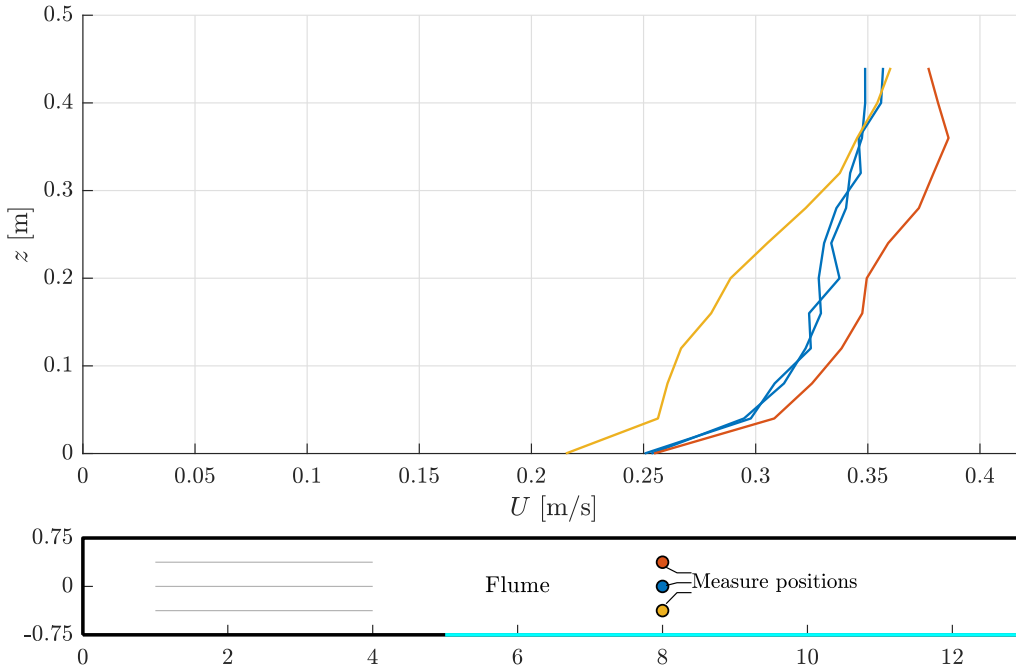


**Figure 3.7:** Mean velocities at  $x = 8$  m with  $Q = 100\%$  and  $h = 50$  cm.

Additionally, it was noticed that the 50 cm water level,  $h$ , always increased with 3.7 cm and 1.7 cm when the pump was working at 100% and 75% respectively.

### 3.3.2 Turbulent properties

As the Vectrino has measured the velocities in three directions, the total kinetic energy per unit mass from turbulence,  $k$ , can be calculated [Versteeg and Malalasekera, 2007]. From  $k$  the specific turbulence dissipation rate  $\omega$  can also be found, see equation (3.2).

$$k = \frac{1}{2} \left( \overline{(u')^2} + \overline{(v')^2} + \overline{(w')^2} \right) \quad \omega = \frac{\sqrt{k}}{C_\mu \ell} \quad (3.2)$$

The  $u'$ ,  $v'$  and  $w'$  indicate the fluctuations around the mean velocities in the  $x$ -,  $y$ - and  $z$ -directions respectively.  $C_\mu$  is a constant set to 0.09 [esi, 2019].  $\ell = 0.3$  m is the reference length scale, which is set as the hydraulic radius of the flume cross-section.

Calculations of the turbulence parameters at  $x = 8$  m in the centre of the flume are approximated as constant values for the upper half of the water depth.  $k \approx 0.0015$  and  $0.002$   $\text{m}^2/\text{s}^2$  and  $\omega \approx 1.43$  and  $1.66$   $\text{s}^{-1}$  for  $Q = 75\%$  and  $100\%$  respectively. The variation of  $k$  throughout the water depth in all examined locations are shown in Appendix C.

At a later stage in the project it was detected that the noise that occurs when using the Vectrino device, should have been examined better during and prior to testing. Instructions are given on how to determine the noise in the Vectrino manual.

It is therefore important to notice that there is a large uncertainty connected to the calculated values  $k$  and  $\omega$ , as  $k$  is a direct result of the size of the fluctuations, which could be noise induced.

Due to the lack of knowledge concerning the noise, the values of the turbulent parameters in this chapter are merely estimates, and might differ greatly from the actual conditions in the flume.

### 3.4 Summary

The current measurements were performed with attention to possible uncertainties, and measures were made in order to eradicate as many sources of error as possible. A longer period of measurements might have been required.

Velocity profiles were determined at different locations in the flume. It is chosen that the model test location should be at  $x = 8$  m, as the velocity profile here corresponds well with theory for a boundary layer flow along a flat plate. Also, the measurements at this location proved to have the least variation in velocities in the upper half of the water depth, where the models will be located. Functions to describe profiles in the centre of the flume at  $x = 8$  m have been quantified in Table 3.1. It was also found that the velocity profiles were not consistent across the width of the flume. This is regarded as a source of error, which is taken into account in further analysis.

An attempt was made to determine the turbulent properties of the flow field, namely the turbulent kinetic energy and the specific turbulence dissipation rate. While it was possible to calculate values of these two parameters, it was later uncovered that there might be a great deal of uncertainty related to the calculated values, as the exclusion of noise had not been made. It is therefore recommended to disregard the calculated values of the turbulent parameters in this chapter.

It was also observed during testing that the water level increased 3.7 cm and 1.7 cm when the pump was working at  $Q = 100\%$  and  $Q = 75\%$  respectively.

---



## 4. Experimental force measurements

This chapter concerns the force measurements on a single leg (Model Leg) of a FPP model and the whole model (Full Model) respectively, see Figure 4.1. The procedure in obtaining the forces is described first, followed by a presentation of the measured forces on the models.

It should be noted that the model scale FPP is not an identical scaled-down version of the P80. Furthermore, there are no wave absorbers in the experiments.

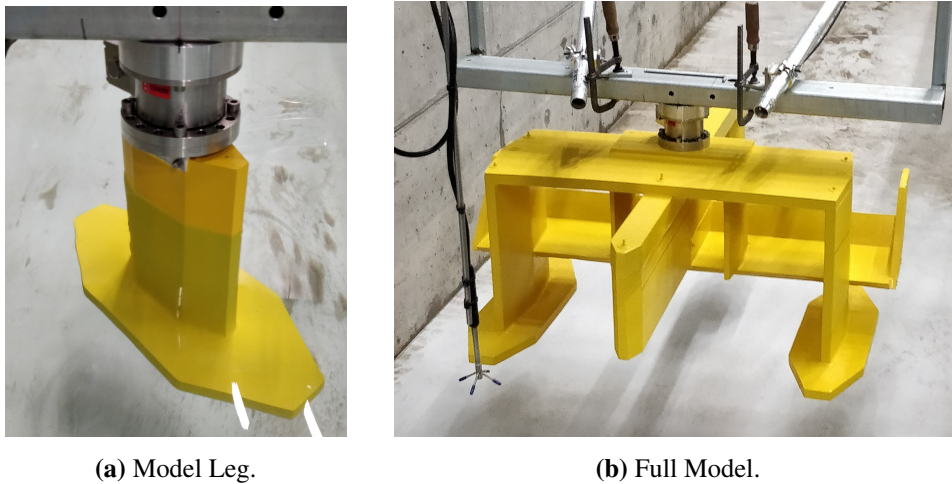


**Figure 4.1:** Models used in experiments.

The experiments are carried out with different orientations of the models. The current generation capacities,  $Q$ , have been quantified in Chapter 3. Replicates for every experiment are made to ensure that no significant variation in the results are present.

Results for each experiment can be found in Appendix E.

### 4.1 Setup and equipment for force measurement

The models are placed in the centre of the flume at  $x = 8$  m and held still by a setup seen in Figure 4.2(a). A force sensor from Schunk, 2019, which can be seen in Figure 4.2(b), is the connecting piece between the setup and the measured model. The sensor measures six voltage signals from where raw forces and moments acting on the model in all three directions are calculated. The sensor is able to measure signals within the range of  $\pm 10$  V corresponding to the forces and moments given in Table 4.1.

$F_x$	$F_y$	$F_z$	$M_x$	$M_y$	$M_z$
$\pm 65$ N	$\pm 65$ N	$\pm 200$ N	$\pm 5$ Nm	$\pm 5$ Nm	$\pm 5$ Nm

**Table 4.1:** Measurement range of force sensor.



(a) Setup of model in water. The Vectrino is raised out of the water, when the forces on the model are measured.



(b) The force/torque sensor with a 1 cm thick steel plate attached to mount the model.

**Figure 4.2:** Setup and equipment.

Prior to model testing, a range of tests were performed on the force sensor to control that the calibration software to the sensor produced reasonable results, see Appendix D. An issue was detected with the force sensor, where the force in the  $z$ -direction,  $f_z$ , changed linearly with time when a constant load was applied. However, it is still chosen to work with the sensor, as changes in loads are still accurately predicted, despite the slope of  $f_z$ . Also, the small changes it would amount to in the  $z$ -direction are not destructive of the test results.

All the experiments have been carried out with the longitudinal direction of the models orientated in five different directions,  $\theta = [0^\circ, 22.5^\circ, 45^\circ, 67.5^\circ, 90^\circ]$ , where  $0^\circ$  is the when the longest side of the Model Leg is parallel with the  $x$ -direction. The models were rotated in a counter-clockwise direction when seen from above. Both  $Q = [75\%, 100\%]$  has been tested for the Model Leg and only  $Q = 100\%$  for the Full Model.

Each test was carried out according to the following procedure:

1. Start data collection of forces
2. Wait at least 40 seconds to create offset values for baseline
3. Start current generation
4. Collect data for 4-9 minutes

From this procedure it should be clear that it is the difference in forces between a still water state and a steady current that is measured.

#### 4.1.1 Model Leg

The experimental setup for the Model Leg is seen in Figure 4.2(a). The Model Leg is placed in a water depth of  $h = 0.50$  m and with the bottom side held  $z = 27.0$  cm above the bottom of the flume, meaning that 23.0 cm plus 1.7 or 3.7 cm of the model is under water depending on the

current speed. Other dimensions of the Model Leg can be seen in Figure 4.3. Notice that the offset forces are measured at still water level, meaning that the extra hydrostatic pressure arising from the current induced water level increase is not included.

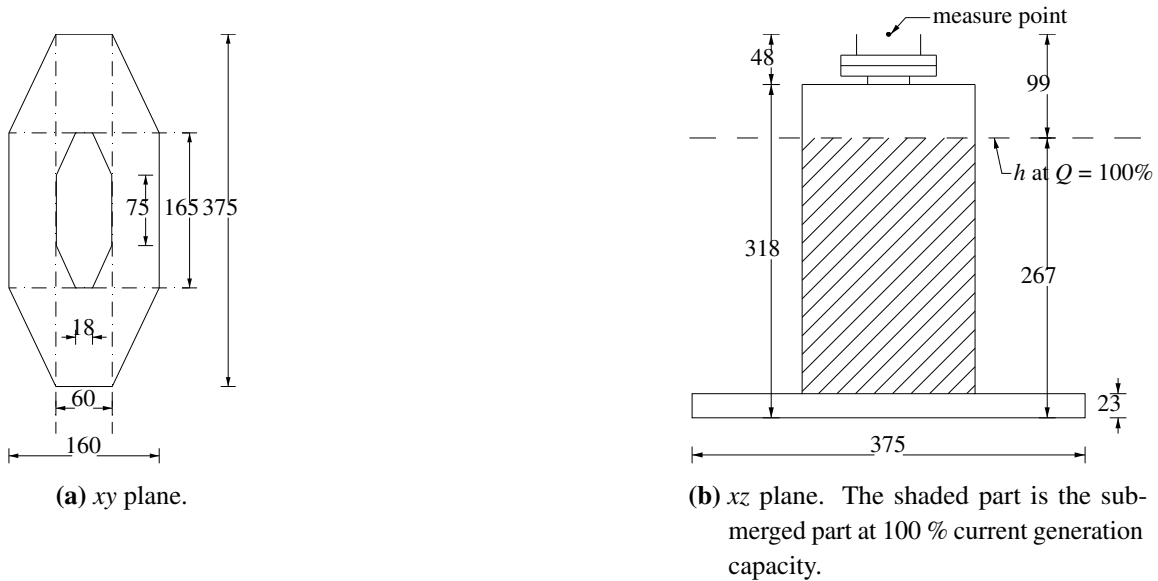


**Figure 4.3:** Model Leg.

It should be mentioned that the real model is not a perfect replicate of the drawings in Figure 4.3. E.g the web of the Model Leg is placed 0.3 cm eccentrically sideways in reality.

#### 4.1.2 Full Model

The Full Model is placed 26 cm above the bottom of the flume for 100 % current generation capacity, meaning that 27.7 cm will be submerged during testing. This adjustment is made to fit the buoyancy line from the drawing of the model, see Figure 4.4.

Prior to the experiments on the Full Model, weights were added to the model to balance it. This was done to get the measured voltage as close to zero as possible. The initially balanced model is seen in Figure 4.5(a).

Some adjustments had to be made when rotating the Full Model in the flume due to a large moment around the *y*-axis produced when orientating the model beyond  $22.5^\circ$  exceeding the measurement range of the force sensor. To solve this issue, additional weights were applied to create an initial counter-moment to make use of the full voltage measurement range, as shown in Figure 4.5(b). This action is justified by the fact that it is the difference between forces/moments with no current and forces/moments with a current that is used in the data analysis.

## 4.2 Data analysis

The forces and moments ( $f_x, f_y, f_z, m_x, m_y, m_z$ ) measured on the Model Leg and the Full Model are treated in the same way. The first 40 seconds of each test is the forces/moments measured without

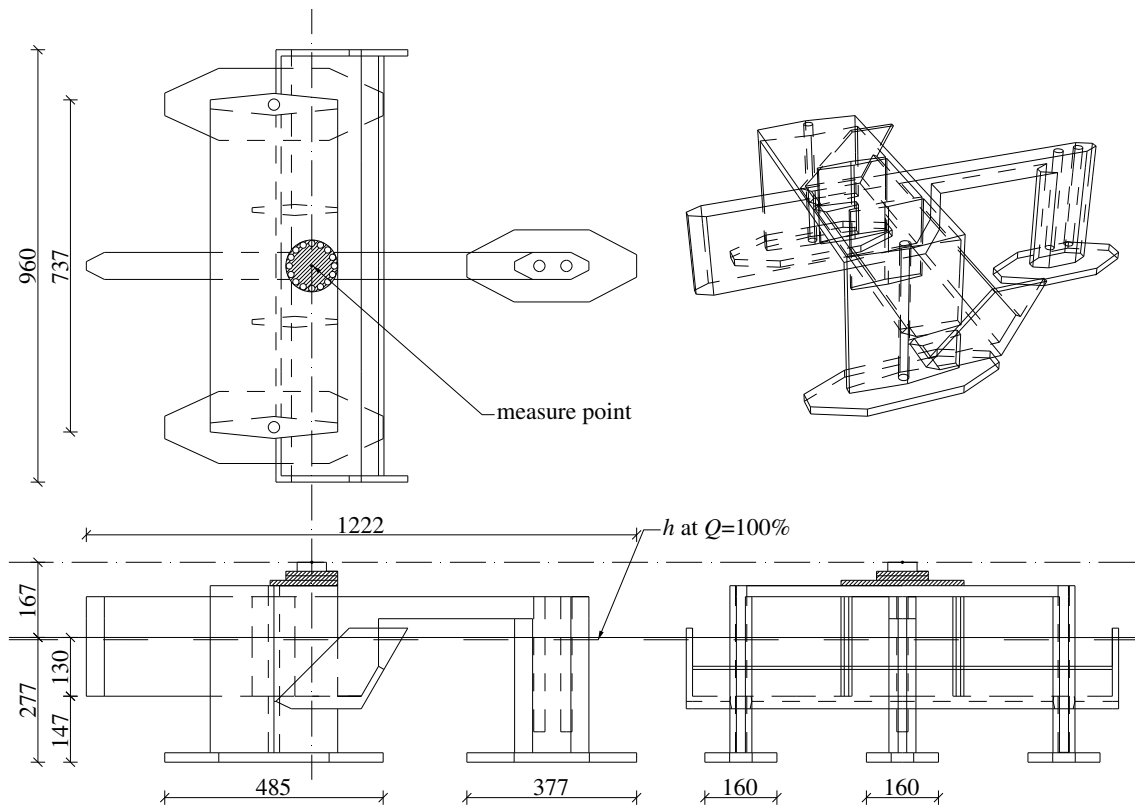
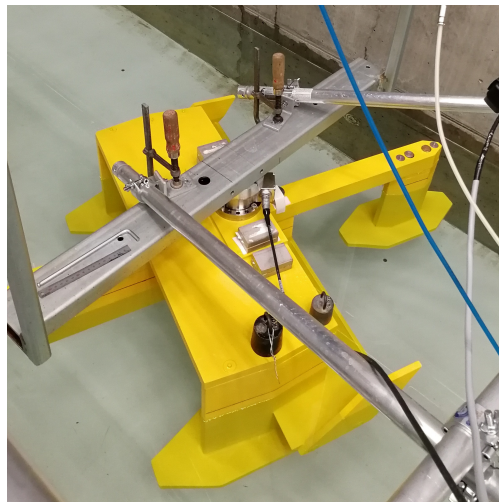


**Figure 4.4:** Drawing of the Full Model in mm.



(a) Balanced at 0°.



(b) Altered weight distribution at 67.5°.

**Figure 4.5:** Full Model balancing in flume.

the pump running. These measurements are averaged and used as offset values. The offset value is subtracted from the raw forces/moments data to have the baseline at zero. Thus the forces/moments that are generated by the current is determined, see Figure 4.6.

The raw force and moment signals are examined visually to detect any oddities. A 'start' and 'end' time are noted to create a time interval in which the signal is assumed steady. Inside this time interval an average value is calculated for each test. This average value is noted as the force/moment generated by the current for each test ( $F_x$ ,  $F_y$ ,  $F_z$ ,  $M_x$ ,  $M_y$ ,  $M_z$ ). It is secured that the start point is 180 s after the pump is started see Figure 4.6. Furthermore, the buoyancy effect created by the increase in water level when the current is started is subtracted from the force in the  $z$ -direction to give a corrected  $F_z$ . With regards to the force and moment directions, the displayed forces and

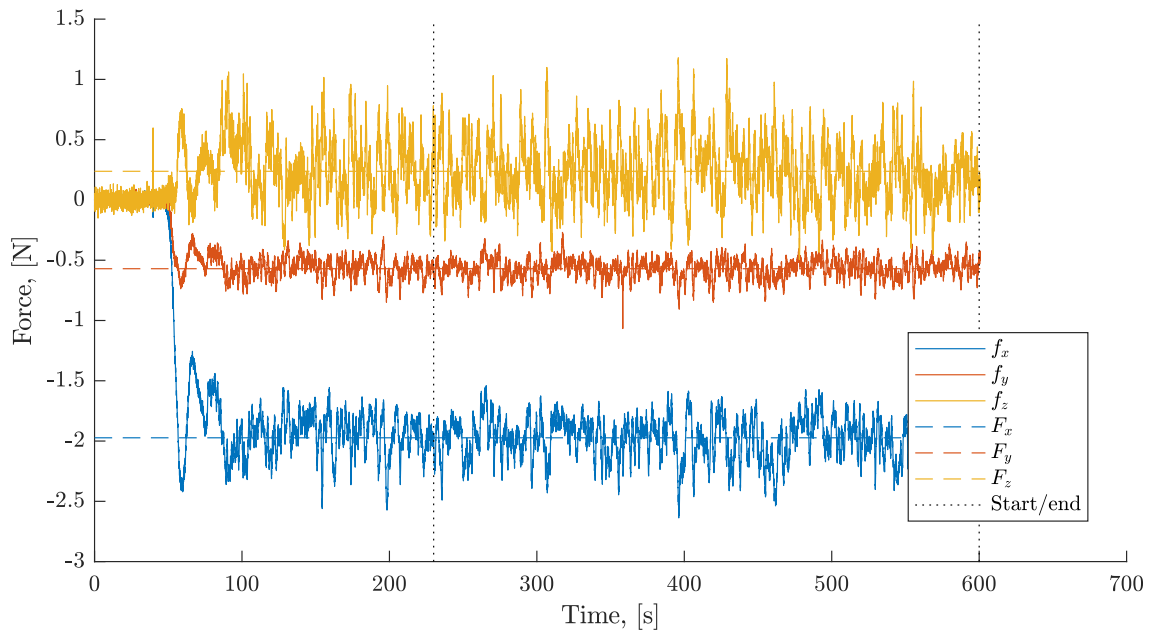


**Figure 4.6:** Example of forces measurement before correction for added buoyancy and direction. Data is for Model Leg with  $Q = 75\%$  and orientation of  $67.5\%$ .

moments in this report are converted from the measured coordinate system of the force sensor to the coordinate system of the flume, see Figure 4.7.

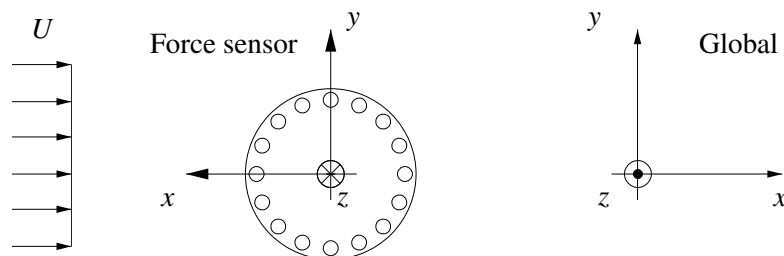


**Figure 4.7:** Change of the coordinate system from the force sensor to the global coordinate system for the flume when seen from above.

### 4.2.1 Model Leg results

The averaged forces and moments for all tests of the Model Leg are shown in Figure 4.8. The Model Leg tests were performed for all five orientations and for current generation capacities of both 75 % and 100 %.

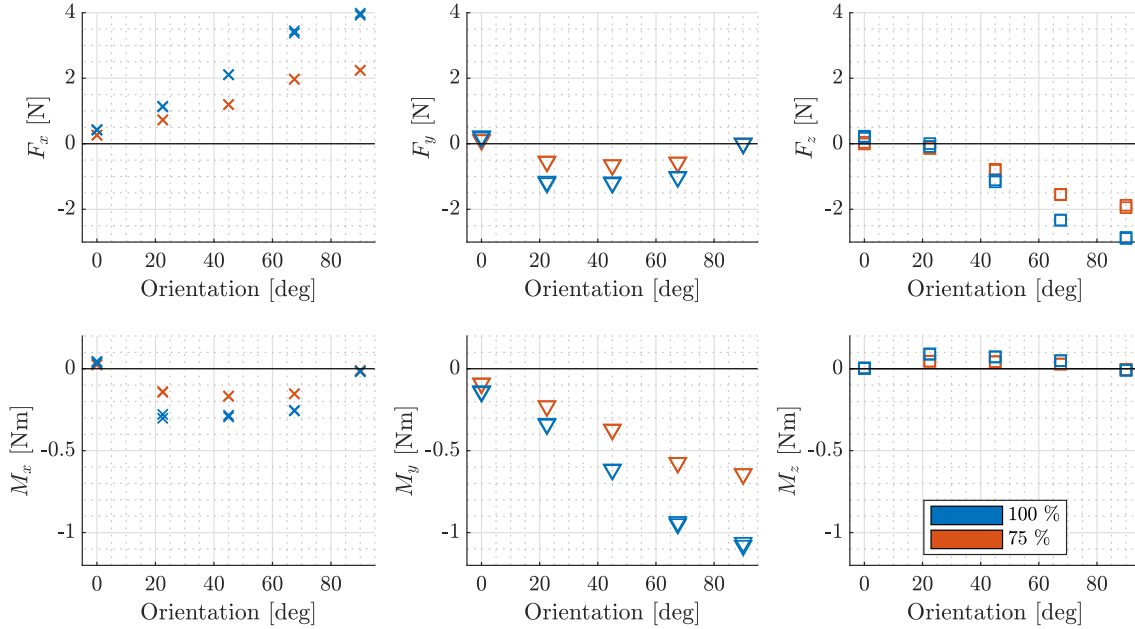


**Figure 4.8:** Forces and moments acting on the Model Leg in all directions at 75 % and 100 % capacity. At least two tests were performed for each orientation and velocity combination.

The forces in the  $x$ -direction increase as the Model Leg is rotated from  $0^\circ$  towards  $90^\circ$ , as would be expected due to a less streamlined structure causing more separation and a larger area for the pressure difference between front and back of the model to act on.

The forces in the  $y$ -direction at  $0^\circ$  are slightly positive, where it would be expected to be zero due to symmetry. However, the different velocity profiles on each side of flume, discussed in Chapter 3, would contribute to a force in the  $y$ -direction. Furthermore, the model itself is not perfectly symmetric as in Figure 4.3. These are assessed to be the reasons for the non-zero force at  $0^\circ$ .

As previously noted, the water level changes, when the current is generated, compared to when there is no current in the flume. The displayed  $F_z$  is corrected for the added buoyancy, generated by the rise in water level;  $\rho_w g V = 1.3$  or  $2.8$  N for 75% or 100% capacity respectively. So when looking at  $F_z$  in Figure 4.8 it is only the force generated from the current which is present and not the change in hydrostatic pressure.

The moments in the  $x$ - and  $y$ -directions are in large due to the contribution from the forces working in the  $y$ - and  $x$ -directions respectively. This can also be seen as  $M_x$  follows the pattern of  $F_y$ .

### 4.2.2 Full Model results

The results of the tests for the Full Model are shown in Figure 4.9.

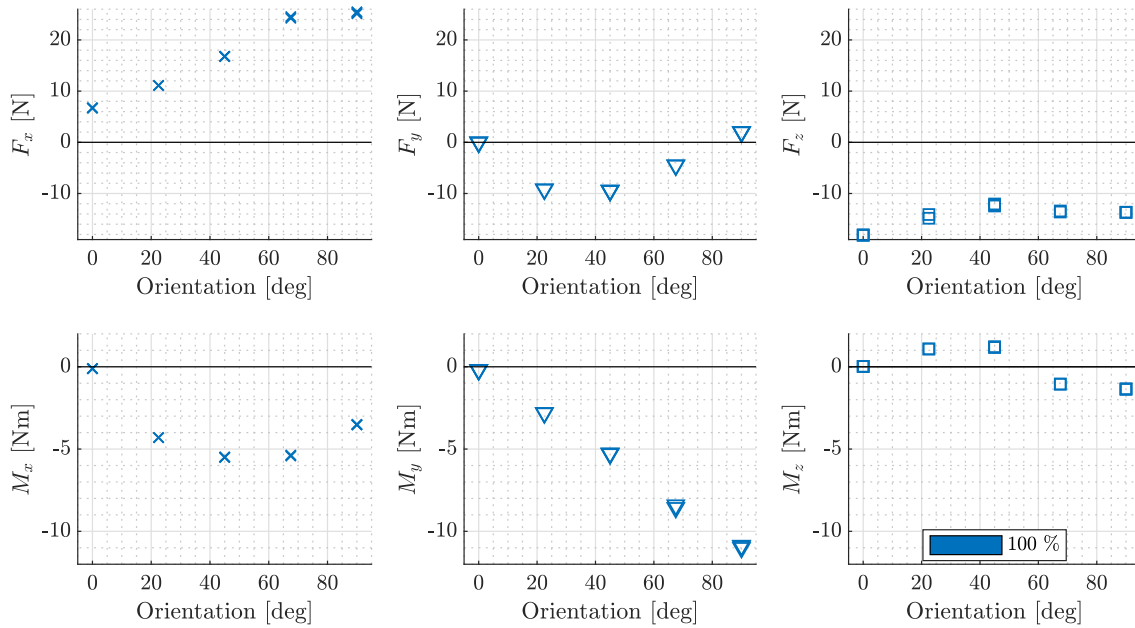


**Figure 4.9:** Forces and moments in all directions at 100 % capacity on the Full Model. At least two tests were performed for each orientation and velocity combination.

As expected, the force in the  $x$ -direction increases with orientation, though flattens out slightly between  $67.5^\circ$  and  $90^\circ$ . This is because the area perpendicular to the current direction at these two angles are similar.

The correction to  $F_z$  from buoyancy is calculated to be 27.8 N.

The forces in the  $y$ -direction are also as expected, with a larger  $F_y$  at  $22.5^\circ$  and  $45^\circ$ . For  $0^\circ$  the model is symmetric around the flow direction, which explains why the force is zero.

It is noted that  $M_y$  slightly exceeds the 10 Nm range for the  $90^\circ$  orientation. In these experiments it was not possible to keep the sensor output inside  $\pm 10$  V at all times due to fluctuations, however reasonable results were obtained nonetheless.

It is important to notice that the tendencies of the moment cannot be compared to reality, as the P80 is moored at fore part of the hull. In these experiments the moments on the Full Model are measured at the measuring point shown in Figure 4.4.

### 4.3 Summary

The force measurements produced very consistent results between similar test cases for both the Model Leg and Full Model. This is visible in Figure 4.8 and 4.9, as data points for each set of orientation and current generation capacity lie on top of one another. From this it is assessed that the experiments have been conducted in a similar manner to one another. Also, the current is considered a steady state over the data recording length, meaning that the recording duration is sufficient.

It should also be noted that the models are not a perfect match between computer drawings and reality. For example the legs of the Full Model were not exactly the same length, and the body of the Model Leg's width differed a few millimetres over the length, which have an influence on the obtained results.

The forces in the  $y$ -direction have a slight uncertainty for the Model Leg at  $0^\circ$  orientation due to the imperfect geometry and difference in velocities on each side of the flume.

The forces in the  $z$ -direction are also exposed to uncertainty, due to the rise of the water level when the current generation is started. There could also be an uncertainty in a possible time variation of  $F_z$  as presented in Appendix D, however this uncertainty is not considered further.

---

## 5. Numerical validation - Model Leg

This chapter concerns the validation of the CFD model for the Model Leg. The aim is to build a model that is stable and valid for different orientations of the structure. Validation is done by comparing CFD results with experimental results obtained in Chapter 4. All five orientations of the Model Leg,  $\theta = [0^\circ, 22.5^\circ, 45^\circ, 67.5^\circ, 90^\circ]$ , are simulated with a current velocity of  $\sim 0.27 - 0.35$  m/s, corresponding to Reynolds number in the range of  $1.0e5 - 1.3e5$ .

The CFD analysis of the Model Leg includes a convergence analysis to determine a sufficient refinement of the background mesh, see section 5.3. In section 5.4 a series of sensitivity analysis are performed, including variations of turbulence parameters, inlet velocity, surface refinement i.e.  $y^+$  and wall functions. These studies are performed to determine the boundary conditions for the numerical model.

The sensitivity analysis are also used to draw conclusions for the numerical models of the Full Model and the P80, which will be discussed in their respective chapters. The sensitivity analysis have been conducted on the Model Leg due to the relatively low computational cost and run time for a simulation compared to the Full Model or P80.

In section 5.5 the experimental results are compared to the results from the CFD analysis. All values of forces and moments can be found in Appendix F.

### 5.1 Computational domain

The computational domain shown in Figure 5.1 is made to resemble a part of the actual flume at AAU, see Figure 3.1. Assumptions and limitations concerning domain size and boundary conditions are described in the following.

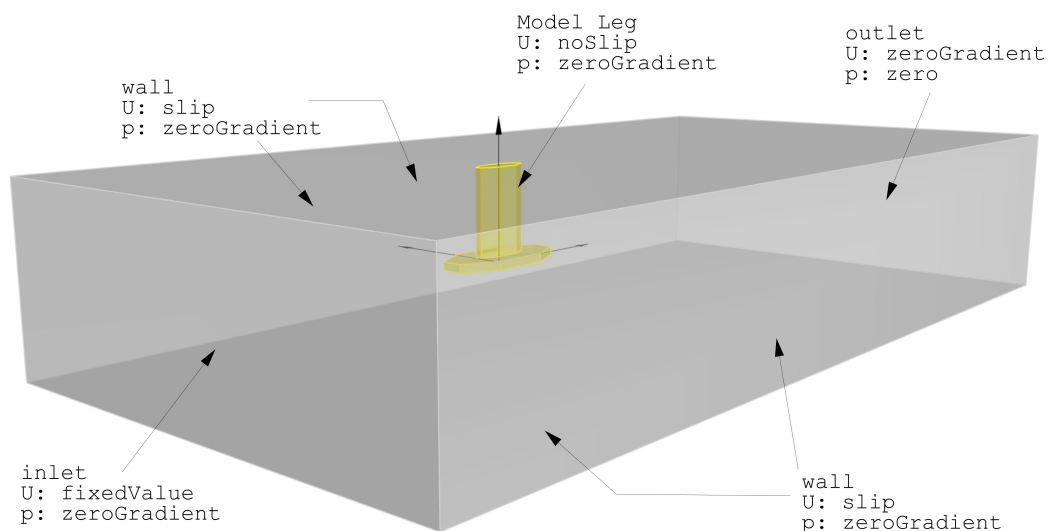


**Figure 5.1:** CFD domain, including OpenFOAM boundary conditions for pressure and velocity, for the Model Leg

- A domain length of 3 m in the  $x$ -direction is found to be sufficient see section 5.3. The extent of the domain starts 1 m in front of the centre of the Model Leg and ends 2 m after same, see Figure 5.2 [Rosetti, Vaz, and Fujarra, 2012]. The height is equal to the water level, when there is a current, i.e. 0.5 m plus the rise in water level for the given  $Q$  (0.017 m for 75 % and 0.037 m for 100 %).
- The flume walls in the experiment are considered to be smooth and sufficiently far away, thereby assuming that the Model Leg would not be affected by any viscous effects occurring at the flume walls. Therefore, the side walls (Front and Back) and Bottom of the flume have been given the slip condition. The Top boundary is also modelled with a slip condition, making it possible to use a single-phase solver, see Figure 5.1, though it is in reality a free surface.
- The inlet turbulence parameters are determined from Menter, 1994 as being  $[k, \omega]=[1e-8 \text{ m}^2/\text{s}^2, 1 \text{ s}^{-1}]$ . This is determined on basis of the study for the turbulence parameters, see section 5.4.1.
- The inlet velocity is modelled as velocity profile given by equation (3.1) over the width of the flume with the values given in Table 3.1. The inlet velocity profile is examined in section 5.4.2.
- The computational settings with regards to solver, turbulence model, and wall functions are given in section 2.4.

### 5.1.1 Mesh

The mesh domain built with `blockMesh` consist of 27 blocks, three subdivisions of the domain in both  $x$ -  $y$ - and  $z$ -direction illustrated by the dotted lines in Figure 5.2. Grading of the cells in the outer blocks are applied towards the cells in the centre blocks (in  $xy$ -plane), in which the model is placed, see Figure 5.3. It is also ensured that the aspect ratio  $\sim 1$  within the centre blocks.

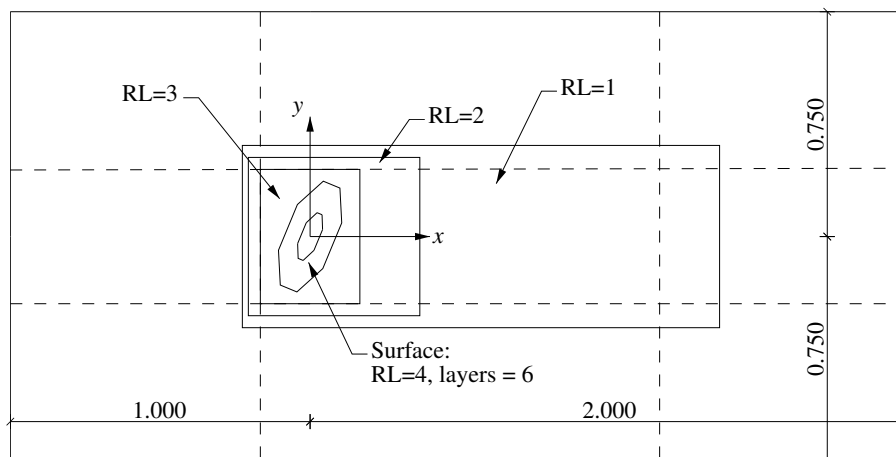


**Figure 5.2:** The Model Leg domain showing the refinement regions for orientation of  $67.5^\circ$ . Units in meters.

Refinement regions are defined around the Model Leg. Since the models influence on the flow increases towards the model, the cell size is refined in the same manner. A refinement region is also defined in the wake to better resolve the effects to the flow from the structure.

Further refinement is applied to the cells at the surface of the model. The `refinementLevel (RL)` is increased and `addLayers` are used to obtain  $y^+ < 1$  for the cells closest to the surface, meaning that the centre of the cells at the surface will be in the lower part of the viscous-sub layer, elaborated in Appendix A.3.

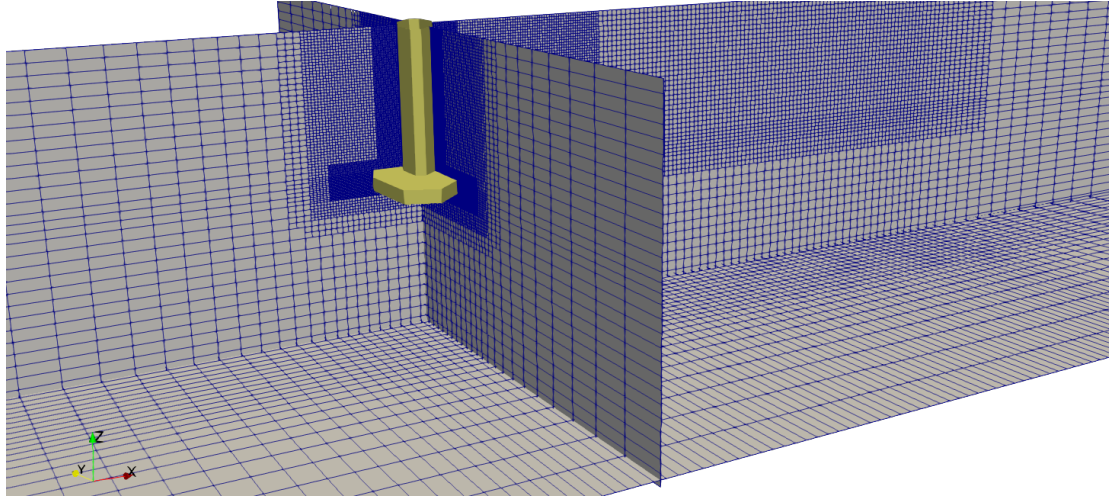


**Figure 5.3:** Mesh domain for the Model Leg.

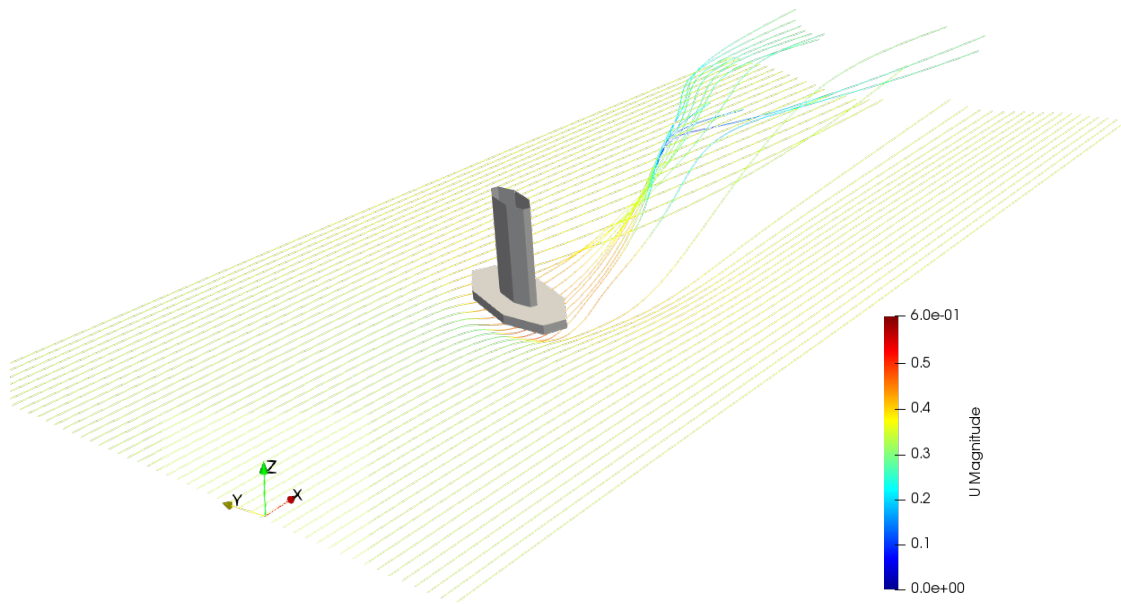
The setup of the mesh remains constant throughout the analysis of the Model Leg, but the amount of cells are varied in the convergence study. The variation is done using the parameter,  $N_z$ , which defines the subdivisions of the background mesh i.e. the `blockMesh` in the  $z$ -direction. When  $N_z$  is increased, the mesh in all blocks of the domain are refined with the same ratio, ensuring that the aspect ratio of the cells are consistent when refining. A mesh with  $N_z = 31$  and 6 added layers - corresponding to approximately 3 million cells - is found to be sufficient, and is described in section 5.3. The mesh can be seen in Figure 5.3 for  $67.5^\circ$  orientation.

## 5.2 General flow description

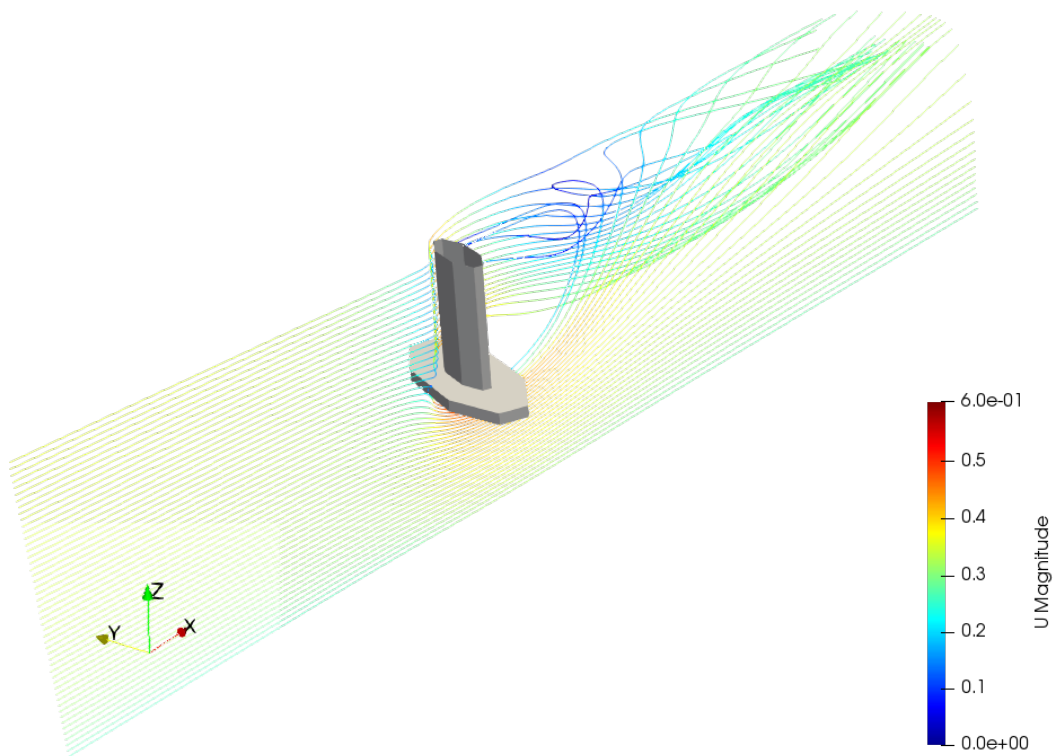
Figure 5.4 and 5.5 are made from the final result of the Model Leg subjected to 100 % current generation velocity and an orientation of  $67.5^\circ$  and  $0^\circ$ , and are used for a qualitative description of the flow characteristics.

The figures show the velocities along streamlines seeded at the inlet. Flow separation occurs beneath the Model Leg, where the fluid is accelerated around this separation region to preserve continuity in the flow field. This occurrence would also be present in the experiment and thereby causing the measured force in the negative  $z$ -direction, see Figure 4.8.

Just behind the Model Leg, separation occurs, which can be seen in Figure 5.4(b) by that the streamlines go around a large region behind the Model Leg. Behind this separation region, the wake is found, where the streamlines gradually become more and more laminar again, as the effect of the structure wears off over distance.

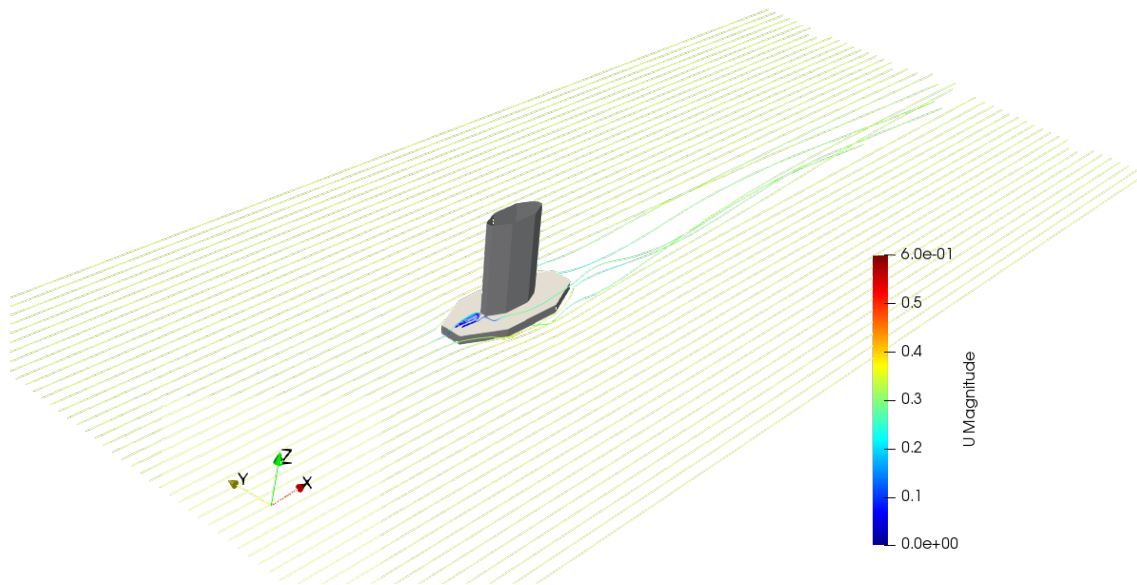


(a)  $xy$ -plane with seeding at  $z = 0.02$ .

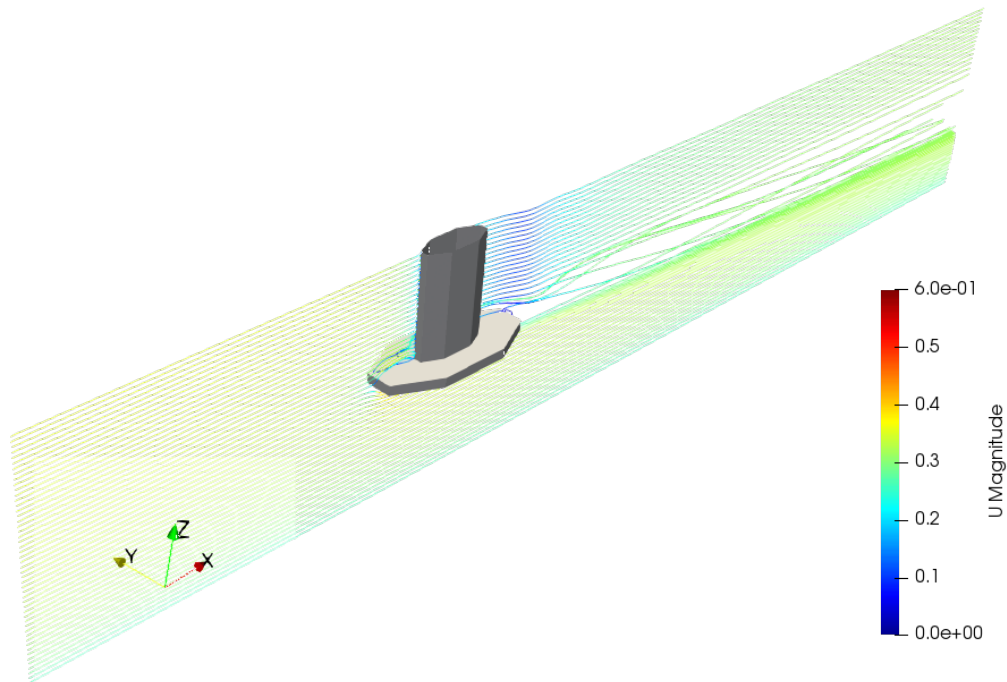


(b)  $xz$ -plane with seeding at  $y = 0.001$ .

**Figure 5.4:** Velocity magnitude along streamlines for model orientation at  $67.5^\circ$ .



(a)  $xy$ -plane with seeding at  $z = 0.02$ .



(b)  $xz$ -plane with seeding at  $y = 0.001$ .

**Figure 5.5:** Velocity magnitude along streamlines for model orientation at  $0^\circ$ .

Figure 5.5 is included to show how the flow characteristics differ between the orientations of the Model Leg. At  $67.5^\circ$  turbulent eddies behind the model would come from the flow under the Model Leg, where at  $0^\circ$  it goes around, and the current is generally less affected by the structure.

### 5.3 Convergence analysis

For this convergence study the parameters presented in Table 5.1 are applied. Notice that the velocity profile is for this section set as a plug flow and the turbulence parameters are the ones calculated in section 3.3.2.

Symbol	Property	Value
$U_{ref,100}$	Reference velocity at 100 % capa.	0.34 m/s
$k$	Turbulent kinetic energy	0.002 m <sup>2</sup> /s <sup>2</sup>
$\omega$	Specific turbulence dissipation rate	1.66 s <sup>-1</sup>

**Table 5.1:** Properties from experiments, which are used for convergence analysis boundary conditions in CFD analysis of Model Leg.

The mesh is refined by the parameter  $N_z$ . The number of layers at the structure surface are also adjusted to keep  $y^+$  between 0.8 and 1.0. Convergence tests have been performed for orientations of  $0^\circ$  and  $67.5^\circ$ . The convergence tests are run for  $N_z = [18 : 35]$ .

From Figure 5.6 it can be seen that small variations occur when refining the mesh at  $0^\circ$ . However, the range in which the results differ is only 0.04 N. With that in mind, one could also argue that the mesh is already converged at the coarsest mesh presented in Figure 5.6. It is chosen to use the mesh with  $N_z = 31$  (i.e. 2.5 for  $0^\circ$  and 3.1M cells for  $67.5^\circ$ ) as the variation in results is less than 0.02 hereafter, compared to 0.04 for all the results in  $F_x$ .

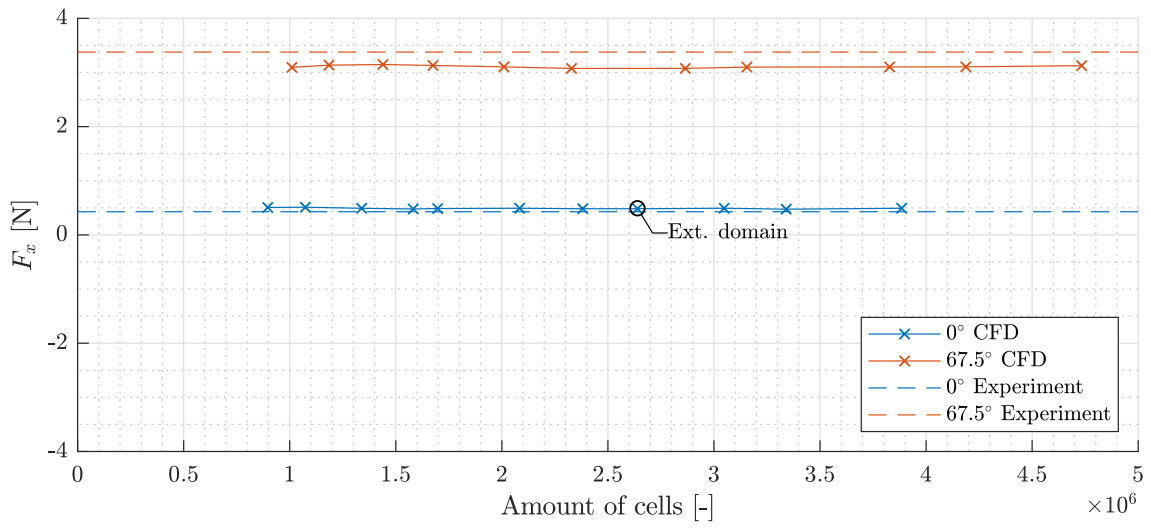
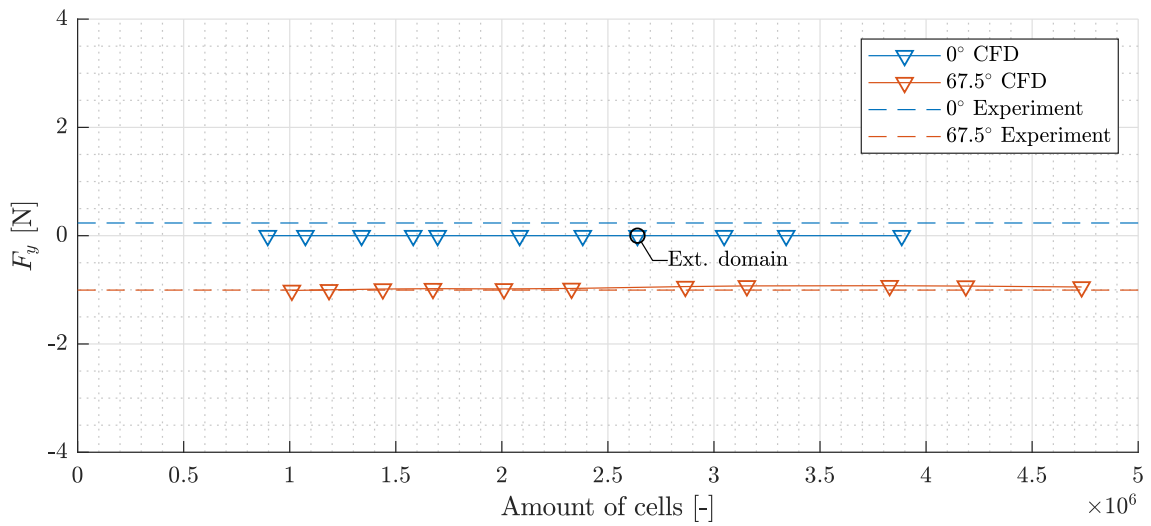
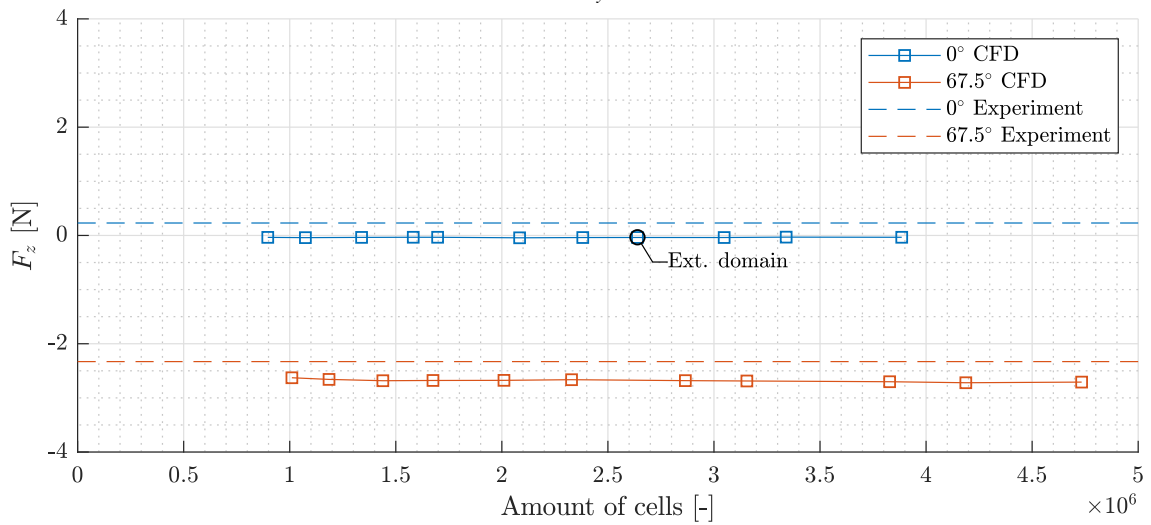
It can also be seen that though the mesh size is converged, the CFD results and experimental results are still about 0.07 N apart - or around 18 % higher - for  $0^\circ$ .

For the convergence of the  $67^\circ$ , see Figure 5.6(a), the difference between the different mesh sizes is no more than 0.08 N between the highest and lowest results and 0.03 N after when the mesh size is higher than 3M ( $N_z = 31$ ). Therefore the solution is assumed mesh independent after this point.

Interestingly, it can be seen that the converged results for  $67.5^\circ$  orientation show a lower force in the  $x$ -direction for the CFD results, as opposed to higher in the  $0^\circ$  orientation. In fact, the forces are about 10 % lower in the CFD compared to the experiments.

Finally, a simulation has been run for the chosen mesh size of  $N_z = 31$  to verify that the domain length is sufficient. The domain length was doubled to 2 m in front and 4 m behind the centre of the Model Leg, and as can be seen from Figure 5.6 the difference has no influence on results.

From the results of the convergence analysis, it is chosen to use mesh sizes defined by  $N_z = 31$ , as it produces a good balance between mesh refinement and simulation time. With this  $N_z$ -value, 6 layers are added near the structure to obtain a calculated  $y^+$  value between 0.8 and 1.0.

(a)  $F_x$ (b)  $F_y$ (c)  $F_z$ **Figure 5.6:** Convergence of Model Leg for 0° and 67.5°.

## 5.4 Sensitivity analysis

In this section the sensitivity of the CFD model to different boundary conditions and parameters are examined. Some justifications made for the numerical models of the Full Model and the P80 in chapter 6 and 7 are also based on the following analysis.

### 5.4.1 Turbulent parameters

The turbulence kinetic energy was initially calculated from analysis of the current velocity in Chapter 3, where it was determined that  $k = 0.002$  and  $\omega = 1.66$  through their turbulent relation. However, it was later found that there might be great uncertainty regarding these calculated values, and that the turbulent parameters might be much lower in reality. Therefore, both small variations of the initial  $k$  and  $\omega$  stated above, and recommended values by Menter, 1994, regarding the  $k - \omega$ -SST model, have been included in this study. The freestream values of  $[k, \omega]$  have therefore also been set to the pair values of  $[1e-08 \text{ and } 1]$ , and  $[1e-12 \text{ and } 0.1]$ , which are the maximum and minimum values for the recommended range.

The results of the analysis can be seen in Figure 5.7 for  $F_x$ . It is noted that the value of  $k$  is sensitive around 0.001-0.003 in this study. Therefore, and due to the insecurities mentioned before, it is chosen to use the parameters determined in accordance with Menter, 1994.

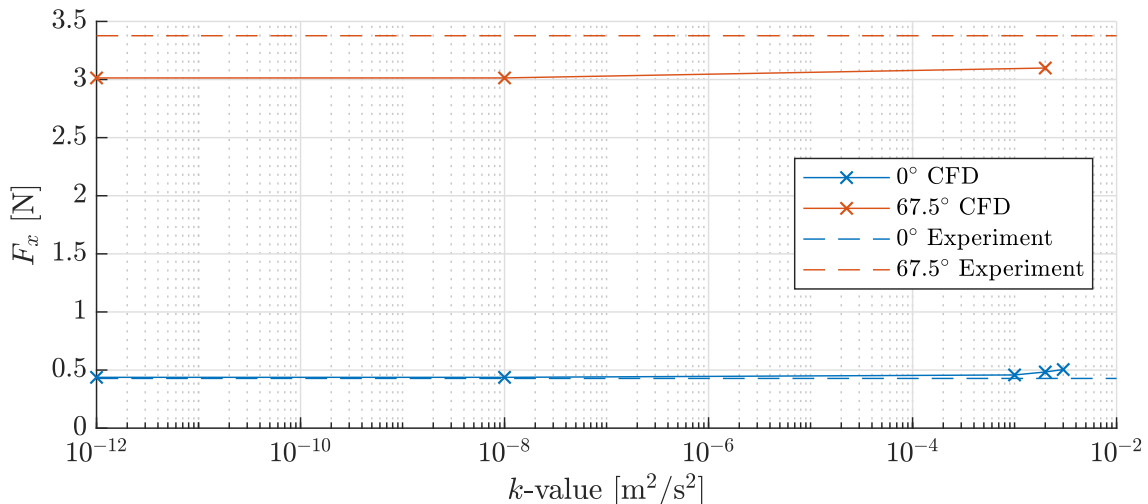


Figure 5.7: Effect of turbulence parameters on force in  $x$ -direction for  $0^\circ$  and  $67.5^\circ$  orientation.

### 5.4.2 Inlet velocity field

The inlet velocity profile was approximated as a plug flow with slip conditions along the flume walls for the the previous analysis. The simulated plug flow is shown in Figure 5.8b.

In this analysis both a plug flow with a no-slip condition along the bottom of the flume, and a profile matching the description in section 3.3.1 with slip condition along the bottom is simulated.

The resulting profiles are seen in Figure 5.8, where it is found that the plug flow with no-slip yields a velocity profile at the model location which is far from the experimental conditions. This is due

to a coarse mesh at the bottom wall, where there should have been a  $y^+ < 1$  to be able to describe the large velocity gradients. In Figure 5.9 the influence of the velocity distributions on the forces are shown. Both  $x$  and  $z$  are seen to be much larger than experimental results for the no-slip plug flow, wherefore it is chosen not to use these conditions for further analysis.

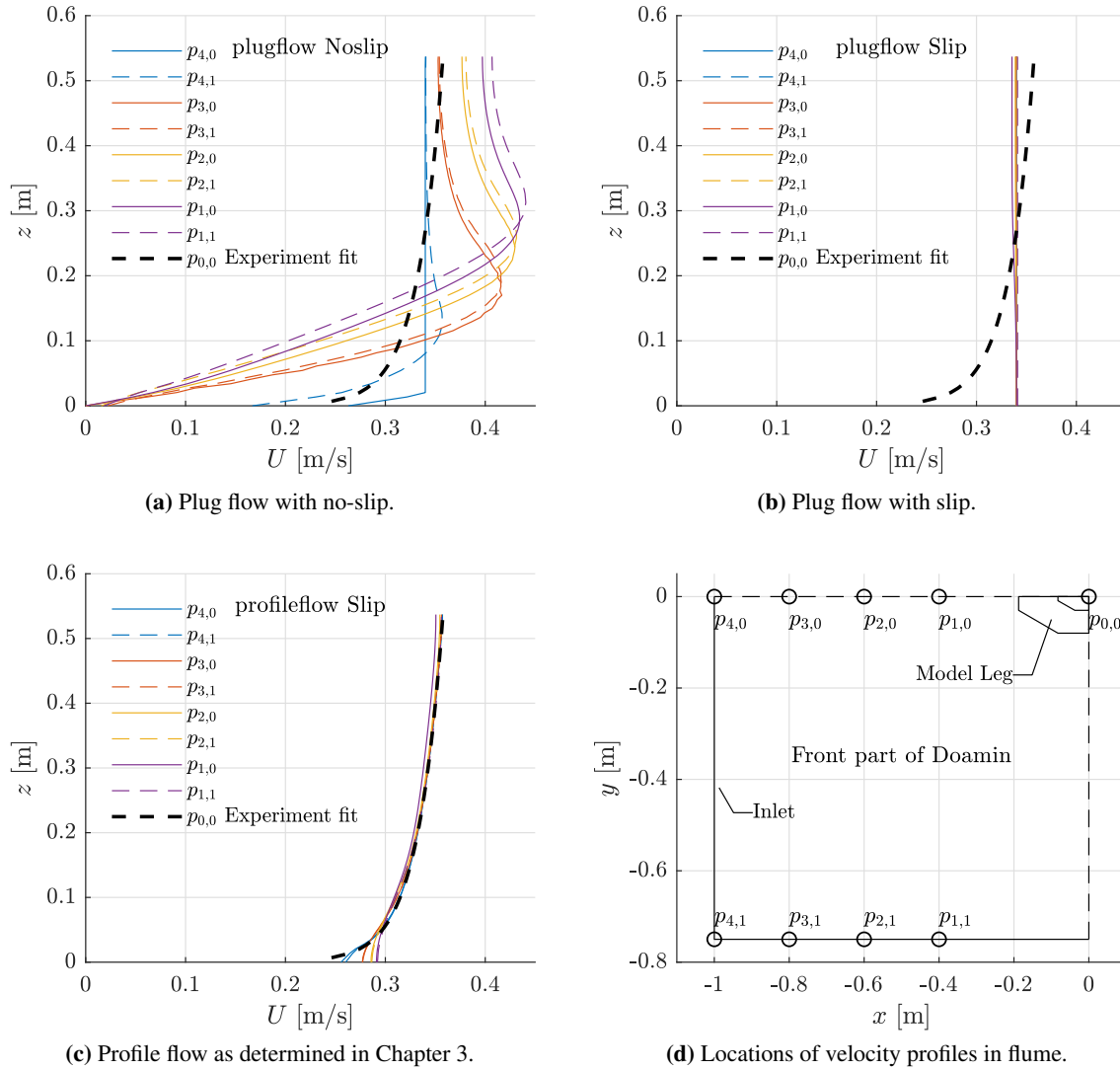


**Figure 5.8:** Velocity profiles and their locations in the flume.

The simulation with the velocity profile determined from experiments and slip conditions along all walls is shown in Figure 5.8c. As expected, the profile fits the experimental profile at the inlet, and also in front of the structure. Results shown in Figure 5.9 show that similar results are obtained to the plug flow, yet a small difference is noted at closer observation.

As there is a small difference between the profile and plug inflow with slip conditions, it is chosen to use the profile fit, as it is a better representation of the experimental conditions.

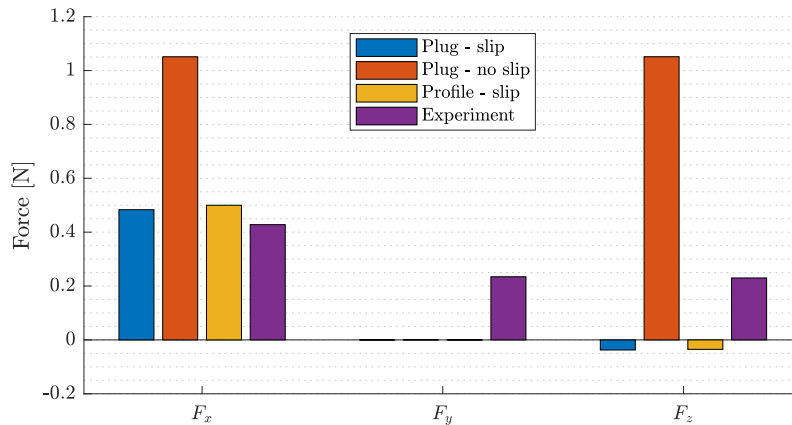


**Figure 5.9:** Forces in  $x$ ,  $y$  and  $z$  for the different velocity profiles with Model Leg orientation of  $0^\circ$ .  $F_y$  is 0 N in CFD, which complies with theory and 0.2 N in the experiments because of the difference in velocities on each side of the experimental Model Leg.

### 5.4.3 Wall functions and cell size near structure

In the CFD simulations of the P80 it would be very computationally costly to obtain a  $y^+ < 1$ . Therefore, the effect of changing  $y^+$  is analysed for the less computational costly Model Leg at  $0^\circ$  and  $67.5^\circ$ . In addition, the significance of the use of the wall functions `kLowReWallFunction` and `nutUBlendedWallFunction` is examined. The effect of the wall functions come into use when the nearest cell centre lies outside of the linear viscous sub-layer, which is explained in detail in Appendix A.

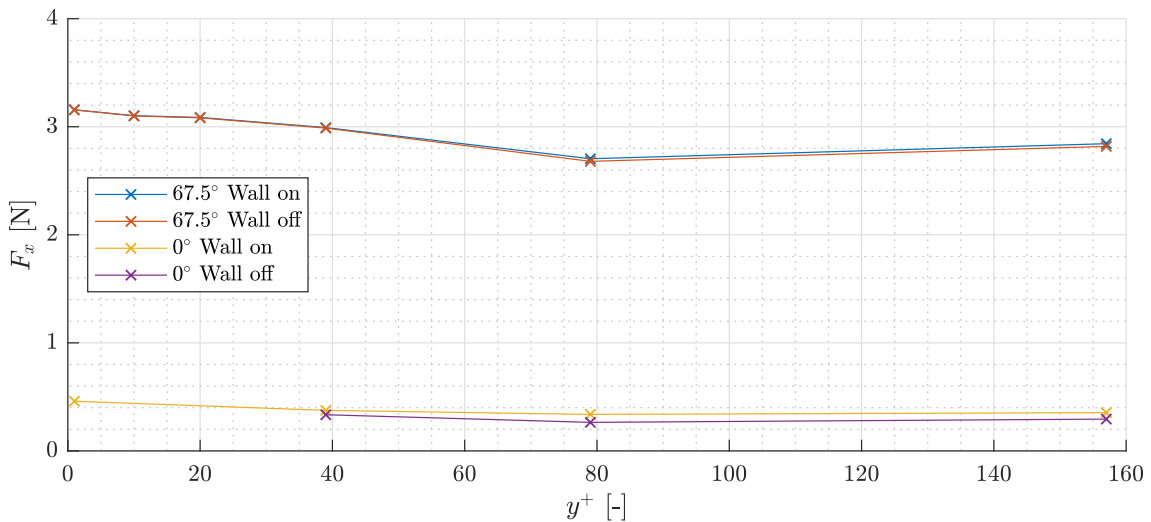


**Figure 5.10:** Wall function on/off and  $y^+$  variation.

In Appendix B, the boundary conditions that are changed when turning the wall functions off are shown. The default setting in this report has been that wall functions are 'on'.

While it was expected that having the wall functions enabled for low  $y^+$  would yield the same results as when disabled, it is also found that the results are practically the same for higher values

of  $y^+$  too for  $67.5^\circ$ , see Figure 5.10. At  $0^\circ$  the difference is more evident, as a larger part of the drag force will be due to the viscous forces.

It is also found that the  $y^+$ -value has a potentially significant effect on results, no matter whether the wall functions are on or off. When using a higher  $y^+$ -value with wall functions on, results for  $F_x$  decreased by up to 15 % for  $67.5^\circ$  and up to 27 % for  $0^\circ$ . These findings should be taken into consideration when using a higher  $y^+$ , as the case will be for the P80. For the Model Leg  $y^+ < 1$  remains.

#### 5.4.4 Inlet direction

It is investigated whether it would be possible to simply change the inlet velocity direction in a quadratic domain (seen from above). This would result in only having the need for one mesh for running currents from different directions on the P80. The analysis has been performed for the  $67.5^\circ$  orientation of the Model Leg, with the flow fields shown in Figure 5.11.

Two analyses are performed; (a) the Model Leg orientated  $67.5^\circ$  with a current running in the  $x$ -direction i.e. parallel to the grid lines. (b) on a Model Leg orientated  $0^\circ$  with a current running at an angle of  $67.5^\circ$  from the  $x$ -direction. For the analysis, the boundary conditions for all the side walls are set as `inletOutlet`.

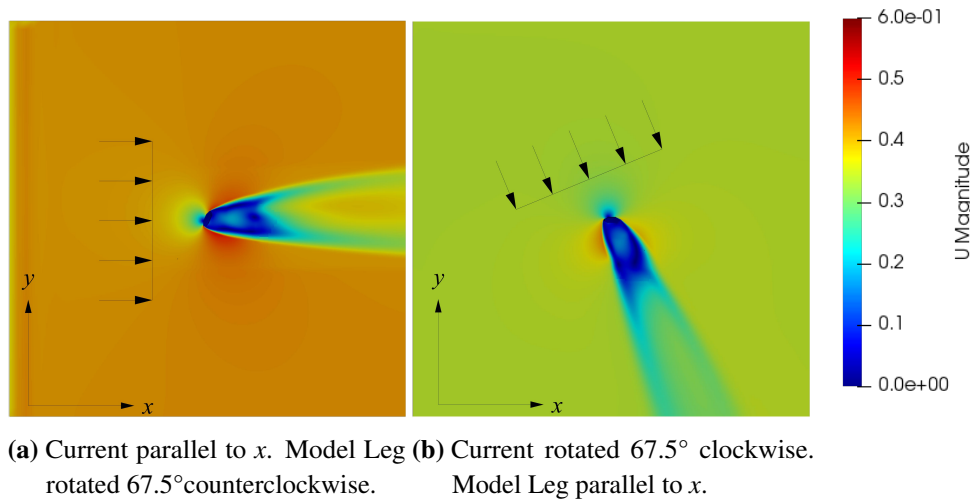


**Figure 5.11:** Flow field for the current acting at a  $67.5^\circ$  angle on the Model Leg, where the current inlet direction is varied.

It can be seen from Figure 5.11 that the magnitude of the velocities in the flow fields do not correspond to one another, leading to the variation in forces shown in Figure 5.12. The difference in results is significant, and this concept will therefore not be applied further in this project.

It should be noted that this idea came at a late stage in the project, wherefore only a crude analysis was able to be performed. The authors of this report believe it would be beneficial to further investigate this idea in future studies concerning the effects on a complex structure from different directions, as meshing has been found to be where the most difficulty lies in CFD analysis.

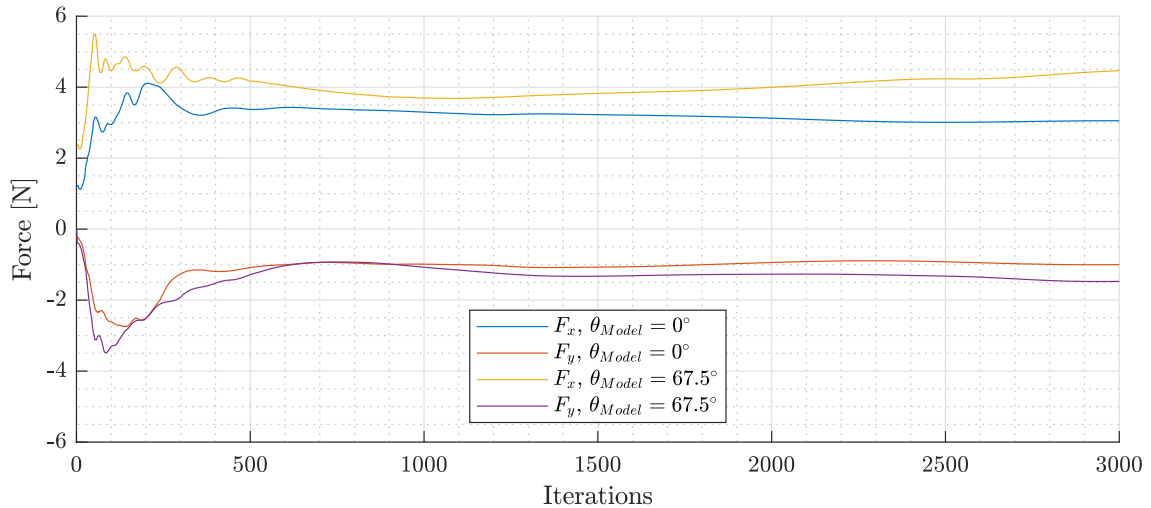


**Figure 5.12:** Forces for the  $67.5^\circ$  orientation of the Model Leg, modelled by rotating the structure or the inlet flow direction

## 5.5 Experiment comparisons

In this section, all the different orientations of the Model Leg are simulated with the boundary conditions given in the start of the chapter. 10 different scenarios are carried out; two different current velocities and five different orientations of the Model Leg. Results of the forces can be seen in Figure 5.13. Figures of the moments can be seen in Appendix F along with a table of all the results.

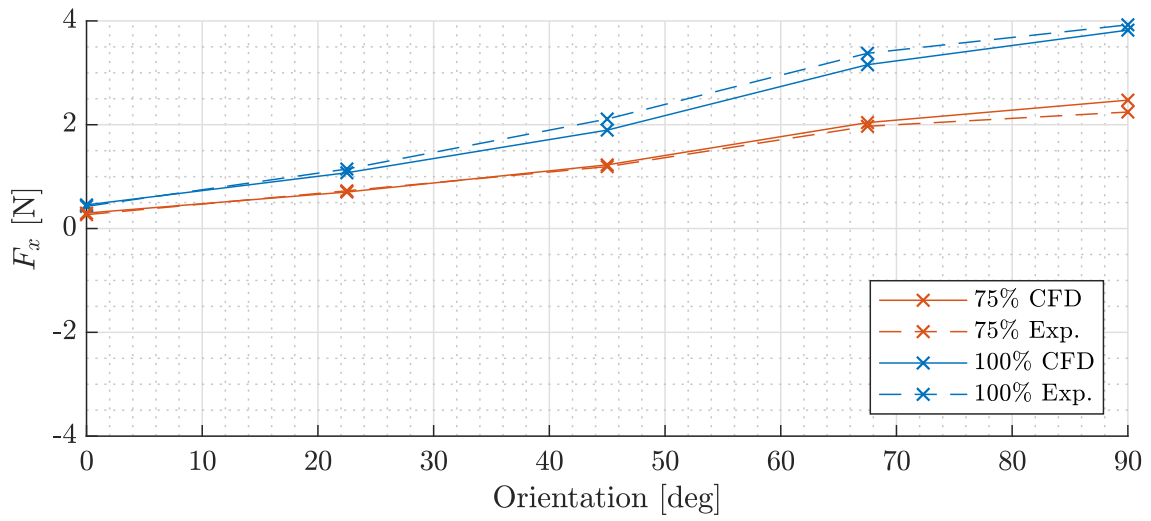
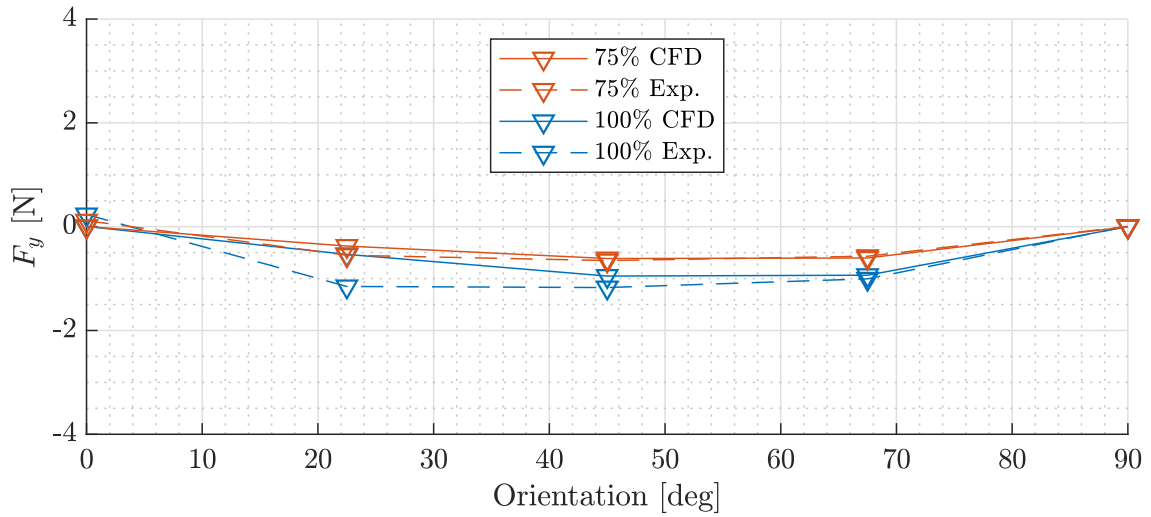
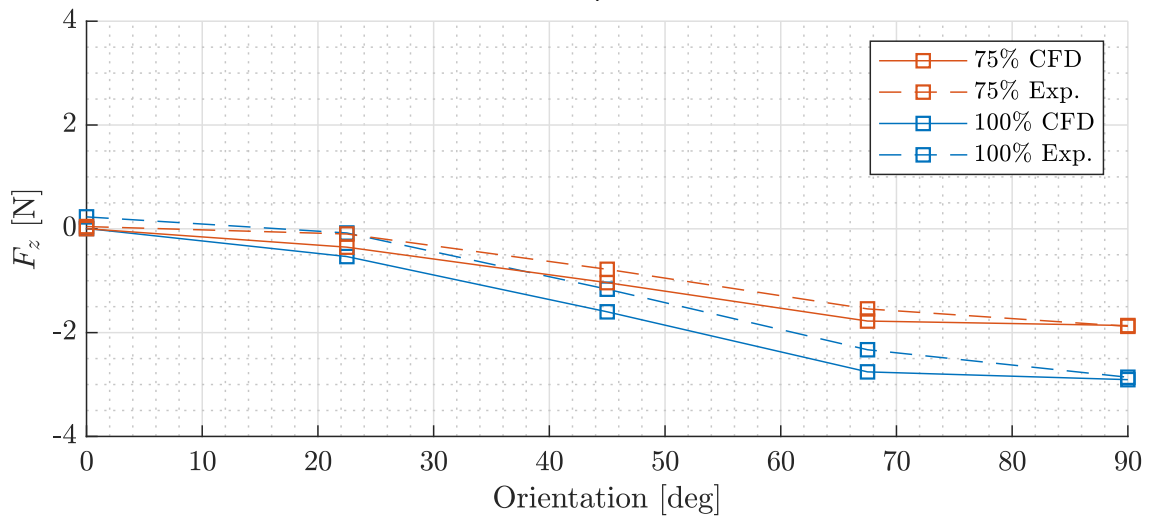
The comparison between the forces in the  $x$ -direction,  $F_x$ , shows that the CFD model represents the experiment very well. There is a good tendency when the model is orientated differently. The forces are in general described well both for different orientations and velocities.

Figure 5.13(b) shows that the forces in the  $y$ -direction,  $F_y$ , are quite similar when the orientation exceeds  $45^\circ$ . However, some differences are observed at especially  $0^\circ$  and  $22.5^\circ$ . The difference at  $0^\circ$  has already been accounted for, as the difference in velocity on each side of the flume in the experiments differed.

These unequal velocities could also have an influence on other directions with large surfaces for pressure forces in the  $y$ -direction, i.e.  $22.5^\circ$  and perhaps  $45^\circ$ . In any case, it is known that the  $F_y$  measured in the experiments are not perfect, wherefore the results obtained from the CFD analysis seem reasonable. Especially, as the CFD results for  $0^\circ$  and  $90^\circ$  agrees well with theory. Also, the  $67.5^\circ$  orientation results, where the unequal velocities across the flume would have a smaller influence, are almost equal.

The CFD results for  $F_z$  match the tendency of the experiment well, see Figure 5.13(c). It is hard to justify whether the offset between the results is due to incorrect calculations from the numerical model or experimental uncertainties. Nevertheless, the results are still satisfactory.

An overview of all the results can be seen in Figure 5.14, and again the tendency is that the CFD results are very close to the experimental results. This is confirmed by the slope of the fit between

(a)  $F_x$ (b)  $F_y$ (c)  $F_z$ 

**Figure 5.13:** Experimental and CFD results of forces for currents equal to the experimental current generation capacity of 75 % and 100 %, and five orientations of the Model Leg.

CFD and experimental results, and an  $R^2 = 0.993$ . Therefore the CFD results are considered validated for the simpler Model Leg.

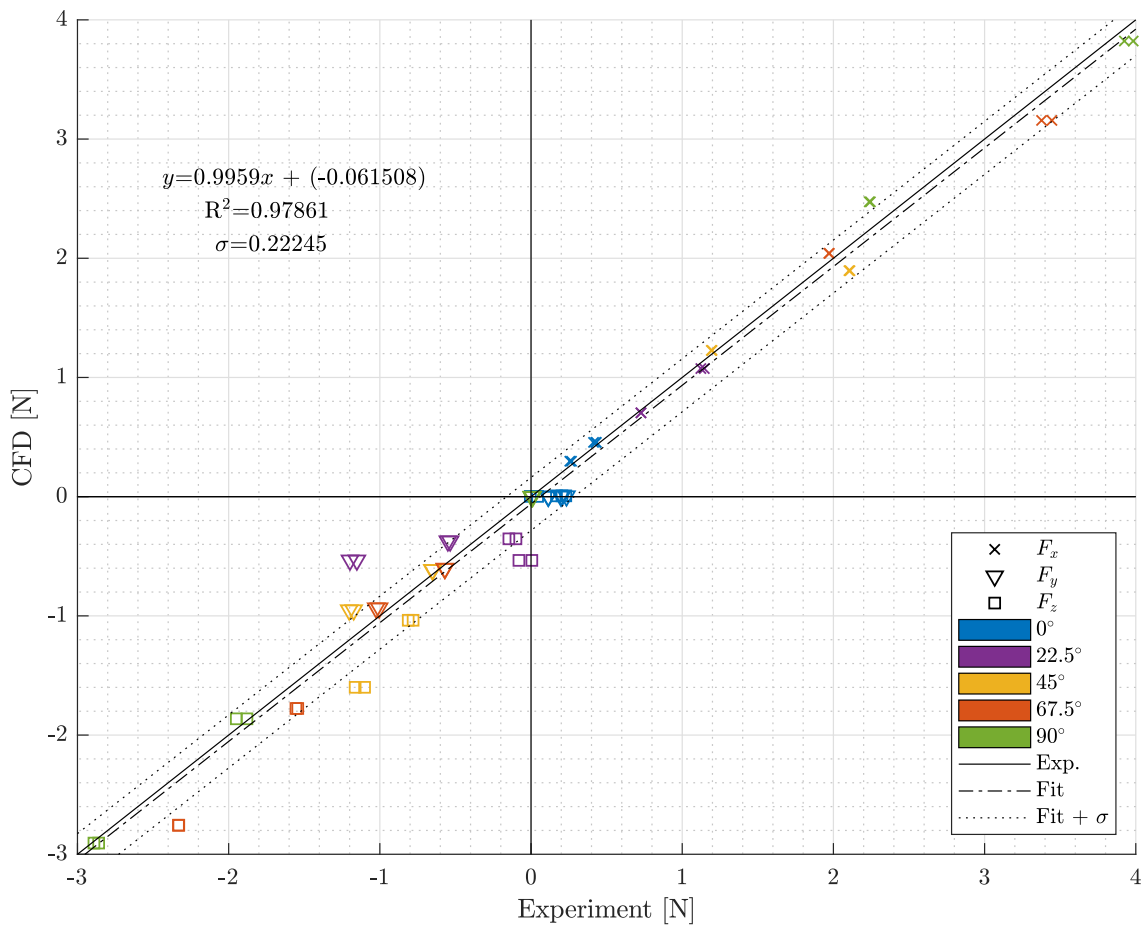


**Figure 5.14:** All scenarios' forces results from experiments vs. CFD analysis.

## 5.6 Summary

In this chapter CFD analysis have been performed on the Model Leg. The setup of the numerical models are set up to resemble the performed experiments. Sensitivity analysis have been performed on parameters that were subject to uncertainties;  $k$ ,  $\omega$  and the velocity inlet profile. The conclusion of the sensitivity analysis are that the  $[k, \omega]$  pair should be set to  $[1e-08, 1]$ , as higher  $k$ -values were more sensitive to change. There was no major difference in having a plug flow compared to the pre-determined velocity profile, yet the actual measured profile in the flume was used in the final CFD analysis in the experimental comparison to replicate experiment conditions as well as possible.

Sensitivity analysis were performed for the Model Leg to investigate effects of mesh refinement near the structure and wall functions. It was found that higher values of  $y^+$  resulted in up to 15-27 % deviation of  $F_x$  compared to when  $y^+ < 1$ , depending on the orientation. Wall functions did not effect the results significantly. But the effect was clearest for the  $0^\circ$  orientation, which is more shear drag dominated.

---

It was also found that changing the direction of the inlet flow did not yield the same results as when changing the model orientation. It is however recommended that future studies of a similar character investigate this potential, possibly on a circular domain, as meshing is found to be the biggest obstacle in CFD analysis.

The final results of the CFD-analysis of the Model Leg are encouraging, as they seem to match the results from the experiments quite well, as seen in Figure 5.14.

In conclusion it is judged that the setup, including the choice of solver, schemes and turbulence model, are suitable, as calculations match the experiments to a satisfactory degree.

---



## 6. Numerical validation - Full Model

This chapter aims to replicate the experimental results of the Full Model from Chapter 4 in CFD. This is done in order to validate the CFD model on a more complex structure than the Model Leg. The procedure will be of a similar manner as to that conducted in Chapter 5.

As the Full Model is a more advanced and computational demanding structure, the extent of CFD simulations are limited compared to the Model Leg. Yet, a convergence analysis containing only a few points is performed. Also, due to oscillations in the the steady solutions, the effect of using a transient solver is tested for a single CFD analysis of the Full Model, see section 6.4.

Aside from that, findings in Chapter 5 have been transmitted to the Full Model CFD analysis.

### 6.1 Computational domain and settings

The following domain, boundary conditions and settings are applied for the Full Model, see Figure 6.1.

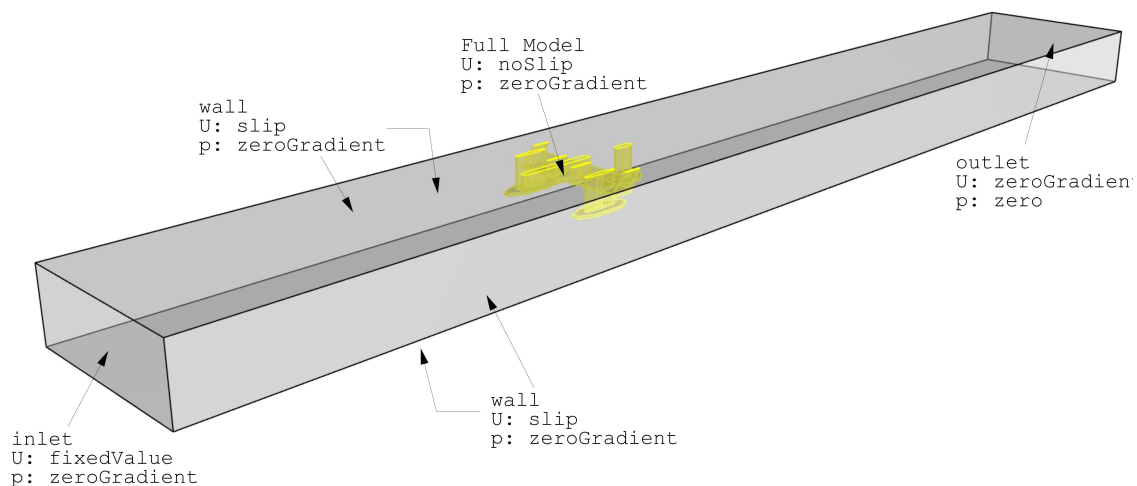


**Figure 6.1:** CFD domain, including OpenFOAM boundary conditions for pressure and velocity, for the Full Model

- The domain is similar to that of the Model Leg, as both experiments were performed in the flume at AAU. The water level height and width of the flume are therefore preserved. Due to the larger model size, the domain length is extended according to the length of the model,  $L_{ref,M} = 1.222$  m, see Figure 4.4. The domain length is therefore set to 11 m corresponding to  $3L_{ref,M}$  in front of the model and  $6L_{ref,M}$  behind the model. The influence of the domain length is examined in section 6.3
- The boundary conditions remain unchanged from the ones described in Chapter 5. I.e. the value of the inlet turbulence parameters are still  $k = 1e-8$  and  $\omega = 1.0$ .
- Slip conditions are applied on all walls, see Figure 6.1. This is done well knowing that the bottom plate of the tail end of the Full Model at  $90^\circ$  orientation is as close as 30 mm to the

Back wall, meaning that there might in fact be some viscous effects from the wall effecting the structure. However, as discussed in section 5.4.2 a no-slip condition would require a high mesh resolution at the wall surface in order to be resolved correctly. As good results were obtained with the slip conditions, the viscous effects from the wall are assumed negligible and therefore the no-slip condition is not used.

- The inlet velocity profile remains a logarithmic profile as determined in Chapter 3.
- The computational settings are unchanged from those given in section 2.4, except for the transient analysis described in section 6.4.

The Full Model is rotated around the same point as in the experiments. Thereby, the obtained moments should be directly comparable to the moments from the experiments.

### 6.1.1 Mesh

The domain is divided into three blocks in the  $x$ -direction of the flume. As opposed to the mesh for the Model Leg, The Full Model domain is not divided in the  $y$ -direction as the model is very wide relative to the width of the flume. Grading in the  $x$ -direction is applied in the blocks containing the inlet and outlet towards the centre block where the model is placed. The height of the domain is subdivided into 38 subdomains i.e.  $N_z = 38$ . Cells in the centre block are generated to have an aspect ratio  $\sim 1$ .

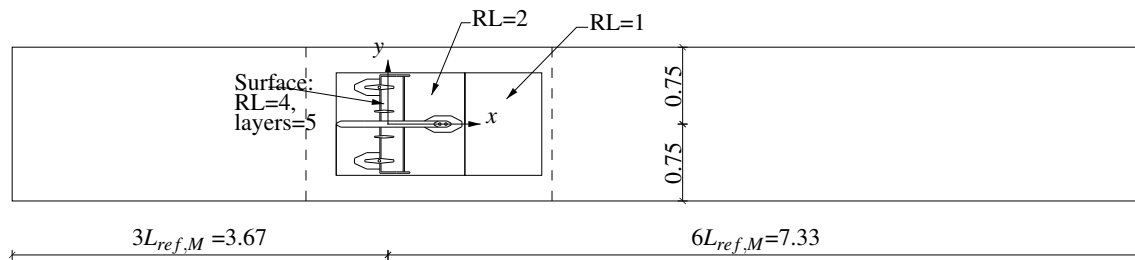


**Figure 6.2:** Full Model domain showing refinement regions for orientation of  $0^\circ$ . Units in meters.

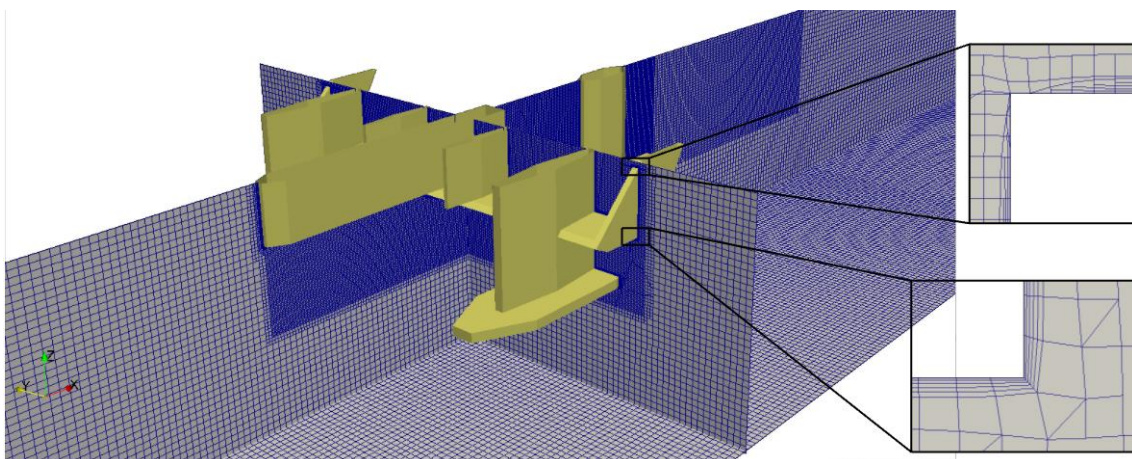
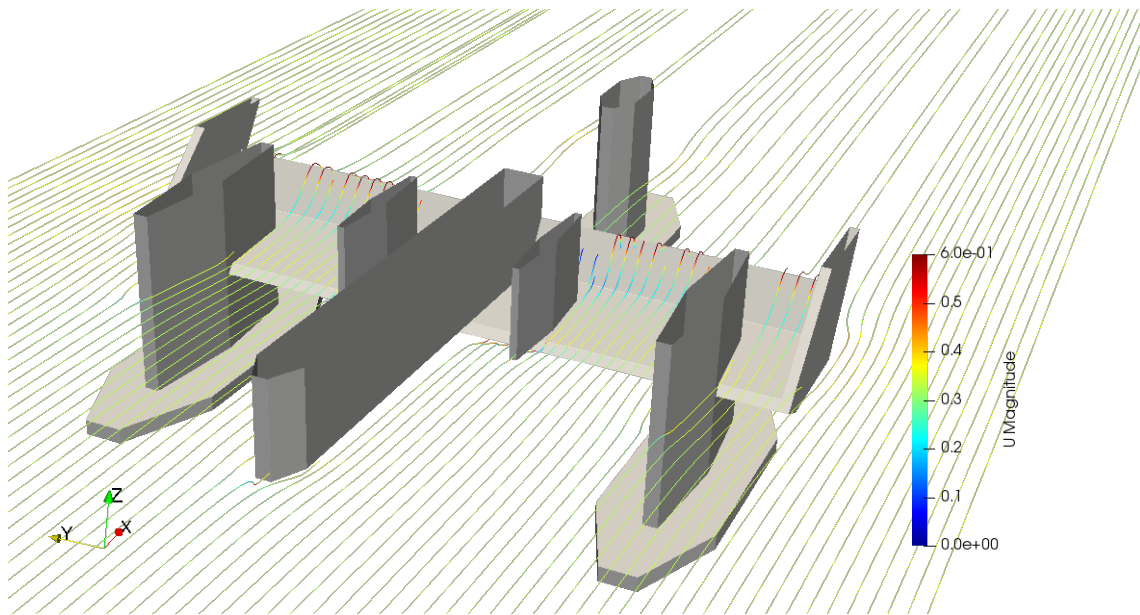


**Figure 6.3:** The mesh around the Full Model.

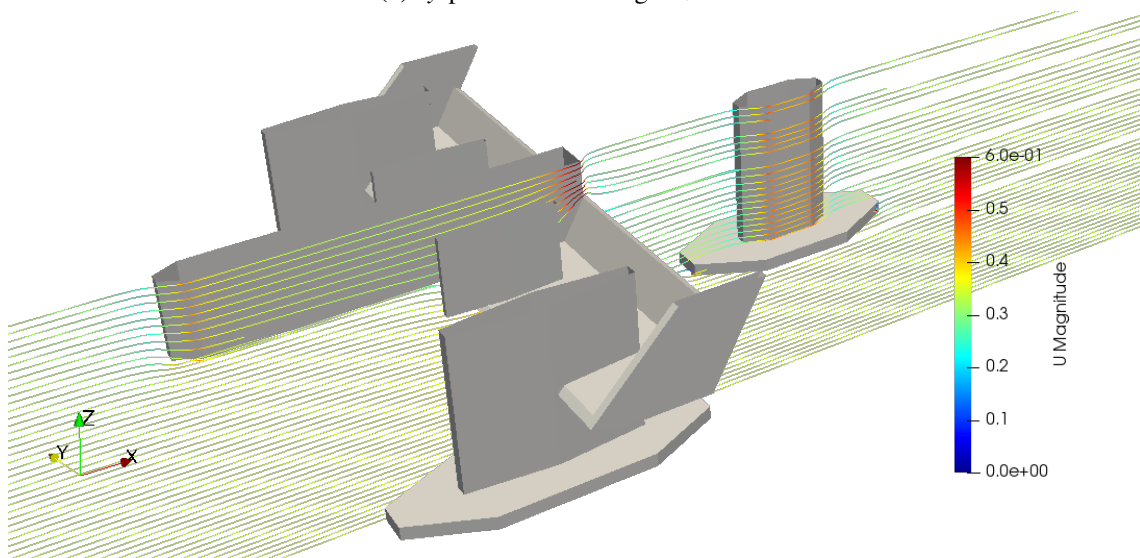
As with the Model Leg, a refinement region surrounding the model is applied to the Full Model to better be able to solve the flow property gradients near the model, see Figure 6.2. At the surface the refinementLevel is increased further and addLayers is applied with 5 layers to obtain a  $y^+ < 1$ .

The mesh consists of 27-31 million cells depending on orientation, which is roughly 7 times more than for the Model Leg. Figure 6.3 shows the mesh in the near region of the model.

## 6.2 General flow description



(a)  $xy$ -plane with seeding at  $z=0.175$ .

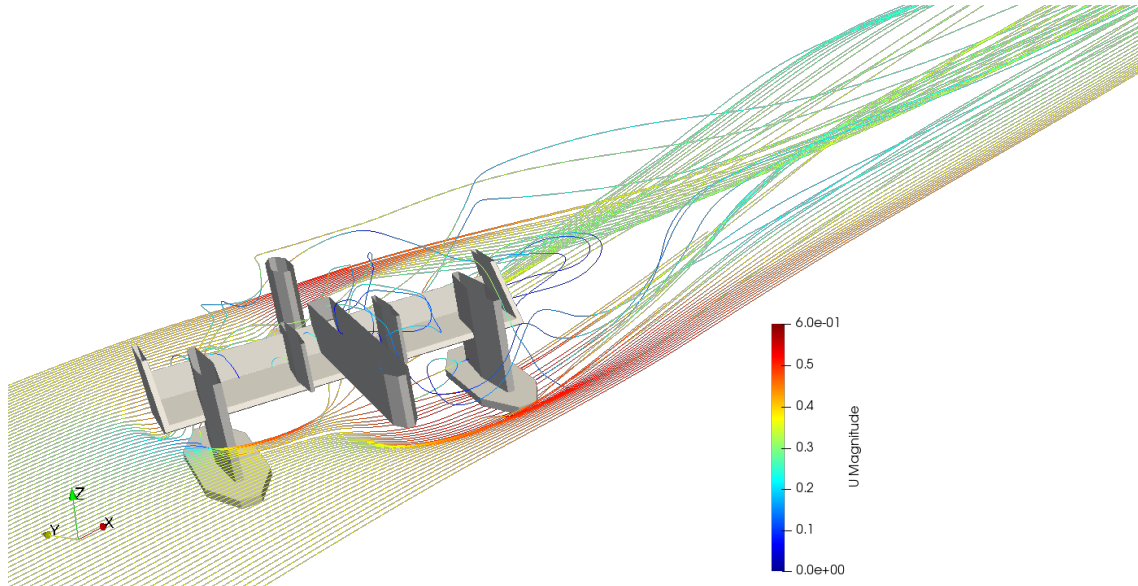


(b)  $xz$ -plane with seeding at  $y=0$ .

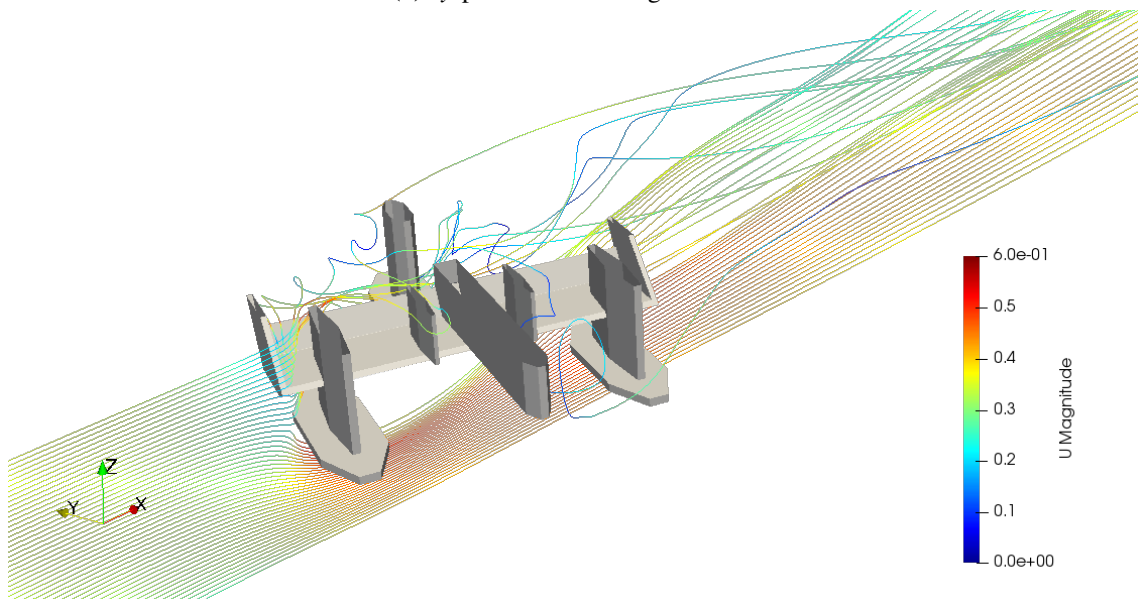
**Figure 6.4:** Velocity magnitude along streamlines for Full Model,  $\theta = 0^\circ$ .

In Figure 6.4 streamlines along the Full Model for  $\theta = 0^\circ$  are shown. It appears that the structure for this orientation is fairly streamlined meaning that large separation zones do not occur.

The flow is accelerated when passing the wing as expected. This acceleration might be greater than in reality since the CFD domain is modelled with a cap instead of a free surface.



(a)  $xy$ -plane with seeding at  $z=0.1$ .



(b)  $xz$ -plane with seeding at  $y=0.1$ .

**Figure 6.5:** Velocity magnitude along streamlines for Full Model,  $\theta = 67.5^\circ$ .

In Figure 6.5 streamlines along the Full Model for  $\theta = 67.5^\circ$  are shown. Compared to Figure 6.4 the flow is much more separative and complex. When flow passes the structure, cavities are formed in front of the wing, causing separation and giving rise to a surging force.

The tail leg at  $67.5^\circ$  is no longer in the shadow of the rest of the platform. It is thereby directly subjected to the current and resembles the Model Leg at this orientation. Separation occurs behind the leg, causing an eccentric force in the  $x$ -direction, which thereby also contributes to the yawing moment.

### 6.3 Convergence analysis

As described in section 6.1, the geometry of the Full Model is larger, more complex and requires an extended domain leading to a significant increase in cells, if the effects present in the viscous sub-layer still are desired to be modelled. The computational time is therefore substantially increased. For this reason, only a limited amount of convergence analysis are performed for the Full Model.

The mesh resolution is analysed for two different values of  $N_z$  i.e. 38 and 41. Convergence of the domain length is examined by extending the domain by 6 m, 2 m in front of the model and 4 m behind.

The deviations of the simulations from the experimental results, for the different meshes are shown in Figure 6.6. It appears that there are some small variations for the different mesh resolutions, which might indicate that the mesh is not fully converged. However, the variation might also be a consequence of the fact that the simulations are not converging towards a constant value as small oscillations are occurring, see Figure 6.7(a). This makes it difficult to estimate a representative value for the simulations with the used method, described in Appendix F.

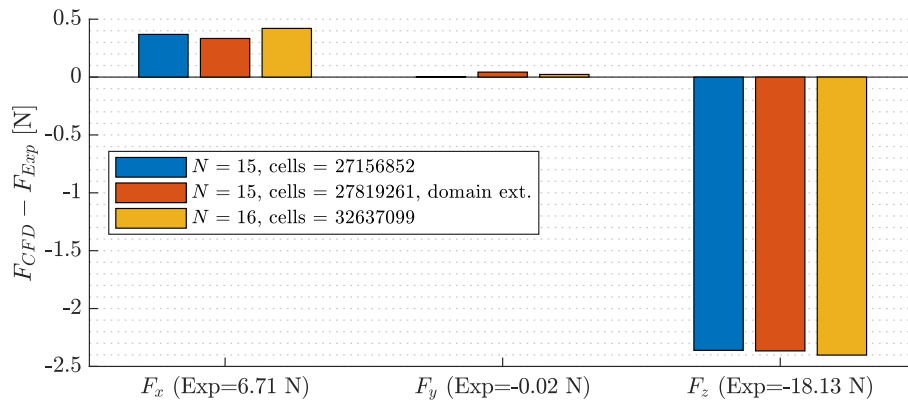


**Figure 6.6:** Convergence of forces for Full Model when varying amount of cells, determined by  $N_z = [15 : 16]$ .

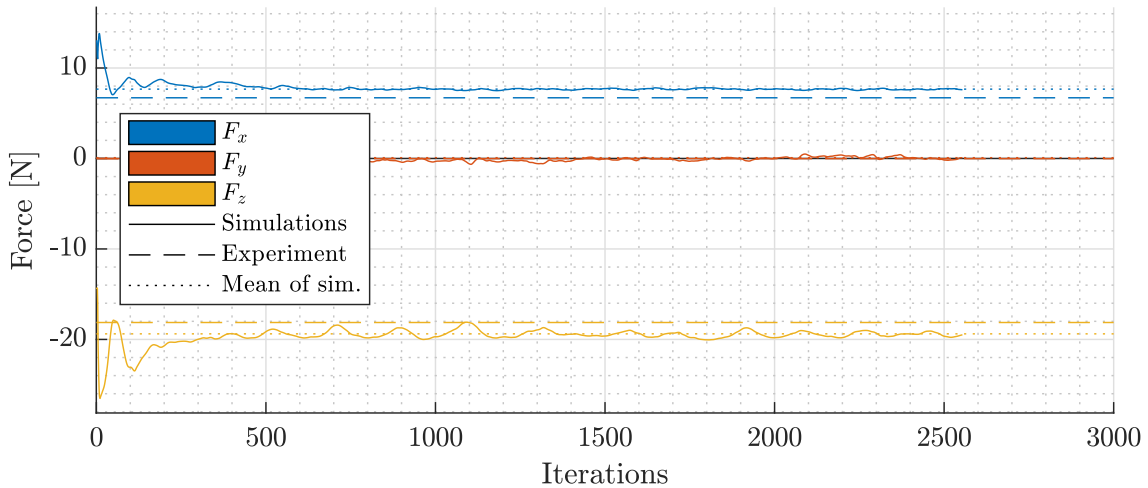
Nevertheless, the small variations between mesh sizes are in the order of  $1e-2$  N, or less than 1 % of the experimental force results. This is judged to be a negligible difference. It is therefore chosen to run simulations for the different angles with  $N_z = 38$ .

### 6.4 Transient analysis

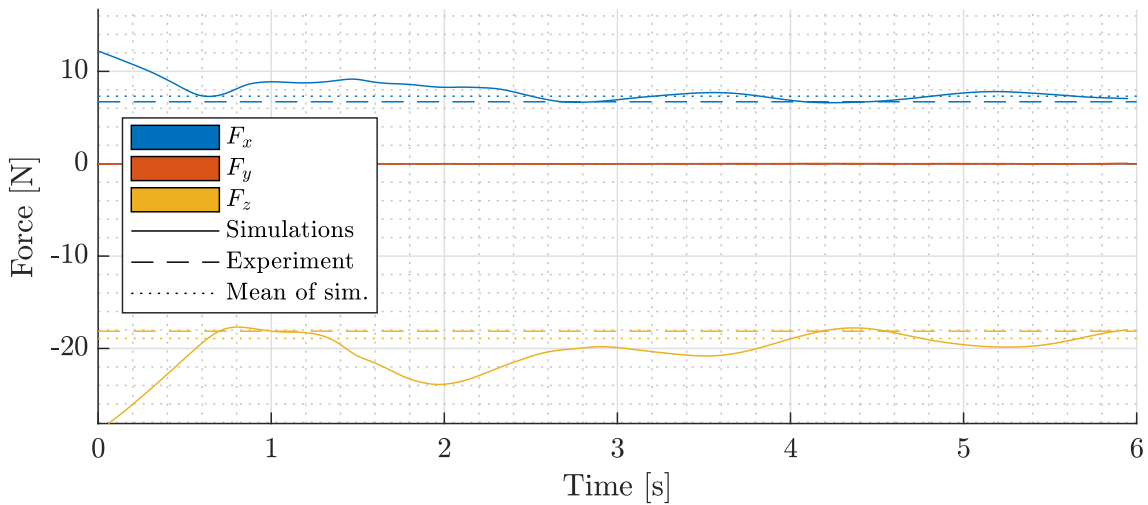
It was observed during the convergence analysis that the forces and moments oscillates over the iterations, as shown in Figure 6.7(a). The oscillations indicate that the flow problem might be

a non-steady problem, where a non-steady solver should be applied. For this reason a transient simulation has been run with the unsteady solver `pimpleFoam`, see Figure 6.7(b).

For this analysis, the background mesh is unchanged, so the refinement parameter  $N_z = 38$ . However, extra refinement at the surface is not applied for this simulation as it will cause the time step,  $\Delta t$ , to be very small for a desired Courant number of  $Co = 0.5$ . As a result of this  $y^+ \sim 60$ . These identical conditions have been run with both a `simpleFoam` and `pimpleFoam` solver, see Figure 6.4. More detailed settings for the unsteady simulation are found in Appendix B.



(a) Steady simulation run with `simpleFoam`.



(b) Transient simulation run with `pimpleFoam`.

**Figure 6.7:** Transient analysis simulations.

It is assumed that the unsteady simulations has reached a steady oscillation at 4.5 seconds. The simulation should have been run for longer, but had to be stopped due to a project deadline. The results of the transient simulation shows that the flow problem does in fact vary in time. It is also found that the transient response oscillates around almost the same mean value as calculated in the steady state solution. The calculated values are  $F_x = 7.66$  N for steady and  $F_x = 7.31$  N for unsteady.

Due to the similar results obtained between the two solvers, it is concluded that the `simpleFoam` solver is applicable for the simulations of the Full Model.

It is further noticed that for the steady solution, the increase in  $y^+$  yielded a result of  $F_x$  that differs more from the experiment (+14 %) than when  $y^+ < 1$  (+6 %).

## 6.5 Experiment comparisons

Simulations have been made with the `simpleFoam` solver to determine the forces and moments acting on the Full Model at all orientations investigated in the experiments.

From Figure 6.8 it can be seen that there is a very good correlation between CFD and experimental results for especially the forces of interest for the yawing moment,  $F_x$  and  $F_y$ .

It can be seen from Figure 6.8(b) that the rotated shape of the structure ( $>0^\circ$ ) initially contributes with a positive yawing moment. Though, as the tail end of the platform comes into view with respect to the current direction ( $\geq 45^\circ$ ), the forces acting on the tail end starts to counter these initial effects. An equilibrium orientation thereby seems to occur between  $45^\circ$  and  $67.5^\circ$ .

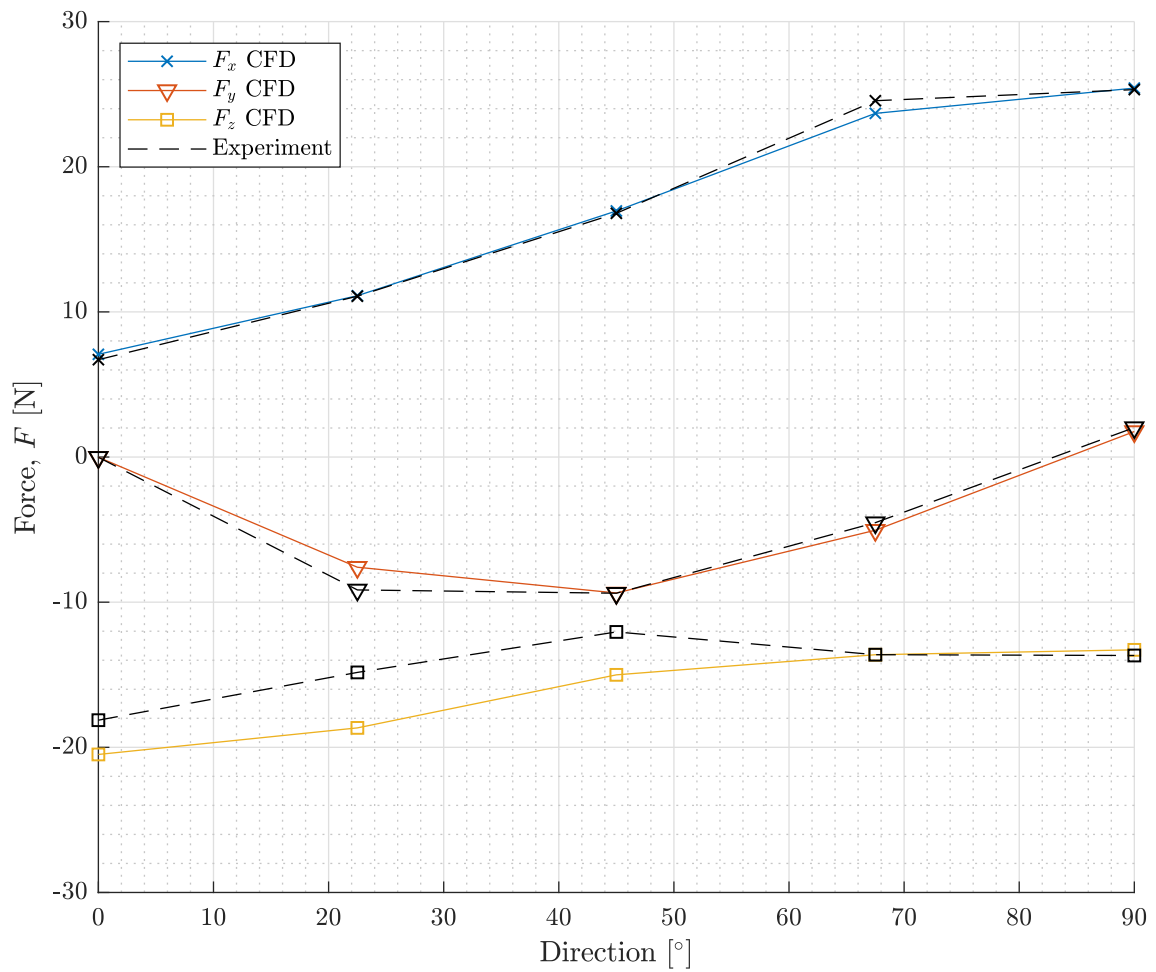
## 6.6 Summary

It was found that the results from the CFD analysis matched the experimental results very well for the Full Model. The model is therefore considered applicable for complex P80 structure.

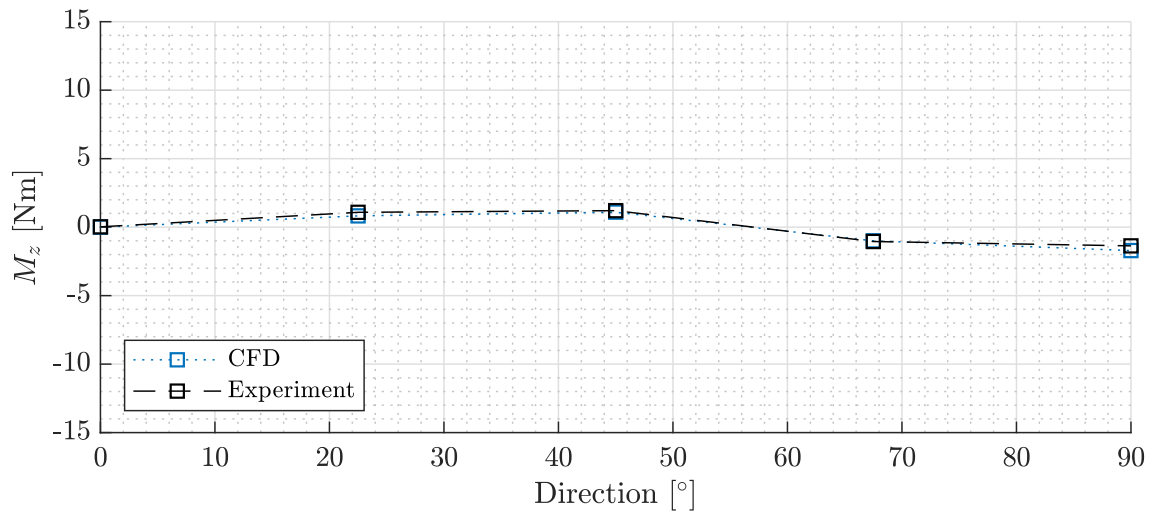
A comparison of a steady and non-steady solution was also performed in this chapter. The findings of this study verified that a steady solver is applicable for the flow problems in this report.

Furthermore, it has been concluded that a domain size of  $3L_{ref,M}$  in front and  $6L_{ref,M}$  behind the model is sufficient.

---



(a) Forces

(b)  $M_z$ **Figure 6.8:** CFD results compared to experimental results.

## 7. Analysis of FPP P80

In this chapter the CFD analysis of the current forces acting on the P80 is presented, with current directions spanning from  $0^\circ$  every  $22.5^\circ$  to  $180^\circ$  to cover a wide range of angles of attack. All the current directions are simulated with a current velocity of 1 m/s, resulting in a Reynolds number of  $\sim 5e7$ . Also, drag coefficients are estimated for each of the analysed orientations.

The P80 is shown in Figure 7.1, and has the overall dimensions shown in Table 7.1. It should be noticed that wave paddles are present in the P80. These are assumed to be in a fixed position, as is rest of the structure.

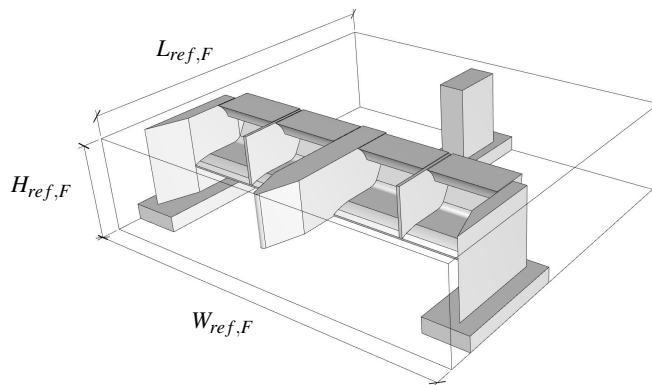


Figure 7.1: P80.

Dim.	Length
$H_{ref,F}$	24.0 m
$W_{ref,F}$	102.7 m
$L_{ref,F}$	88.3 m

Table 7.1: P80 dimensions.

It was not possible to perform a convergence analysis on CFD models of the P80 due to a considerable amount of time spent on remedying meshing issues. These issues and how they have been handled are explained in further detail in section 7.1.1.

All the CFD results of the forces and moments working on the structure are presented for the different current directions in section 7.3. The moments are calculated around two points; the mooring point and a point of interest for Floating Power Plant, as it is the origin in one of their own models. The latter point is referred to as the FPP origin, see Figure 7.2.

As no experiments have been made on the P80, the results will be compared in the form of drag coefficients to a rough estimate based on Det Norske Veritas, 2010 in section 7.4.

### 7.1 Computational domain

The computational domain attempts to replicate the conditions at sea.

- The domain is created to extend  $4W_{ref,F}$  in front of the structure,  $4W_{ref,F}$  to the side and  $8W_{ref,F}$  times behind. As it was observed in previous simulations of the Full Model that the influence of the structure did not reach far in the  $z$ -direction, the domain only extends to double the submerged depth of the P80 in this direction,  $2H_{ref,F}$ .

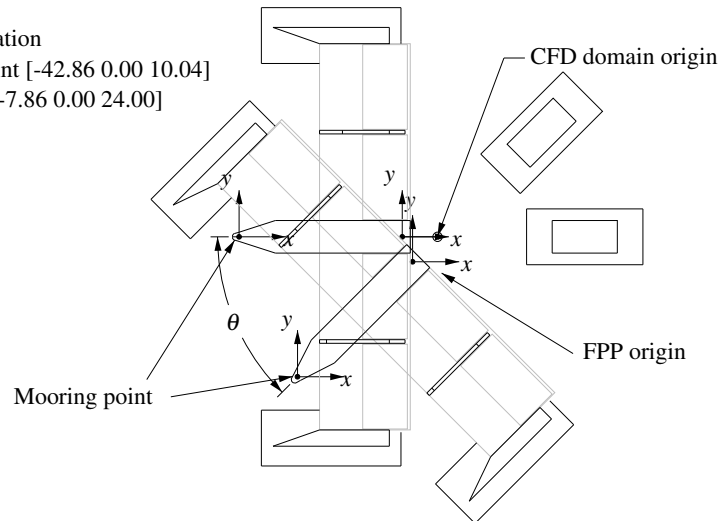


**Figure 7.2:** Position of mooring point, and coordinate system for different current directions.

- Slip conditions are applied on the sides normal to the current direction, as the P80 would be placed in open waters.
- The inlet turbulence parameters  $[k, \omega]$  are  $[8.78e-11, 8.33e-3]$ . These are calculated based on the recommendations made by Menter, 1994 as in the numerical validation chapters.
- The inlet velocity profile is modelled as a plug flow of 1 m/s, as requested by Floating Power Plant.
- The computational settings in Table 2.4 are retained. Due to simulation instability, changes concerning schemes and limiters are made. The changes are presented directly in Appendix B and listed below.
  - 2. order upwind scheme on the convective term for velocity are changed to 1.order for better stability but at the expense of accuracy.
  - Limiters for the laplacian and surface normal schemes are used with a value of 0.33 instead of 1.
  - Non-orthogonality correction are used
  - Relaxation factors have been reduced.

### 7.1.1 Mesh

The mesh is divided into nine blocks; three in both the  $x$ - and  $y$ -direction, which are shown with dashed lines in Figure 7.3. Grading is applied to the outer blocks towards the centre block, wherein the structure is placed. An aspect ratio of  $\sim 1$  is ensured in the centre block.

A square refinement region with  $RL = 2$  surrounds the structure and follows the P80 when rotated. In the wake of the structure another refinement region is defined with  $RL = 1$ . At the surface of the structure, the cells are further refined to  $RL = 4$  and 5 layers are added to lower the  $y^+$ -value.

Apart from having a geometrically much larger domain - approximately 100 times bigger than the Full Model - the meshing near the structure would also have to be twice as fine as for the experimental models to achieve a  $y^+ < 1$ , according to equations shown in appendix A.3. As it was

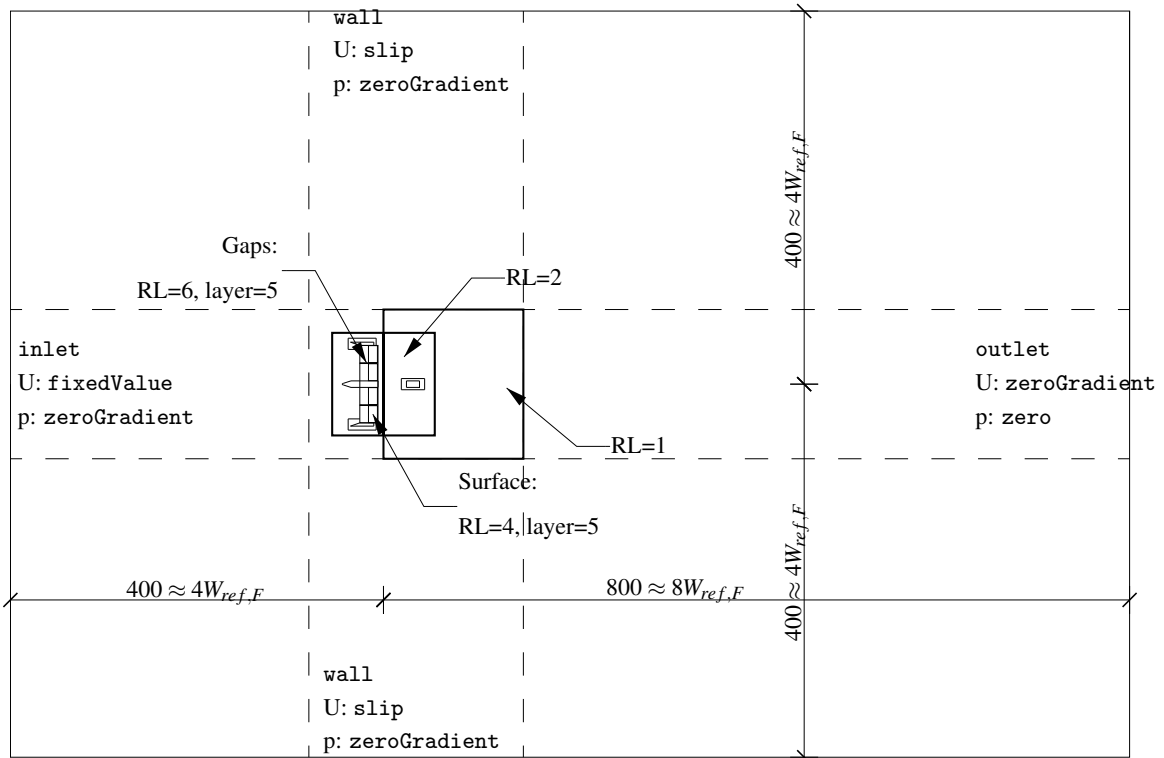


**Figure 7.3:** P80 domain showing the refinement regions for orientation of  $0^\circ$ . Units in meters. Boundary conditions are also shown. Top and bottom boundaries are also slip and zeroGradient.

not possible to create such a fine mesh due to computational requirements and time limitations, the flow problem for the P80 has been resolved with a  $y^+ \approx 150$ .

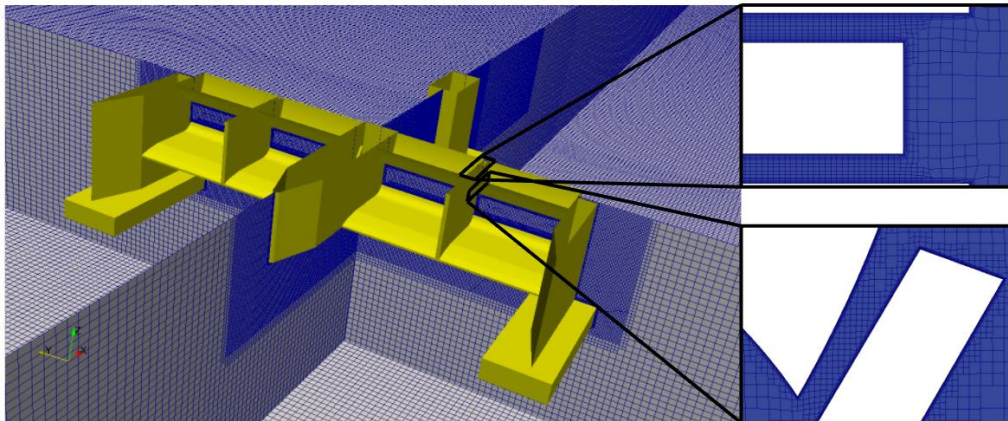


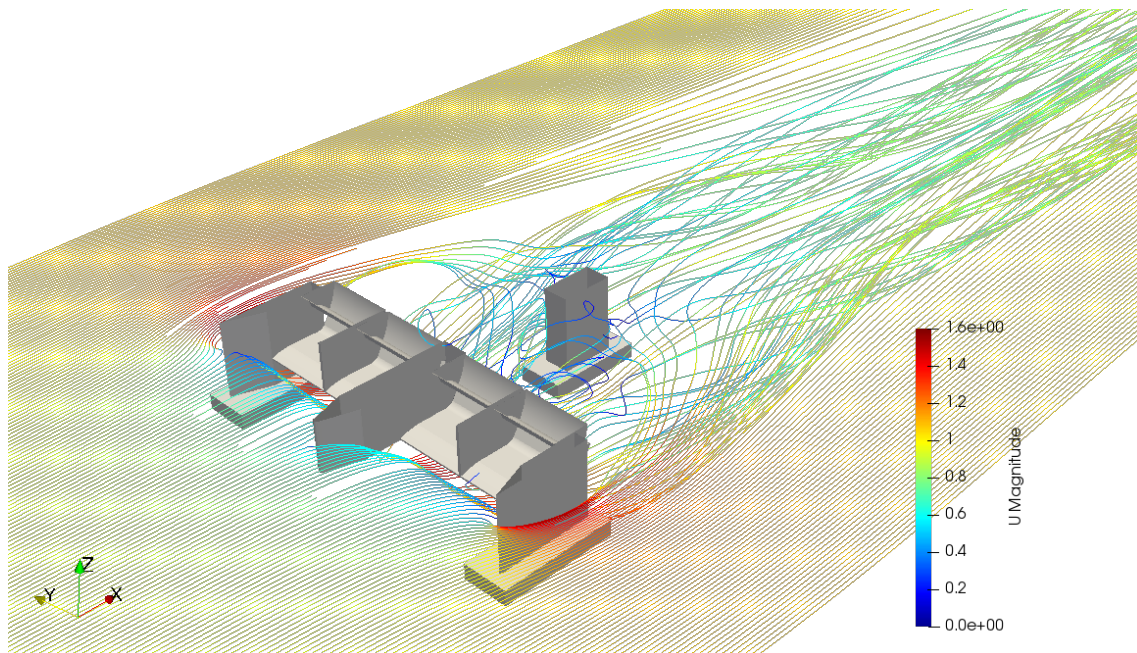
**Figure 7.4:** Mesh of P80.

Despite this setup of the mesh, issues occurred for the orientations between  $0^\circ - 90^\circ - 180^\circ$ . Especially, skew cells occurred at sharp angles of the geometry, which would cause the simulations to diverge.

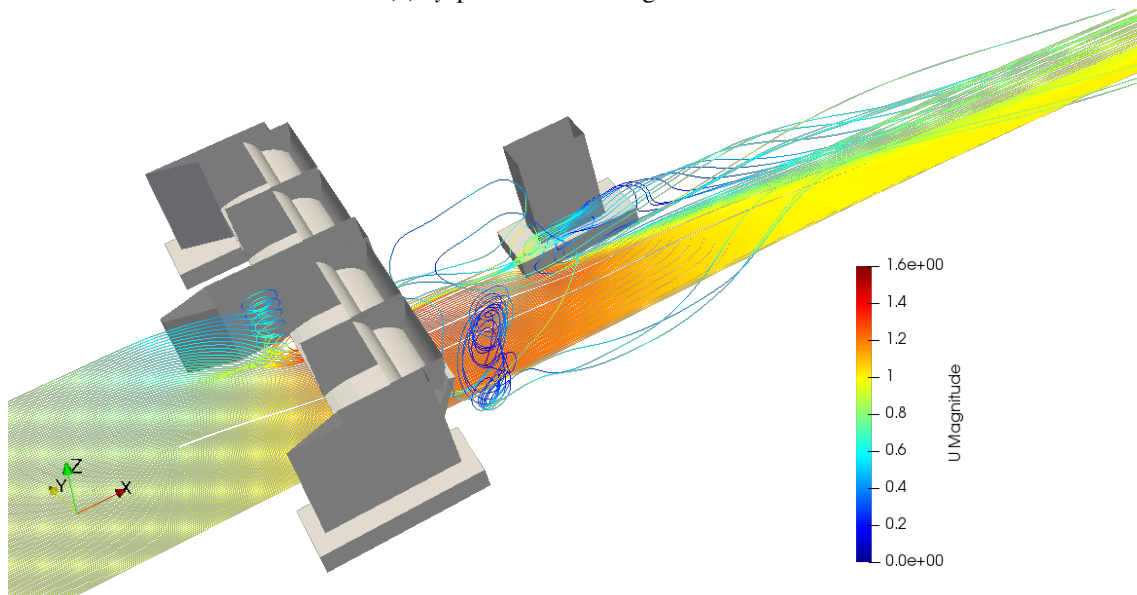
Therefore, measures were made in order to fix these skew cells. Sharp angles have been smoothed in the input geometry. Refinement boxes have been applied in gaps caused by the appearance of the wave absorbers, see Figure 7.4.

## 7.2 General flow description

The effect of introducing the wave paddles to the design has changed the general flow. When the P80 is facing the current head-on, practically all of the current will be directed either around or below the enclosed area that the wave paddles create, see Figure 7.5. For the Full Model without the paddles the flow would run over the shelf. This difference would result in a relatively larger downforce on the P80 compared to the Full Model.



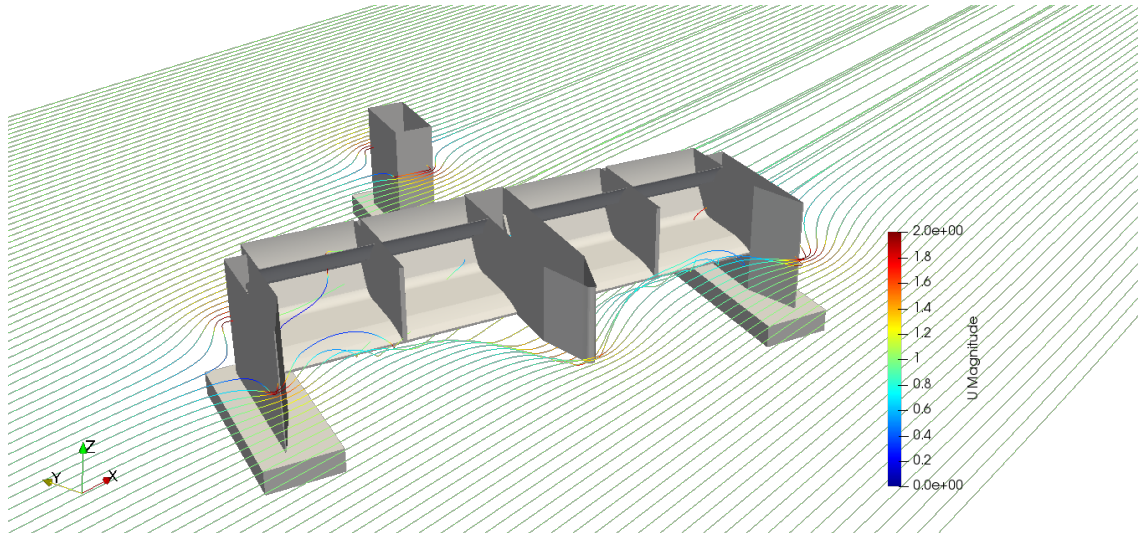
(a)  $xy$ -plane with seeding at  $z = 14$ .



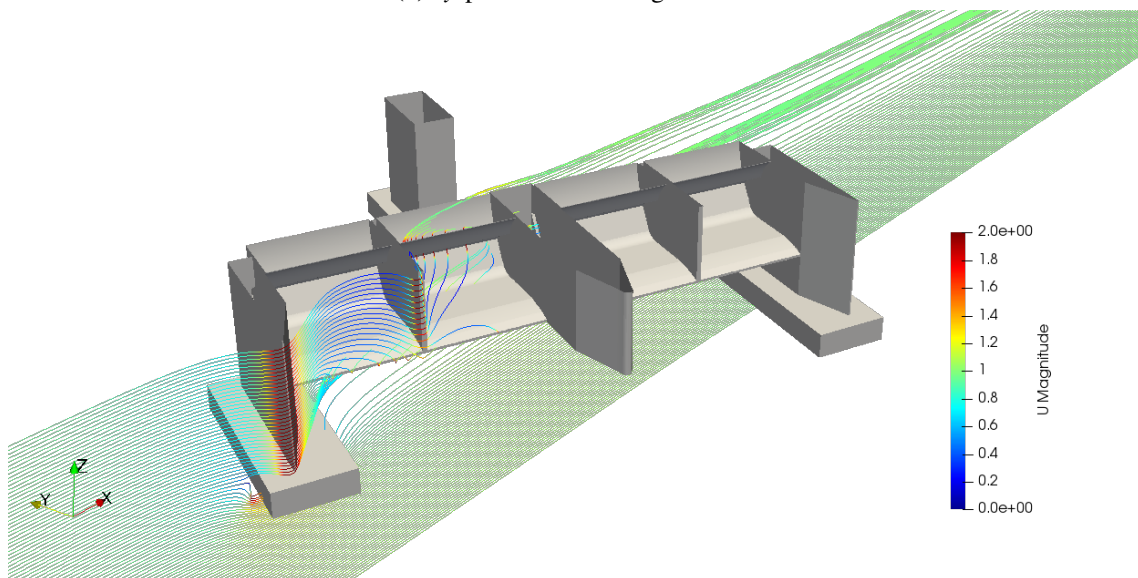
(b)  $xz$ -plane with seeding at  $y = -2$ .

**Figure 7.5:** Velocity magnitude along streamlines for P80,  $\theta = 0^\circ$ .

The tail end is in lee of the wave paddles and shelf, as well as being situated in the separation zone. The forces on the tail end will therefore be lesser at this orientation. On the other hand, the enclosed area acts as a large blunt surface, which causes a great deal of separation and large pressure drag. This will result in a large  $F_x$ . At  $67.5^\circ$  there is a lesser degree of separation downstream of the



(a)  $xy$ -plane with seeding at  $z=16$ .



(b)  $xz$ -plane with seeding at  $y=-10$ .

**Figure 7.6:** Velocity magnitude along streamlines for P80,  $\theta = 67.5^\circ$ .

current, due to a smaller frontal area in the streamwise direction. At this angle, the tail end is no longer in lee of the wave paddles, resulting in a higher exerted force on it. This will result in a higher yawing moment, due to the large moment arm from the tail end to the mooring turret.

### 7.3 Results

The results of the CFD analysis are shown in both Table 7.2 and Figure 7.7 and 7.8. All simulations except  $0^\circ$ ,  $90^\circ$  and  $180^\circ$  have been run with 1. order schemes to stabilise the simulations. Thereafter, using the 1. order simulations as a starting guess, 2. order schemes are run to get more accurate results. For  $67.5^\circ$  however, the 2. order results had not converged, which can be seen from its larger deviation between the 1. and 2. order results. Therefore, the 1. order result for  $67.5^\circ$  is used in further analysis.

When comparing the P80 to the small scale Full Model, it is found that the tendencies from  $0^\circ$  to  $90^\circ$  are almost opposite, in that  $F_x$  decreases from  $0^\circ$  to  $90^\circ$  for the P80 and vice versa for the Full Model. The difference here lies in that the P80 includes wave paddles, which more or less blocks any flow through the structure at  $0^\circ$ . Also, the legs in the P80 are more blunt as opposed to a more rounded shape in the Full Model. The effect of these factors are that  $F_x$  becomes much larger for  $0^\circ$  with diminishing effect towards  $90^\circ$ , which is therefore seen as being a lower value.

Beyond  $90^\circ$   $F_x$  is generally lower. This is because the back wall is at an angle to the flow, making the back of the structure more streamlined than the front.

At  $0^\circ$  and  $180^\circ$ ,  $F_y$  should be equal to zero due to symmetry. An explanation to the CFD results not showing a zero value is due to uneven meshing. The change of direction of  $F_y$  between  $45^\circ$  to  $67.5^\circ$  could be a result of the wave paddles and shelf being more parallel to the flow, and thereby less separation. This effect can be compared to the stalling phenomena of an airfoil.

The yawing moment,  $M_z$ , around the mooring turret is largest when the current acts on the side of the structure. This is due to the back leg being subjected directly to the current forces, which also has a large moment arm of  $\sim 80$  m. As a consequence of the P80 being moored at the fore part of the hull, the yawing moment is consistently negative, meaning that it will always try to orientate inline with the current.

The change in  $F_z$  from when the platform is orientated at  $45^\circ$  to  $67.5^\circ$  is large. When looking at Figure 7.5(a) and Figure 7.6(a) it appears that at  $0^\circ$  the flow is directed underneath the structure causing a lot of separation leading to a force in the  $z$ -direction. In contrast, the  $67.5^\circ$  the flow is going around the platform.

The forces in the  $z$ -direction were always negative. This would mean that with a steady current, the FPP would be pulled down until buoyancy equilibrium is obtained. The result of this would be a larger submerged area, which would increase the current drag on the structure. However, the effect of the negative  $F_z$  is estimated to increase the submerged depth by a matter of centimetres, and should therefore not have a great influence on results.

When examining these results, it should be kept in mind that the simulations were run with a  $y^+ \approx 150$ . In section 5.4.3 it was found that a  $y^+ \approx 150$  yielded results of  $F_x$  which differed with 15 % - 27 %, compared to when  $y^+ < 1$ .

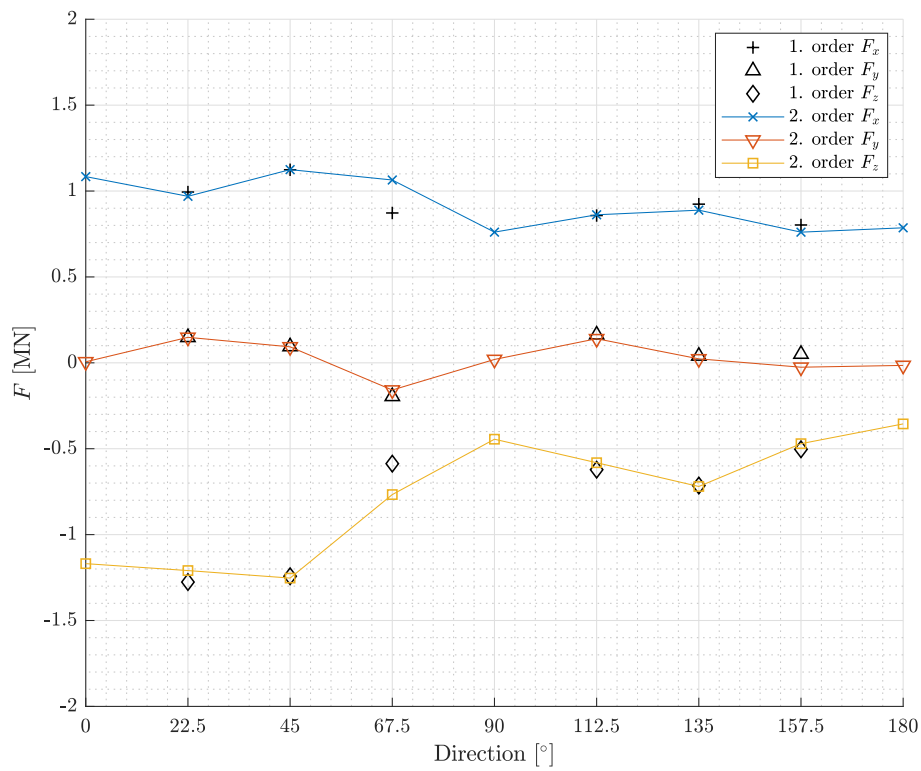


Figure 7.7: Forces acting on P80.

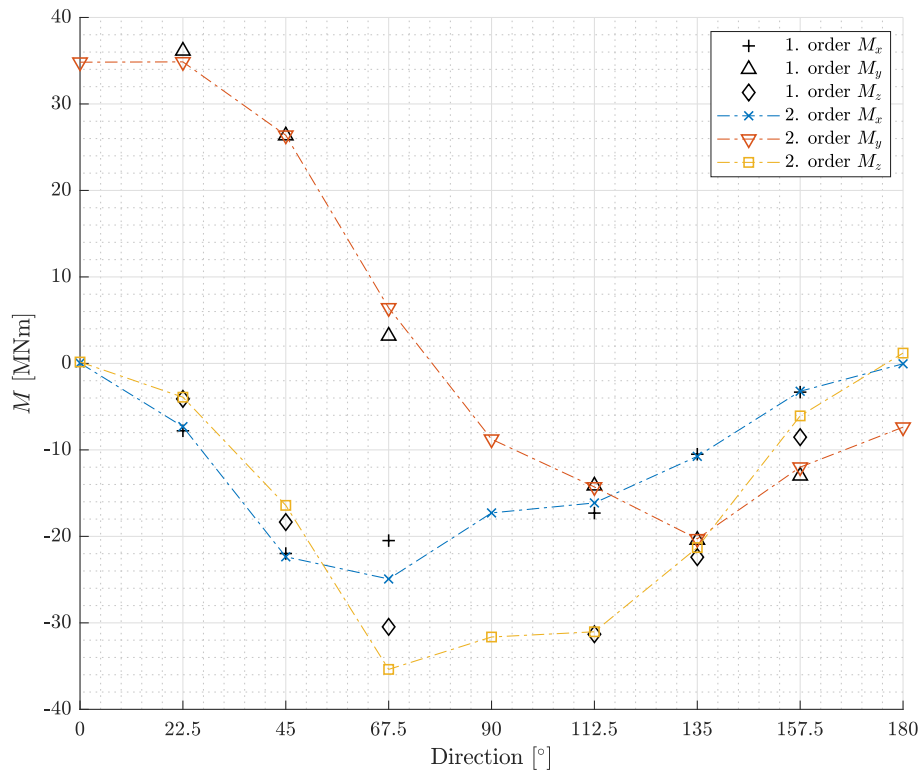


Figure 7.8: Moments acting on P80 around mooring point.

$\theta$ [°]	Or.	Force [MN]			Moment (FPP O.) [MNm]			Moment (mooring) [MNm]		
		$F_x$	$F_y$	$F_z$	$M_x$	$M_y$	$M_z$	$M_x$	$M_y$	$M_z$
0.0	1									
	2	1.08	0.01	-1.17	0.12	-21.22	-0.05	0.04	34.83	0.16
22.5	1	0.99	0.15	-1.28	11.38	-19.01	4.44	-7.79	36.14	-4.10
	2	0.97	0.15	-1.21	10.94	-17.77	4.27	-7.32	34.87	-3.91
45.0	1	1.12	0.09	-1.24	10.02	-20.01	7.08	-21.98	26.33	-18.35
	2	1.12	0.09	-1.25	10.32	-20.51	8.89	-22.36	26.38	-16.41
67.5	1	0.87	-0.20	-0.59	-4.27	-16.69	0.36	-20.49	3.18	-30.46
	2	1.06	-0.16	-0.77	-2.61	-18.97	0.83	-24.93	6.42	-35.38
90.0	1									
	2	0.76	0.02	-0.44	-1.45	-19.39	-5.01	-17.29	-8.76	-31.64
112.5	1	0.86	0.16	-0.62	5.07	-17.79	-1.41	-17.31	-14.15	-31.31
	2	0.86	0.14	-0.58	4.62	-18.53	-1.29	-16.13	-14.29	-31.03
135.0	1	0.92	0.04	-0.71	7.71	-15.71	1.42	-10.50	-20.43	-22.40
	2	0.89	0.02	-0.72	7.38	-14.89	1.27	-10.75	-20.29	-21.29
157.5	1	0.80	0.05	-0.50	4.10	-7.96	3.84	-3.32	-13.00	-8.53
	2	0.76	-0.03	-0.47	2.72	-7.41	3.31	-3.22	-11.99	-6.07
180.0	1									
	2	0.79	-0.01	-0.36	-0.22	-5.92	0.70	-0.05	-7.37	1.19

**Table 7.2:** Forces and moments on P80. Or. stands for order of the used schemes, which is either first or second. Moments are given at the FPP origo of supplied drawing and at the supplied mooring point. Moments at mooring for 0° are not available due to human error in the pre-programming of this simulation.

## 7.4 Estimation of drag coefficients

In this section the drag coefficients on the P80 are estimated. This is done both by calculating the drag coefficients from the forces obtained in the CFD results in section 7.3, and by a simple rough estimation of the drag coefficients based on Det Norske Veritas, 2010 for comparison.

The drag coefficients are calculated from equation (7.1).

$$F_i = 0.5\rho C_{D,i} A_{ref} |U|U \quad (7.1)$$

The  $i$  index denotes the forces/drag coefficient in either the current direction or transverse to it ( $x$  or  $y$ ), where the velocity,  $U$ , is always in the current direction. The reference area,  $A_{ref} = 2364 \text{ m}^2$ , is in this report determined as the simplified frontal area of the P80, i.e. the total width,  $W_{ref,F}$ , times the submerged depth,  $H_{ref,F}$  see Figure 7.1.

### 7.4.1 Det Norske Veritas drag coefficients

In Det Norske Veritas, 2010 Appendix E, drag coefficients are given for some simpler geometries such as ellipses or flat plates perpendicular to flow direction. As the P80 is a complex model

it would not be accurate to model it by simply e.g. a flat plate perpendicular to flow direction. Therefore, following inspiration by Thomsen, Ferri, and Kofoed, 2017, it is chosen to superimpose drag coefficients for different chosen elements from Det Norske Veritas, 2010 to create a better estimate of a global drag coefficient for the P80.

Thus, the P80 has been divided into parts, which resemble the cases in Det Norske Veritas, 2010, see Figure 7.9. Only an estimate of a drag coefficient in the  $x$ -direction,  $C_{D,x}$ , at  $0^\circ$  is determined in this way. At this angle,  $C_{D,y} = 0$  due to symmetry. It is calculated that  $C_{D,x} = 1.07$  for the P80..

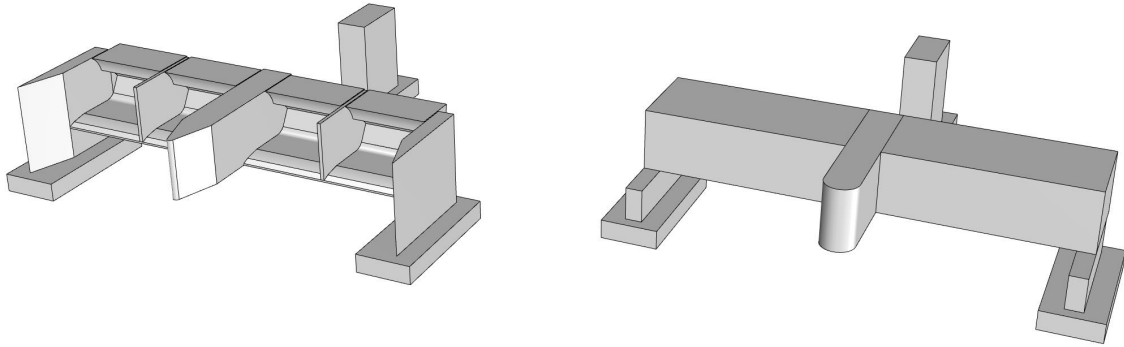


**Figure 7.9:** Geometries of actual and simplified P80.

Detailed calculations of this rough estimate for the drag coefficient can be found in Appendix G for the P80 as well as for the Full Model and Model Leg.

#### 7.4.2 CFD drag coefficients

The results are a direct product of the CFD analysis force results, which were discussed in section 7.3.

The drag coefficients are calculated by isolating  $C_{D,i}$  in equation (7.1), and thereby obtaining the results in Table 7.3. The drag coefficients are also presented in Figure 7.10 along with the rough estimate calculated from Det Norske Veritas, 2010. Only the highest order obtained CFD results are included, except the  $67.5^\circ$  orientation. The CFD estimated  $C_{D,x}$  is 25 % lower than the DNV estimate.

Dir.	$0^\circ$	$22.5^\circ$	$45^\circ$	$67.5^\circ$	$90^\circ$	$112.5^\circ$	$135^\circ$	$157.5^\circ$	$180^\circ$
$C_{D,x}$	0.89	0.80	0.93	0.72	0.63	0.71	0.73	0.63	0.65
$C_{D,y}$	0.00	0.12	0.08	-0.16	0.02	0.12	0.02	-0.02	-0.01

**Table 7.3:** Drag coefficients in  $x$  and  $y$  relative to current direction on P80, based on CFD results.

The estimated coefficients are only applicable to the exact structure supplied by Floating Power Plant. Any non-uniform change in scale of of the FPP would result in the estimated drag coefficients being invalid. As the drag coefficients on the P80 have only been determined for one size and one current velocity, it is not known whether a change in Reynolds number would result in a change of the value of the drag coefficients.

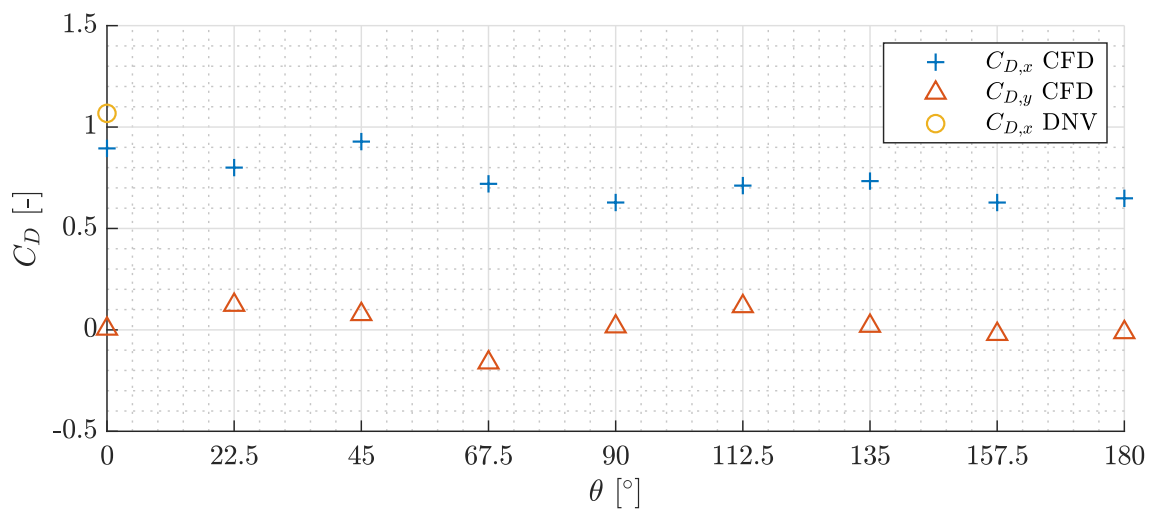


**Figure 7.10:** Drag coefficients in x and y relative to current direction on P80.

## 8. Conclusion

It was found that the velocity field in the flume varies depending on location in both the longitudinal and transverse direction of the flume. At the centre of the flume 8 m from the inlet the velocity profile in the direction parallel to the flume length was found to fit a logarithmic profile well. The velocity profile with the smallest standard deviation from the fitted profile was achieved when running the current generator at the max capacity of 50 Hz. Lower current generating capacities of 50 % and 75 % of the max capacity yielded more fluctuating mean velocities throughout the water depth. It was also found that the velocity profile was not constant across the width of the flume at any of the measured distances from the inlet. At a distance of 5 m and 11 m from the inlet a limited amount of measurements were made. However, these measurements did not show the velocity profile as having a well-fitted logarithmic shape in the direction parallel to the flume length.

The  $k - \omega$  SST turbulence model has shown to yield good results throughout the report when used with the values of the turbulent parameters recommended by Menter, 1994. Analysis performed on the Model Leg showed that a  $k$ -value in the order of magnitude of  $1e-3$  is sensitive to small changes of  $k$ .

From the numerical validation analysis it was found that a steady state solver was highly applicable to calculate the forces acting on the model of a FPP. Results from the CFD analysis on the Full Model showed a deviation of results ranging from 0 % - 6 % for the forces in line with the current direction and 0 % - 18 % for the forces transverse to the current direction.

The forces acting on the P80 were found to be in the range of 0.8 - 1.1 MN for the force in line with the current direction, and 0 - 0.2 MN for the force in the transverse direction to the current. It was also found that the value of  $y^+$  has a significant impact on results. In a sensitivity test performed on the Model Leg, the difference between a  $y^+ < 1$  and  $y^+ \approx 150$  was found to be up to 15 % to 27 % depending on the current angle of attack despite the use of wall functions. The Full Model CFD analysis, which predicted forces accurately when compared to the performed experiments, were performed with a  $y^+ < 1$ . The P80 was performed with a  $y^+ \approx 150$ . Therefore, it is advised to take the uncertainty regarding the higher value of  $y^+$  into account when using the determined drag coefficients. Ideally, simulations should be re-run with a  $y^+ < 1$  to increase the confidence of the results.

### 8.1 Further work

The authors have a few suggestions for future studies of a similar nature to this report.

A larger amount of the problems faced by the authors of this report were due to meshing, particularly of the P80. The P80 was meshed in the same way as the experimental models, i.e. a mesh for each orientation of the structure, and the inlet always coming from one rectangular boundary. This caused the formation of skew cells and high aspect ratios for orientations of the model that were not  $0^\circ$ ,  $90^\circ$  or  $180^\circ$ . Though these issues were resolved to a certain extent, it is recommended that future studies aim to create as small an amount of meshes as possible. This could be done by e.g.

---

creating a larger, possibly circular, domain, where it is possible to vary the direction of the inlet velocity, instead of the orientation of the structure.

In order to fully describe the current forces acting on the FPP, analysis should be made with different Reynolds numbers to ensure that the estimated drag coefficients hold for different velocities.

---

# References

- Aldegunde, Manuel, Juan J Pombo, and Antonio Garcia Loureiro, 2019, “Octree-based mesh generation for the simulation of semiconductor devices”. In:
- Carbon Trust, 2015, *Floating Offshore Wind: Market and Technology Review*. Tech. rep.
- Christiansen, Linea Højgaard and Sara Winther Lausten, 2017, “Optimisation of inlet for simultaneous current and wave generation in a wave flume”. MA thesis. Aalborg University.
- Clean Technica, 2018, *Hywind Scotland, World’s First Floating Wind Farm, Performing Better Than Expected*. last visited: 27/05/2019. URL: <https://cleantechnica.com/2018/02/16/hywind-scotland-worlds-first-floating-wind-farm-performing-better-expected/>.
- Det Norske Veritas, 2010, *Recommended Practice DNV-RP-C205 - Environmental conditions and environmental loads*. Appendix E - Drag coefficients. URL: <https://rules.dnvgl.com/docs/pdf/dnv/codes/docs/2010-10/rp-c205.pdf>.
- Energistyrelsen, 2019, *Eksisterende havvindmølleparker og aktuelle projekter*. last visited: 27/05/2019. URL: <https://ens.dk/ansvarsomraader/vindenergi/eksisterende-havvindmoelleparker-og-aktuelle-projekter>.
- esi, 2019, *OpenFOAM.com*. URL: <https://www.openfoam.com/documentation/>.
- EWEA, European Wind Energy Association, 2013, *Deep water - The next step for offshore wind energy*. Tech. rep.
- FPP, Floating Power Plant -, 2019, *Floating Power Plant - Invest in the future*. last visited: 27/05/2019. URL: <http://www.floatingpowerplant.com>.
- IEA, International Energy Agency, 2019, *Global Energy Statistics*. last visited: 26/05/2019. URL: <https://www.iea.org/statistics/>.
- Kitware, 2019, *ParaView*. URL: <https://www.paraview.org/>.
- Lykke Andersen, Thomas, 2018, *WAVELAB*. last modified 2018-12-17. URL: <https://www.hydrosoft.civil.aau.dk/wavelab/>.
- Menter, F. R., 1994, “Two-Equation Eddy-Viscosity Turbulence Models for Engineering Applications”. In: *AIAA 32.08*, p. 8.
- Munson, Okiishi, Huebsch, and Rothmayer, 2013, *Fundamental of Fluid Mechanics*. Seventh edition. John Wiley & Sons, Inc.
- NORTEK, 2019, *Vectrino*. URL: <https://www.nortekgroup.com/products/vectrino>.
- Rønby, Johan, 2019, *The current OpenFOAM landscape*. Presentation at DANSIS OpenFOAM seminar at AAU Copenhagen 27/03/2019.
-

- 
- Rosetti, Guilherme, Guilherme Vaz, and André Fajarra, 2012, “URANS Calculations for Smooth Circular Cylinder Flow in a Wide Range of Reynolds Numbers: Solution Verification and Validation”. In: vol. 5. ISBN: 9780791844922. DOI: 10.1115/OMAE2012-83155.
- Schunk, 2019, *FTsensor*. URL: [https://schunk.com/cn\\_en/gripping-systems/product/30862-FTn-gamma-si-65-5/](https://schunk.com/cn_en/gripping-systems/product/30862-FTn-gamma-si-65-5/).
- Thomsen, Jonas Bjerg, Francesco Ferri, and Jens Peter Kofoed, 2017, “Validation of a Tool for the Initial Dynamic Design of Mooring Systems for Large Floating Wave Energy Converters”. In: *Journal of Marine Science and Engineering*, p. 23.
- UN Environment, 2019, *Global Environment Outlook - GEO-6; Healthy Plant, Healthy People*. Tech. rep.
- Versteeg, H. K. and W. Malalasekera, 2007, *An Introduction to Computational Fluid Dynamics*. Second edition ISBN: 978-0-13-127498-3. Pearson Education.
- Weller, H.G., Gavin Tabor, Hrvoje Jasak, and Christer Fureby, 1998, “A tensorial approach to CFD using object oriented techniques”. In: *Computers in Physics* 12.
-



# Appendices

<b>A</b>	<b>Theory</b> .....	<b>65</b>
<b>B</b>	<b>Numerical settings</b> .....	<b>71</b>
<b>C</b>	<b>Flume velocity profiles</b> .....	<b>73</b>
<b>D</b>	<b>Force sensor</b> .....	<b>79</b>
<b>E</b>	<b>Forces from experiments</b> .....	<b>81</b>
<b>F</b>	<b>Simulation results</b> .....	<b>83</b>
<b>G</b>	<b>Drag coefficients from DNV</b> .....	<b>93</b>



# A. Theory

This Appendix describes the essential theory used in this report.

## A.1 Governing equations

The governing equations for time dependent, three dimensional fluid flow and heat transfer of a compressible Newtonian fluid are given in equation (A.1)-(A.7). In this non-linear, coupled system of seven equations, there are also seven unknown properties of the fluid flow. Density,  $\rho$ , pressure,  $p$ , temperature,  $T$ , internal energy,  $i$  and velocities in three directions,  $\mathbf{u} = [u; v; w]$ . All these properties are functions of time and space,  $(t, x, y, z)$ .

The flow problem investigated in this report is assumed to be an incompressible, steady-state, Newtonian fluid. These assumptions simplify the equation system (A.1)-(A.7) significantly and is explained in the following.

$$\text{Continuity} \quad \frac{\partial \rho}{\partial t} + \text{div}(\rho \mathbf{u}) = 0 \quad (\text{A.1})$$

$$x \text{ momentum} \quad \frac{\partial(\rho u)}{\partial t} + \text{div}(\rho u \mathbf{u}) = -\frac{\partial p}{\partial x} + \text{div}(\mu \text{ grad}(u)) + S_{Mx} \quad (\text{A.2})$$

$$y \text{ momentum} \quad \frac{\partial(\rho v)}{\partial t} + \text{div}(\rho v \mathbf{u}) = -\frac{\partial p}{\partial y} + \text{div}(\mu \text{ grad}(v)) + S_{My} \quad (\text{A.3})$$

$$z \text{ momentum} \quad \frac{\partial(\rho w)}{\partial t} + \text{div}(\rho w \mathbf{u}) = -\frac{\partial p}{\partial z} + \text{div}(\mu \text{ grad}(w)) + S_{Mz} \quad (\text{A.4})$$

$$\text{Internal energy} \quad \frac{\partial(\rho i)}{\partial t} + \text{div}(\rho i \mathbf{u}) = -p \text{ div}(\mathbf{u}) + \text{div}(k_i \text{ grad}(T)) + \Phi + S_i \quad (\text{A.5})$$

$$\text{Eq. of state 1} \quad p = p(\rho, T) \rightarrow p = \rho RT \quad \text{for perfect gas} \quad (\text{A.6})$$

$$\text{Eq. of state 2} \quad i = i(\rho, T) \rightarrow i = C_v T \quad \text{for perfect gas} \quad (\text{A.7})$$

The momentum equations (A.2)-(A.4) yield the Navier-Stokes equations. [Versteeg and Malalasekera, 2007]

Due to the assumption of a Newtonian fluid, there is a linear relation between velocity gradients (rate of deformation) and the viscous stresses of the fluid. This relation is formed by the dynamic viscosity,  $\mu$  and a second viscosity,  $\lambda$ , describing stresses occurring from volumetric deformation. It should be noted that some small viscous stress terms, which depend on the volumetric strains, are moved to the source term  $S_M$  along with the  $\lambda$  terms, to simplify the equations. These terms are zero for an incompressible fluid.

The energy equation consists of contributions from the work done by pressure and viscous forces, as well as heat added to the fluid particle. Again viscous forces are expressed by means of the velocity gradients, due to the Newtonian fluid assumption. Furthermore, Fourier's law of heat conduction is used to express the heat flux,  $\mathbf{q}$ , as a function of the local temperature gradient,  $\mathbf{q} = -k_i \text{ grad}(T)$ . The kinetic energy has been subtracted from the specific energy to yield equation (A.5) describing

the internal energy. The kinetic energy is found by multiplying the momentum equations by the velocity component in the respective direction and sum the results. The term  $\Phi$ , describes all contributions from the viscous stresses to the internal energy.

For an incompressible fluid, the density,  $\rho$ , does not vary across the field. Consequently, the coupling between the energy equation (A.5) and the mass conservation and momentum equations (A.1)-(A.4) provided by the equations of state (A.6)-(A.7) does not occur.

By assuming that the flow problem is not affected by heat transfer, the flow field can be solved by only considering conservation of mass and momentum equations.

The assumption of steady state causes the term,  $\partial/\partial t$ , in the transport equation (A.9) to disappear, as there will be no change in properties over time.

### Transport equations

When the governing equations are in the form shown in (A.1)-(A.5), it appears that there are significant similarities. Therefore, the so-called transport equation is formulated, see equation (A.8).

$$\frac{\partial(\rho\phi)}{\partial t} + \text{div}(\rho\phi\mathbf{u}) = \text{div}(\Gamma \text{grad}(\phi)) + S_\phi \quad (\text{A.8})$$

By inserting a fluid property (e.g. 1,  $u$ ,  $v$  or  $w$ ) as  $\phi$ , a special formulation of the governing equation will appear, i.e.  $u$  will give the momentum equation in the  $x$ -direction, etc.. The terms in the governing equations which are not in common, are a part of the source term in the transport equation.  $\Gamma$  is a diffusion coefficient (dynamic viscosity,  $\mu$ , or thermal conductivity,  $k_i$ ).

The integral of equation (A.8) can be seen in equation (A.9). The volume integration of the divergence terms, can be done as a surface integration over the CV. The Gauss divergence theorem is used for the purpose [Versteeg and Malalasekera, 2007]. Thereby equation (A.9) is obtained.

$$\frac{\partial}{\partial t} \left( \int_{\text{CV}} (\rho\phi) dV \right) + \int_A \mathbf{n} \cdot (\rho\phi\mathbf{u}) dA = \int_A \mathbf{n} \cdot (\Gamma \text{grad}(\phi)) dA + \int_{\text{CV}} S_\phi dV \quad (\text{A.9})$$

These equations are essential for the finite volume method to implement the governing equations to a discretised domain of finite control volumes.

## A.2 RANS based turbulence model

Due to shear in a flow field, fluctuations and vorticity is generated, i.e. turbulence. Some of this turbulence is in the shape of turbulent eddies, which transports fluid particles between the control volumes. The same amount of mass is removed and added to a CV by the eddy motion, hence the continuity equation is satisfied. However, the particles transported by eddies can carry extra momentum, resulting in extra turbulent stresses; the so-called Reynolds stresses.

The RANS equations accounts for these extra stresses. The Reynolds decomposition defines a fluid property,  $\phi$ , as a sum of a steady mean value,  $\Phi$ , and a time dependent fluctuation value,  $\phi'$ :

$$\phi(t) = \Phi + \phi'(t) \quad (\text{A.10})$$

By substituting this formulation of the fluid properties into the momentum equations and making use of the rules controlling the time averages of fluctuating properties, extra terms containing products of the fluctuation velocities occur, see equation (A.11) for the  $x$ -momentum.

$$\frac{\partial(\rho U)}{\partial t} + \text{div}(\rho U \mathbf{U}) + \text{div}(\overline{\rho u' \mathbf{u}'}) = -\frac{\partial P}{\partial x} + \text{div}(\mu \text{grad}(U)) + S_{Mx} \quad (\text{A.11})$$

In the  $y$ - and  $z$ -momentum equations,  $u'$  would be replaced by  $v'$  and  $w'$  respectively. The new terms in the momentum equations are the Reynolds stresses and give rise to six new unknowns, e.g.  $\tau_{xy} = \tau_{yx} = -\overline{\rho u' v'}$ .

To compute the Reynolds stresses an expression formed by Boussinesq is used. The approach for this expression is that the Reynolds stresses is proportional to the average rates of deformation of the fluid element, see equation (A.12).

$$\tau_{ij} = -\overline{\rho u'_i u'_j} = \mu_t \left( \frac{\partial U_i}{\partial x_j} + \frac{\partial U_j}{\partial x_i} \right) - \frac{2}{3} \rho k \delta_{ij} \quad (\text{A.12})$$

The equation is shown in tensor notation, meaning  $i$  or  $j$  can equal 1, 2 or 3 referring to the  $x$ -,  $y$ - or  $z$ -direction respectively. The second term having  $\delta_{ij}$ , the Kronecker delta, ensures that the sum of the normal stresses are physically correct, by being equal to minus twice the amount of turbulent kinetic energy,  $k$ , per unit volume. It is here assumed that these normal stresses are isotropic. Furthermore, the turbulent viscosity,  $\mu_t$  is also assumed to be isotropic for models using the Boussinesq expression.

The  $k - \omega$  SST turbulence model is used to determine the turbulent viscosity (eddy viscosity),  $\mu_t$ , in this report. The model is a combination of two acclaimed turbulence models, namely the  $k - \varepsilon$  and  $k - \omega$  models. The  $k - \omega$  model is used close to the wall in the viscous-sub layer and the log-layer, and is known for its good predictions of the mean flow profiles for simple definitions of the boundary conditions and its numerical stability. However the  $k - \omega$  is very sensitive to the choice of freestream value for  $\omega$  far from the wall, why the  $k - \varepsilon$  is used in this region. These models add two extra transport equations to every CV in the computational domain. One for the kinetic energy,  $k$ , and one for the dissipation of kinetic energy which can either be from the  $k - \omega$  or the  $k - \varepsilon$  model. In the  $\varepsilon$ -equation,  $\varepsilon$  is substituted by  $\varepsilon = k\omega$ . The equations are shown in (A.13)-(A.15). [Versteeg and Malalasekera, 2007]

$$\begin{aligned}
k\text{-equation} \quad \frac{\partial \rho k}{\partial t} + \text{div}(\rho k \mathbf{U}) &= \text{div} \left( \left( \mu + \frac{\mu_t}{\sigma_k} \right) \text{grad}(k) \right) + \\
&\left( 2\mu_t S_{ij} \cdot S_{ij} - \frac{2}{3} \rho k \frac{\partial U_i}{\partial x_j} \delta_{ij} \right) - \beta^* \rho k \omega
\end{aligned} \tag{A.13}$$

$$\begin{aligned}
\omega\text{-equation} \quad \frac{\partial \rho \omega}{\partial t} + \text{div}(\rho \omega \mathbf{U}) &= \text{div} \left( \left( \mu + \frac{\mu_t}{\sigma_\omega} \right) \text{grad}(\omega) \right) + \\
\gamma_1 \left( 2\rho S_{ij} \cdot S_{ij} - \frac{2}{3} \rho \omega \frac{\partial U_i}{\partial x_j} \delta_{ij} \right) &- \beta_1 \rho k \omega^2
\end{aligned} \tag{A.14}$$

$$\begin{aligned}
\varepsilon\text{-equation} \quad \frac{\partial \rho \omega}{\partial t} + \text{div}(\rho \omega \mathbf{U}) &= \text{div} \left( \left( \mu + \frac{\mu_t}{\sigma_{\omega,1}} \right) \text{grad}(\omega) \right) + \\
\gamma_2 \left( 2\rho S_{ij} \cdot S_{ij} - \frac{2}{3} \rho \omega \frac{\partial U_i}{\partial x_j} \delta_{ij} \right) &- \beta_2 \rho \omega^2 + 2 \frac{\rho}{\sigma_{\omega,2} \omega} \frac{\partial k}{\partial x_k} \frac{\partial \omega}{\partial x_k}
\end{aligned} \tag{A.15}$$

The constants used in the equations can be found in Versteeg and Malalasekera, 2007.

The SST (shear stress transport) model accounts for the transport of the principal turbulent shear stress by reformulating the expression for  $\mu_t$ . Originally  $\mu_t = \rho k / \omega$ , but in the SST model it is given as equation (A.16). [Menter, 1994]

$$\frac{\mu_t}{\rho} = \frac{a_1 k}{\max(a_1 \omega ; \partial U / \partial y F_2)} \tag{A.16}$$

$F_2$  is equal to 1 for boundary layer flow and 0 for free shear flow.

### A.3 Near-wall region

The term  $y^+$  is widely used in this report to describe the degree of surface refinement. Equations in A.17 shows how to calculate  $y^+$  according to turbulent boundary layer flow over a flat plate.

$$y^+ = \frac{y u_\tau}{\nu}, \quad u_\tau = \sqrt{\frac{\tau_w}{\rho}}, \quad \tau_w = \frac{C_f \rho U_{ref}^2}{2}, \quad C_f = \frac{0.026}{Re_x^{1/7}}, \quad Re_x = \frac{\rho U_{ref} L}{\mu}, \quad u^+ = \frac{U}{u_\tau} \tag{A.17}$$

The turbulent boundary layer can be divided into two regions the inner region and the outer region. The inner region is 10-20 % of the boundary layer thickness closest to the wall. Viscous forces is equal or greater that the inertia forces in this region. The inner region is further subdivided in three zones in which the flow acts differently as shown in Figure A.1. The zone closest to the surface is called the viscous-sub layer, where the viscous effects are dominant and the relation between the velocity and the distance from the wall is linear i.e.  $u^+ = y^+$ . Using this expression with the

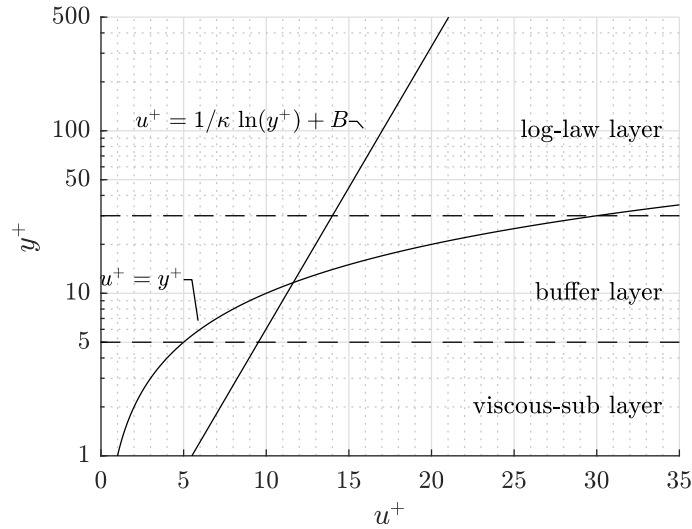


**Figure A.1:** Normalised velocity distribution near a surface.

formulas in A.17 and the fact that  $U$  and  $y$  is equal to zero at the wall, the expression for the wall shear stress yields:

$$\tau_w = \mu \frac{\Delta U}{\Delta y} \quad (\text{A.18})$$

This means that for grid with cells with centres in the viscous-sub layer the wall shear stress is determined simply by dividing the cell centre velocity parallel to the surface with the distance to the surface multiplied with the viscosity. This is not the case for the buffer layer where the viscous and the turbulent effects are of even importance and the log-law layer where the turbulent effects are dominant. The linear relation between  $U$  and  $y$  are not present for these layers, where the buffer is a transition to the logarithmic relationship in the log-law layer. If the cells at the surface has its centre in these layers, wall functions are needed to calculate the correct  $\tau_w$ . Wall functions are boundary conditions that form relations from the surface to the centre of the cells at the surface.



## B. Numerical settings

fvSchemes	
Term	Scheme
ddtSchemes	steadyState
gradSchemes	Gauss linear*
grad(U)	cellLimited Gauss linear 1
div(phi,U)	bounded Gauss linearUpwindV grad(U)*
div(phi,k)	bounded Gauss upwind
div(phi,omega)	bounded Gauss upwind
div((nuEff*dev2(T(grad(U)))))	Gauss linear
laplacianSchemes	Gauss linear corrected*
interpolationSchemes	linear
snGradSchemes	corrected*
wallDist	method meshWave

fvSolution	
Setting	Value
p solver	GAMG
p smoother	GaussSeidel
p tolerance	$10^{-7}$
p relTol	$10^{-2}$
"(U k omega)" solver	smoothSolver
"(U k omega)" smoother	GaussSeidel
"(U k omega)" tolerance	$10^{-8}$
"(U k omega)" relTol	$10^{-2}$
"(U k omega)" nSweeps	1
"(k omega)" minIter	2
SIMPLE nNonOrthogonalCorrectors	0*
SIMPLE consistent	yes
"(p U k omega)" relaxationFactors	(0.3 0.5 0.5 0.5)*

**Table B.1:** Schemes and solution settings used in this report, defined in the files `fvSchemes` and `fvSolution`. '\*' indicates that the setting is tuned for stability in the simulations for the P80, see Table B.2.

fvSchemes	
Term	Scheme
gradSchemes	cellLimited Gauss linear 1
div(phi,U)	bounded Gauss upwind
laplacianSchemes	Gauss linear limited 0.33
snGradSchemes	limited

fvSolution	
Setting	Value
SIMPLE nNonOrthogonalCorrectors	20
"(p U k omega)" relaxationFactors	(0.1 0.2 0.2 0.2)

**Table B.2:** Schemes and solution settings tuned for the P80 simulations defined in the files fvSchemes and fvSolution.

Boundary	0.orig/(U,p,k,omega,nut) Condition
inlet (U) (model scale)	fixedValue; nonuniform List<vector>
inlet (U) (full scale)	fixedValue; uniform
inlet (k,omega,nut)	fixedValue; uniform
inlet (p)	zeroGradient
outlet (U,k,omega)	inletOutlet; uniform
outlet (nut)	calculated
outlet (p)	fixedValue
walls (U,k,omega)	slip
walls (nut)	calculated
walls (p)	zeroGradient
Model (U)	noSlip
Model (p)	zeroGradient
Model (omega)	omegaWallFunction
Model (k)	kLowReWallFunction
Model (nut)	nutUBlendedWallFunction
Model (k,nut)(wallfunction off)	fixedValue; uniform 1e-20

**Table B.3:** Boundary conditions used in this report, defined in the 0.orig/ directory

## C. Flume velocity profiles

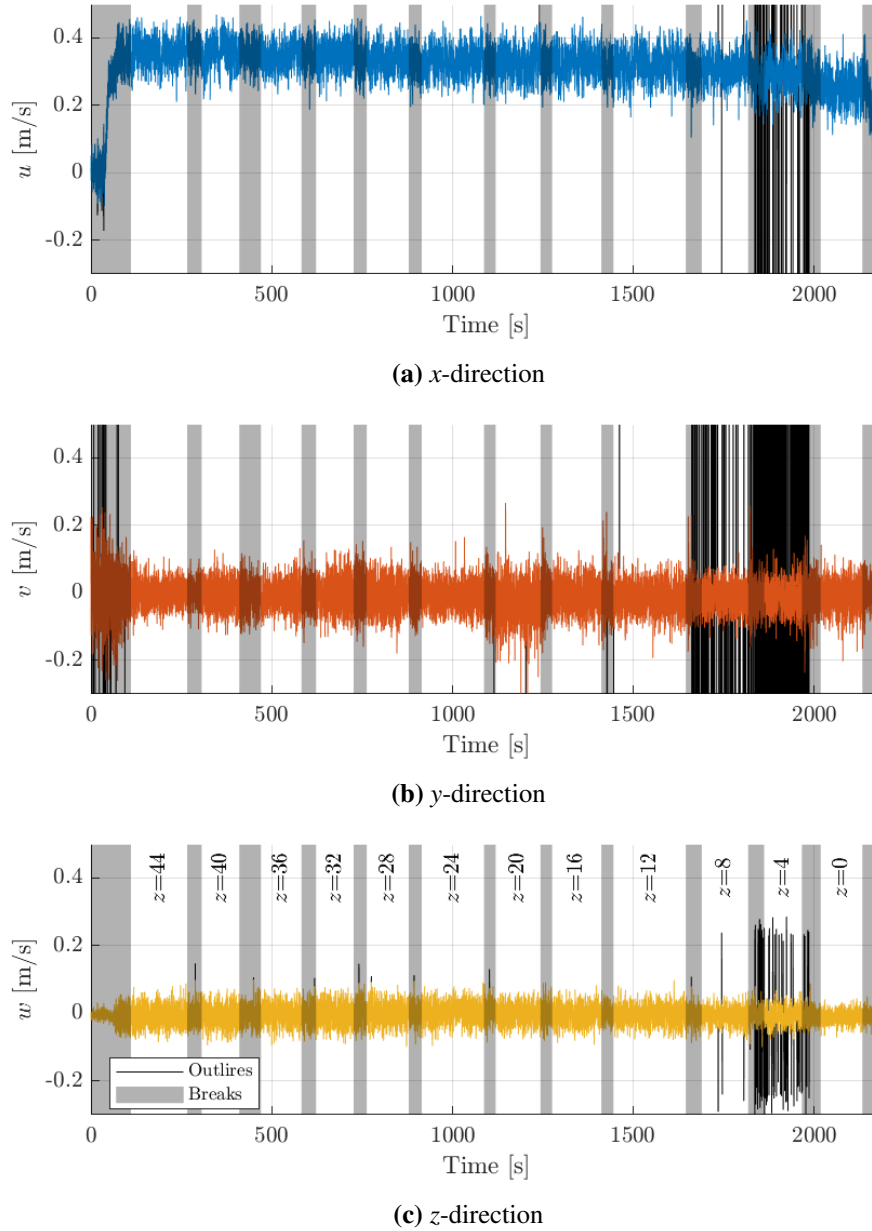
In this appendix, the velocity profiles measured in the flume at AAU are presented.

Table C.1 gives an overview of the performed experiments and shows that the majority of them have been carried out at  $x = 8$  m. This is because the small scale model testing has been performed at this location and is thereby of most interest for this project. The last three experiments were done with the flowmeter propeller.

No.	$x$ [m]	$y$ [m]	$h$ [cm]	$Q$ [%]	$U_{top}$ [m/s]
1	8	0.000	30	50	0.254
2	8	0.000	30	50	0.268
3	8	0.000	50	50	0.184
4	8	0.000	50	50	0.180
5	8	0.000	50	75	0.272
6	8	0.000	50	75	0.271
7	8	0.000	50	100	0.348
8	8	0.000	50	100	0.352
9	8	0.000	70	50	0.149
10	8	0.000	70	100	0.306
11	8	0.375	50	50	0.194
12	8	0.375	50	100	0.375
13	8	-0.375	50	50	0.189
14	8	-0.375	50	100	0.361
15	5	0.000	50	50	0.166
16	5	0.000	50	100	0.329
17	5	0.375	50	100	0.352
18	5	-0.375	50	100	0.348
19	11	0.000	50	50	0.188
20	11	0.000	50	100	0.352
21	11	0.375	50	100	0.368
22	11	-0.375	50	100	0.338
23	8	0.000	50	50	0.181
24	8	0.000	50	75	0.273
25	8	0.000	50	100	0.352

**Table C.1:** Overview of the current velocity experiments.  $x$  and  $y$  define location,  $h$  is the water depth,  $Q$  is the current generation capacity and  $U_{top}$  is the mean current velocity in the  $x$ -direction measured at the uppermost  $z$ -location (e.g. for  $h = 0.5$  m,  $U_{top}$  is mean current velocity at  $z = 0.44$  m).

In figure C.1 an example of the correction of the measured velocities in the  $x$ -  $y$ - and  $z$ -direction are present.



**Figure C.1:** Correction of the velocity measurements. Ranges of  $-0.1$  to  $0.5$  m/s,  $-0.3$  to  $0.3$  m/s and  $-0.1$  to  $0.1$  m/s are used for the  $x$ -  $y$ - and  $z$ -direction respectively. The measurements shown are for the location  $x = 8$  m,  $y = 0$  m.  $Q = 100\%$  and  $h = 0.5$  m. The measuring positions above the bottom of the flume are specified by  $z$  in cm

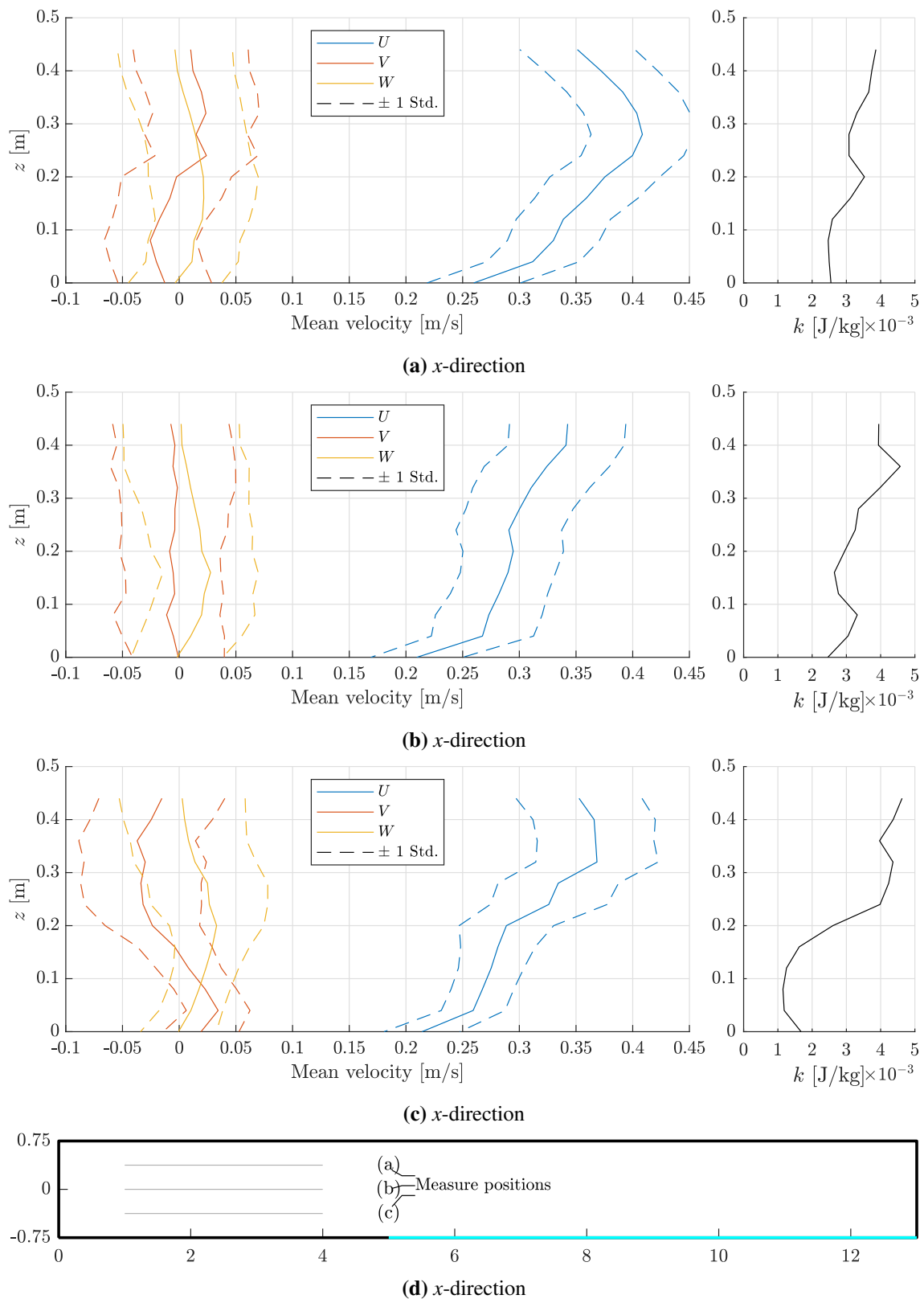


**Figure C.2:** Mean velocities  $U$ ,  $V$  and  $W$  at  $x=5$  m for three different  $y$  locations. The 68% Confidence Intervals for the velocities  $u$ ,  $v$  and  $w$  are shown as well i.e.  $\pm$  a standard derivation when assuming that the velocities are normal distributed.

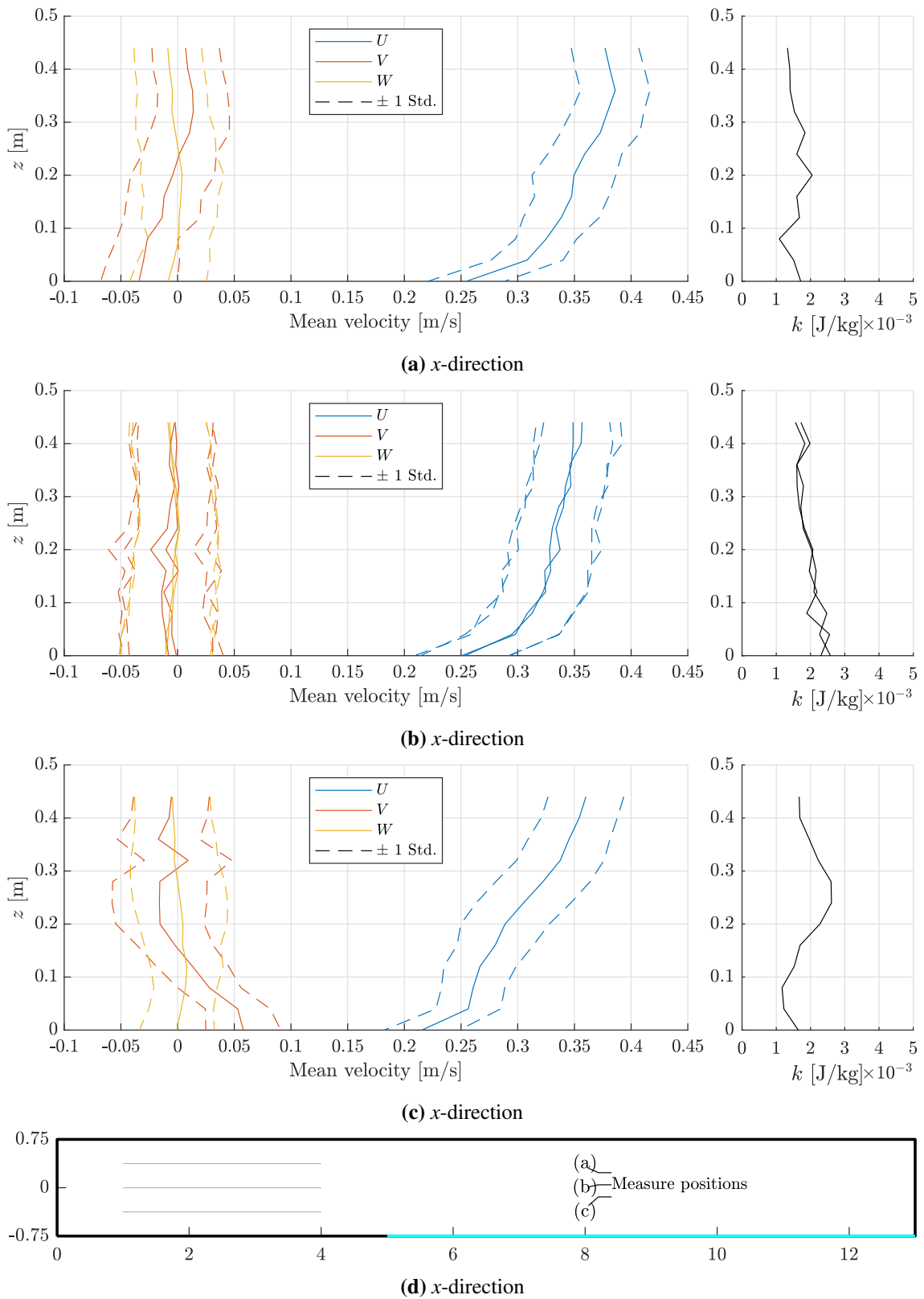


**Figure C.3:** Mean velocities  $U$ ,  $V$  and  $W$  at  $x = 8$  m for three different  $y$  locations. The 68% Confidence Intervals for the velocities  $u$ ,  $v$  and  $w$  are shown as well i.e.  $\pm$  a standard derivation when assuming that the velocities are normal distributed.

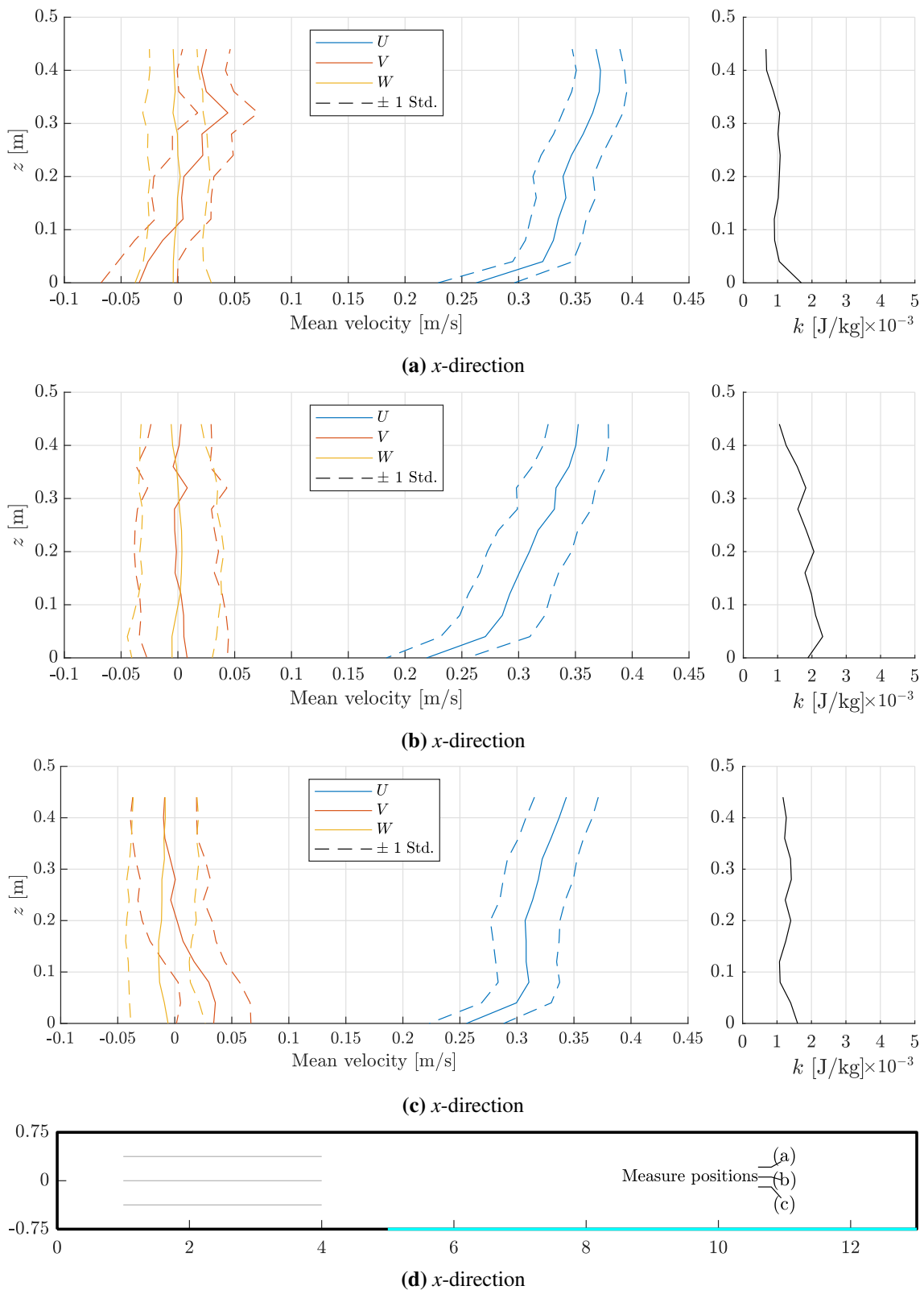


**Figure C.4:** Mean velocities  $U$ ,  $V$  and  $W$  at  $x=11$  m for three different  $y$  locations. The 68% Confidence Intervals for the velocities  $u$ ,  $v$  and  $w$  are shown as well i.e.  $\pm$  a standard deviation when assuming that the velocities are normal distributed.



## D. Force sensor

A 6-axis force/torque sensor from Schunk [Schunk, 2019] is used to measure the forces on the model. A steel plate is mounted on the sensor and holes are made in the plate every  $22.5^\circ$  with a distance of 5 cm from the plate centre to the hole centre. In this way, experiments for different orientations of the model was carried out, see Figure D.1.



**Figure D.1:** The force/torque sensor with a 1 cm thick steel plate attached to mount the model.

Along with the sensor, a calibration matrix and a vector with offset values are provided to calculate the forces from the 6 measured signals. To validate the accuracy of the sensor, tests should be performed before doing the model testing. These tests have been done with three different setups of the sensor.

- The sensor standing on the floor, having its  $z$ -direction pointing upwards. Loading it with weights of 0.5 kg, 1.0 kg and 2.0 kg
- The sensor mounted on a stand, having its  $y$ -direction pointing downwards. Loading it with weights of 0.5 kg, 1.0 kg and 2.0 kg, hanging on a bolt mounted in different holes.
- The sensor hanging in the model setup, with positive  $z$ -direction pointing downwards. Both tests with weights hanging in different locations, and newtonmeter pullings were carried out.

Some issues were detected with the force sensor, where the force in the  $z$ -direction seems to change linearly with time, despite there being a constant load applied. The slope varies between  $\pm 0,00075 \text{ N/s}$  under a constant load.

It has also been noticed that measurements for the moments around the  $x$ - and  $y$ -axis when pulling in the  $y$ - and  $x$ -directions respectively, always exceeded the calculated values. It was found that by adding 2 cm to the  $z$ -direction results became in much better compliance with the analytical calculations. From this it seems that the origin from where the sensor measures, is placed 2 cm inside the sensor in the negative  $z$ -direction. Figure D.2 shows the results from one of the tests, with the corrected  $z$ -arm.

From Figure D.2 it is found that there is a small force measured in the  $x$ -direction. This might be due to that the  $y$ -direction is not entirely vertical, but is rotated slightly clockwise, which would give rise to deviations of  $M_y$  and  $M_z$ .

---

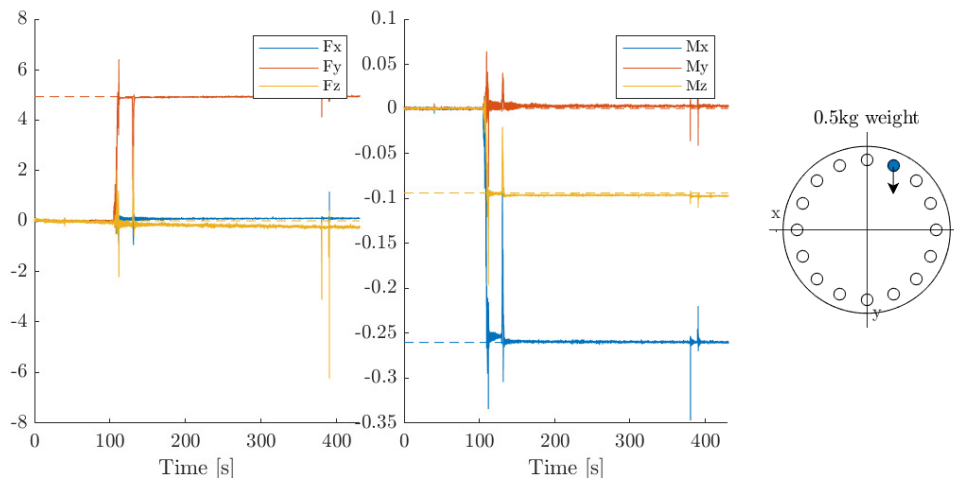


**Figure D.2:** Calibration test with the y-direction downwards, and a weight of 0.5 kg. The dotted lines are the calculated forces from the weight.

It is still chosen to work with the sensor, as changes in loads are still accurately predicted, despite the slope of  $F_z$ . Also, the small changes it would amount to in the z-direction is not destructive of the test results.

## E. Forces from experiments

Some of the experiments are not included in the results, as they contained errors due to interruptions during testing or insufficient test duration.

Forces and moments are taken as an average over the measured signal duration.

### E.1 Model Leg

Exp. no.	$\theta$ [°]	$Q$ [%]	$F_x$ [N]	$F_y$ [N]	$F_z$ [N]	$M_x$ [Nm]	$M_y$ [Nm]	$M_z$ [Nm]
5	0.0	75	0.26	0.11	-0.00	0.023	-0.088	0.002
24	0.0	75	0.27	0.11	0.04	0.027	-0.091	0.004
2	0.0	100	0.41	0.20	0.20	0.034	-0.137	0.004
4	0.0	100	0.43	0.23	0.23	0.044	-0.139	0.002
25	0.0	100	0.43	0.20	0.17	0.044	-0.142	0.004
16	22.5	75	0.73	-0.53	-0.15	-0.139	-0.228	0.045
17	22.5	75	0.73	-0.55	-0.10	-0.144	-0.229	0.046
6	22.5	100	1.12	-1.20	0.01	-0.302	-0.335	0.091
18	22.5	100	1.15	-1.15	-0.08	-0.279	-0.341	0.088
9	45.0	75	1.20	-0.65	-0.81	-0.166	-0.373	0.043
20	45.0	75	1.19	-0.65	-0.78	-0.168	-0.370	0.041
8	45.0	100	2.10	-1.20	-1.10	-0.294	-0.614	0.072
19	45.0	100	2.11	-1.17	-1.16	-0.284	-0.618	0.073
22	67.5	75	1.97	-0.57	-1.55	-0.153	-0.574	0.028
23	67.5	75	1.97	-0.57	-1.54	-0.153	-0.574	0.028
10	67.5	100	3.45	-1.02	-2.33	-0.258	-0.947	0.049
11	67.5	100	3.38	-1.00	-2.33	-0.253	-0.934	0.049
14	90.0	75	2.24	0.00	-1.95	-0.011	-0.643	-0.005
15	90.0	75	2.24	0.01	-1.88	-0.011	-0.643	-0.005
12	90.0	100	3.98	0.01	-2.89	-0.016	-1.079	-0.009
13	90.0	100	3.92	0.01	-2.86	-0.018	-1.062	-0.010

**Table E.1:** Forces for each experiment on Model Leg. Exp. no.: Experiment number.  $Q$ : Current generation capacity.

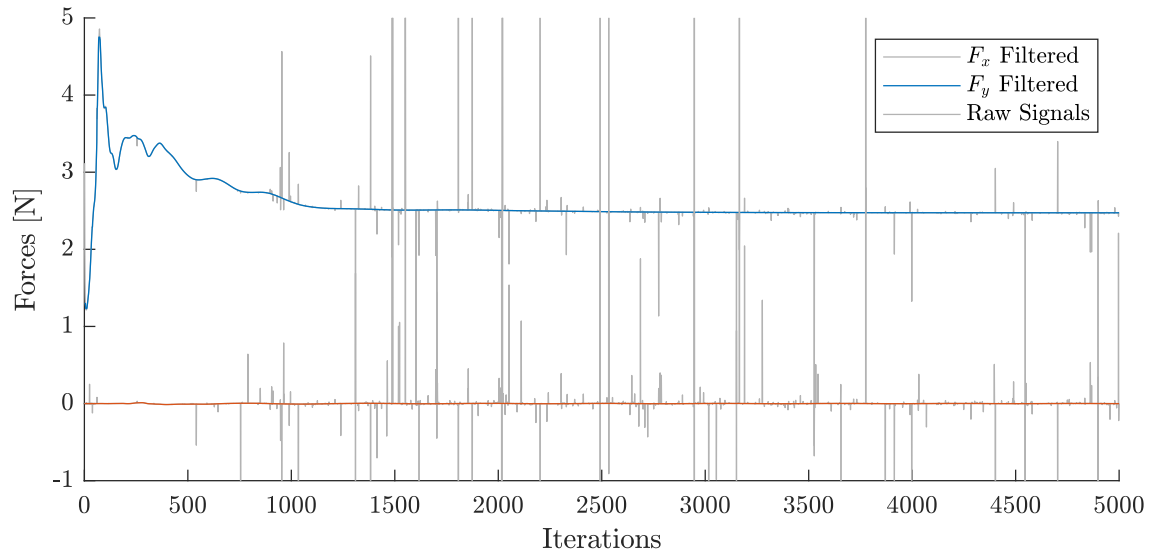
## E.2 Full Model

Exp. no.	$\theta$ [°]	$Q$ [%]	$F_x$ [N]	$F_y$ [N]	$F_z$ [N]	$M_x$ [Nm]	$M_y$ [Nm]	$M_z$ [Nm]
1	0.0	100	6.69	0.00	-18.17	-0.117	-0.178	0.025
2	0.0	100	6.72	0.00	-18.08	-0.110	-0.187	0.027
3	0.0	100	6.71	-0.02	-18.13	-0.108	-0.191	0.023
4	22.5	100	11.12	-9.21	-14.11	-4.311	-2.795	1.083
5	22.5	100	11.08	-9.16	-14.84	-4.296	-2.817	1.083
7	45.0	100	16.75	-9.48	-12.26	-5.481	-5.252	1.173
8	45.0	100	16.79	-9.43	-12.44	-5.505	-5.301	1.212
9	45.0	100	16.79	-9.38	-12.05	-5.506	-5.278	1.205
10	67.5	100	24.55	-4.52	-13.62	-5.424	-8.571	-1.050
11	67.5	100	24.24	-4.45	-13.41	-5.366	-8.410	-1.056
12	90.0	100	25.49	1.98	-13.66	-3.531	-11.001	-1.336
13	90.0	100	25.31	2.03	-13.67	-3.527	-10.892	-1.367
14	90.0	100	25.11	2.02	-13.68	-3.496	-10.865	-1.358

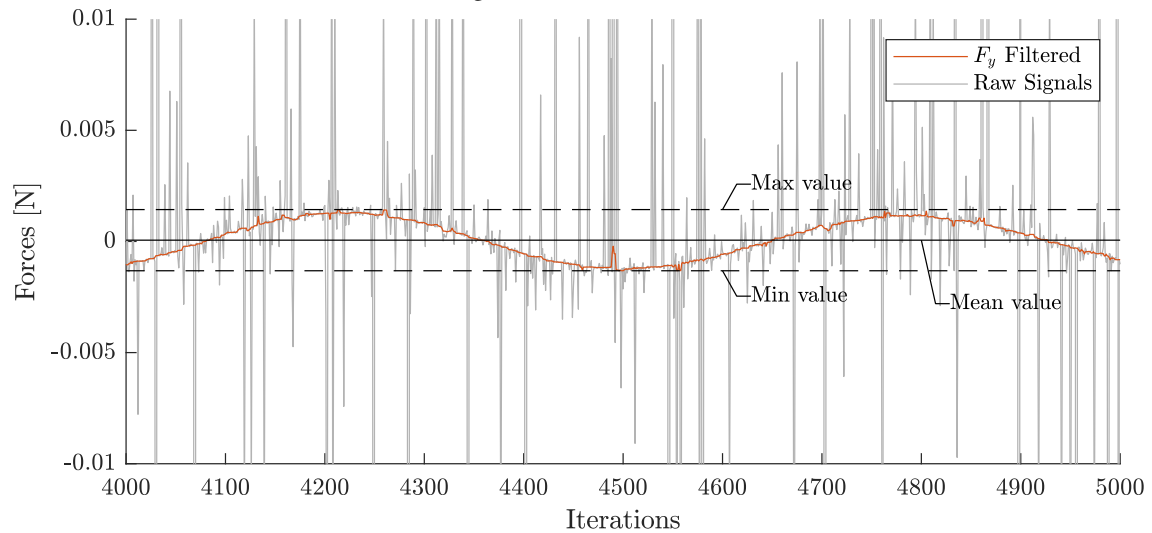
**Table E.2:** Forces for each experiment on Full Model. Exp. no.: Experiment number.  $Q$ : Current generation capacity.

## F. Simulation results

In this Appendix, all results of simulations are presented. The results of each force and moment in the simulations are first filtered to remove unphysical peaks, see Figure F.1(a). Thereafter, the final results shown in the tables are calculated as the average between the max and min value in the last 1000 iterations of the simulation, see Figure F.1(b).



(a) Filtering of simulated force iterations.



(b) Representative value of simulation, calculated as the mean of the max and min of the last 1000 iterations.

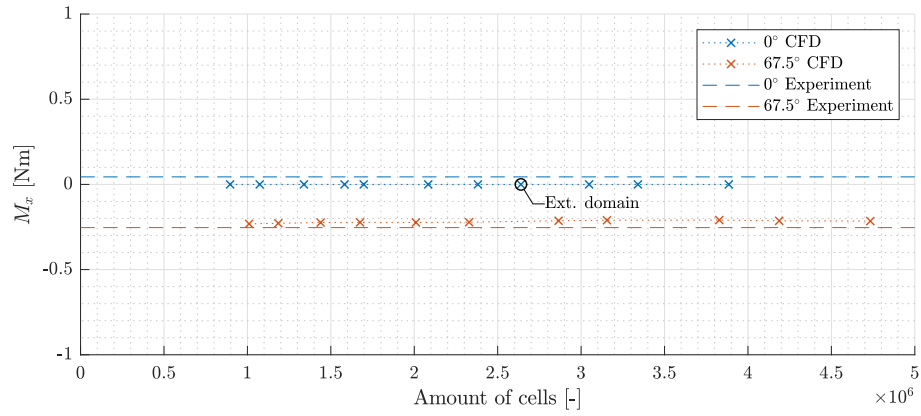
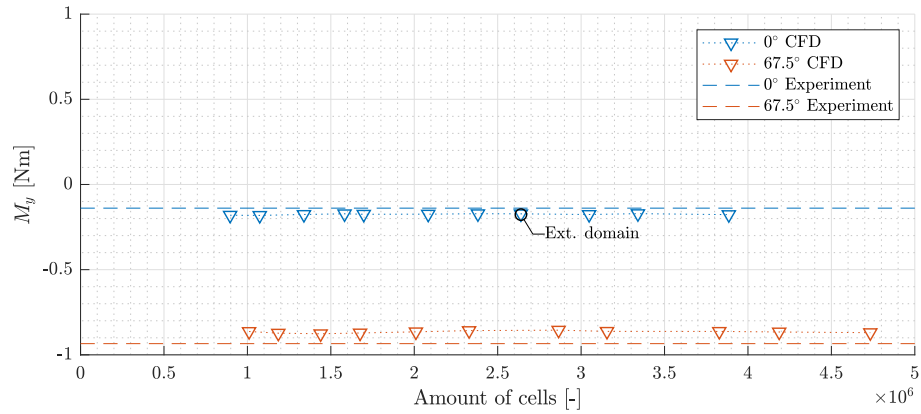
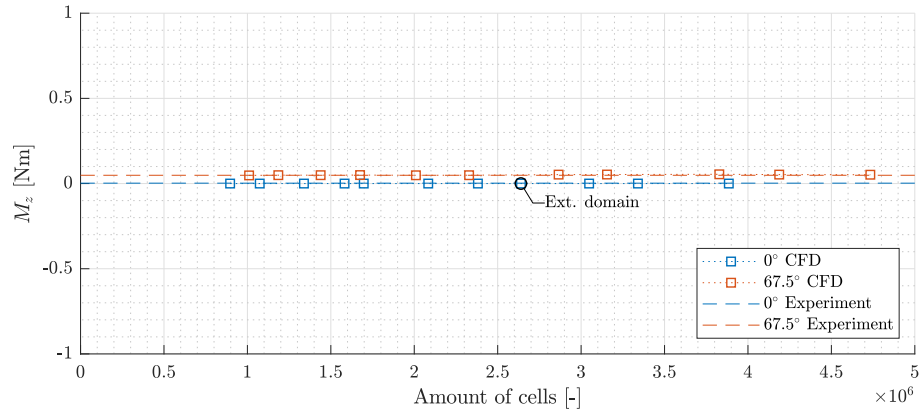
**Figure F.1:** Results shown are for Model Leg experimental comparison simulation with  $Q = 75\%$  and  $90^\circ$  orientation.

## F.1 Model Leg results

### F.1.1 Convergence analysis

$N$	$\theta$ [°]	$F_x$ [N]	$F_y$ [N]	$F_z$ [N]	$M_x$ [Nm]	$M_y$ [Nm]	$M_z$ [Nm]
10	0.0	0.51	0.00	-0.04	0.000	-0.180	-0.000
11	0.0	0.51	-0.00	-0.04	-0.000	-0.182	0.000
12	0.0	0.49	-0.00	-0.04	-0.000	-0.176	0.000
13	0.0	0.48	0.00	-0.03	0.000	-0.172	-0.000
14	0.0	0.49	-0.00	-0.03	-0.000	-0.175	0.000
15	0.0	0.49	0.00	-0.04	0.000	-0.174	-0.000
16	0.0	0.48	0.00	-0.04	0.000	-0.172	-0.000
17	0.0	0.48	-0.00	-0.04	-0.000	-0.172	-0.000
18	0.0	0.49	-0.00	-0.04	-0.000	-0.176	0.000
19	0.0	0.48	0.00	-0.03	0.000	-0.171	-0.000
20	0.0	0.49	-0.00	-0.03	-0.000	-0.177	-0.000
10	67.5	3.09	-1.01	-2.63	-0.232	-0.863	0.048
11	67.5	3.14	-1.00	-2.66	-0.228	-0.873	0.049
12	67.5	3.15	-0.99	-2.68	-0.224	-0.876	0.049
13	67.5	3.13	-0.98	-2.68	-0.223	-0.872	0.050
14	67.5	3.10	-0.98	-2.68	-0.223	-0.865	0.049
15	67.5	3.07	-0.97	-2.66	-0.222	-0.858	0.049
16	67.5	3.08	-0.94	-2.68	-0.213	-0.855	0.053
17	67.5	3.10	-0.93	-2.69	-0.210	-0.862	0.053
18	67.5	3.10	-0.92	-2.70	-0.209	-0.863	0.054
19	67.5	3.10	-0.93	-2.72	-0.214	-0.866	0.053
20	67.5	3.13	-0.95	-2.71	-0.215	-0.870	0.052

**Table F.1:** Convergence analysis for Model Leg results.

(a)  $M_x$ (b)  $M_y$ (c)  $M_z$ **Figure F.2:** Convergence of moments Model Leg for  $0^\circ$  and  $67.5^\circ$ .

## F.1.2 Sensitivity analysis

$k$ [m <sup>2</sup> /s <sup>2</sup> ]	$\omega$ [s <sup>-1</sup> ]	$\theta$ [°]	$F_x$ [N]	$F_y$ [N]	$F_z$ [N]	$M_x$ [Nm]	$M_y$ [Nm]	$M_z$ [Nm]
1e-12	0.1	0.0	0.44	-0.01	0.00	-0.002	-0.159	-0.000
1e-08	1	0.0	0.44	0.01	0.00	0.001	-0.159	0.000
1e-03	1.17	0.0	0.46	-0.00	-0.03	-0.000	-0.165	-0.000
2e-03	1.66	0.0	0.48	-0.00	-0.04	-0.000	-0.172	-0.000
3e-03	2.03	0.0	0.50	-0.00	-0.05	-0.000	-0.178	-0.000
1e-12	0.1	67.5	3.01	-0.89	-2.68	-0.195	-0.834	0.053
1e-08	1	67.5	3.01	-0.89	-2.68	-0.195	-0.834	0.053
2e-03	1.66	67.5	3.10	-0.93	-2.69	-0.210	-0.862	0.053

Table F.2: Turbulence parameters variation, Model Leg.

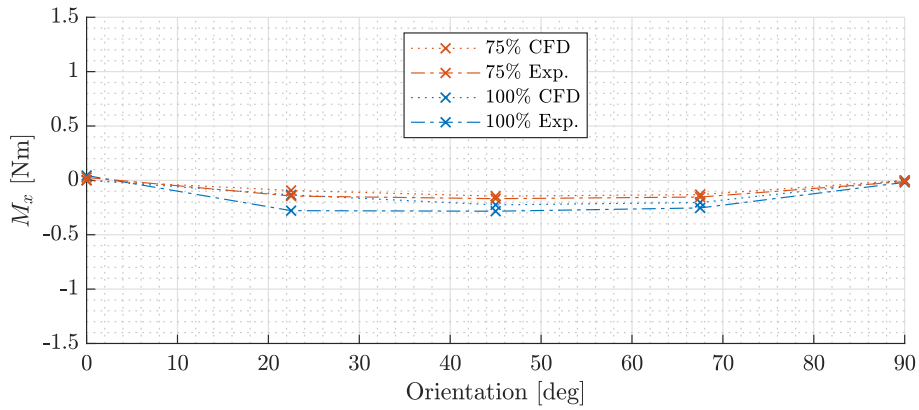
Profile	$\theta$ [°]	$F_x$ [N]	$F_y$ [N]	$F_z$ [N]	$M_x$ [Nm]	$M_y$ [Nm]	$M_z$ [Nm]
Plug - slip	0.0	0.48	-0.00	-0.04	-0.000	-0.172	-0.000
Plug - no slip	0.0	1.05	0.00	1.05	0.000	-0.339	0.000
Profile - slip	0.0	0.50	-0.00	-0.04	-0.000	-0.178	-0.000

Table F.3: Velocity profile variation, Model Leg.

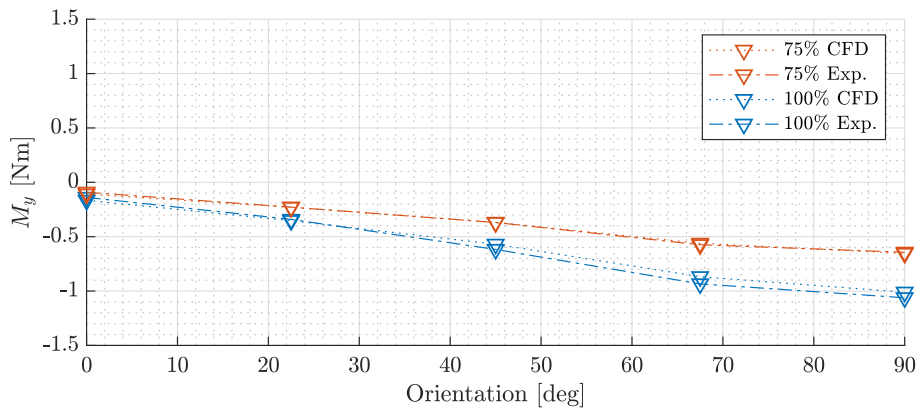
Wall on/off	$y^+$	$\theta$ [°]	$F_x$ [N]	$F_y$ [N]	$F_z$ [N]	$M_x$ [Nm]	$M_y$ [Nm]	$M_z$ [Nm]
On	1	67.5	3.16	-0.94	-2.76	-0.204	-0.868	0.055
On	10	67.5	3.10	-0.94	-2.74	-0.205	-0.855	0.054
On	20	67.5	3.09	-0.84	-2.74	-0.182	-0.853	0.060
On	39	67.5	2.99	-0.96	-2.67	-0.211	-0.829	0.051
On	79	67.5	2.70	-0.85	-2.36	-0.181	-0.752	0.060
On	157	67.5	2.84	-0.55	-2.26	-0.114	-0.789	0.063
Off	1	67.5	3.16	-0.94	-2.76	-0.204	-0.868	0.055
Off	10	67.5	3.10	-0.94	-2.74	-0.206	-0.854	0.054
Off	20	67.5	3.08	-0.85	-2.74	-0.182	-0.852	0.061
Off	39	67.5	2.99	-0.97	-2.68	-0.213	-0.828	0.052
Off	79	67.5	2.68	-0.84	-2.36	-0.182	-0.746	0.060
Off	157	67.5	2.82	-0.55	-2.29	-0.116	-0.781	0.064

Table F.4: Wall function on/off and  $y^+$  variation, Model Leg.

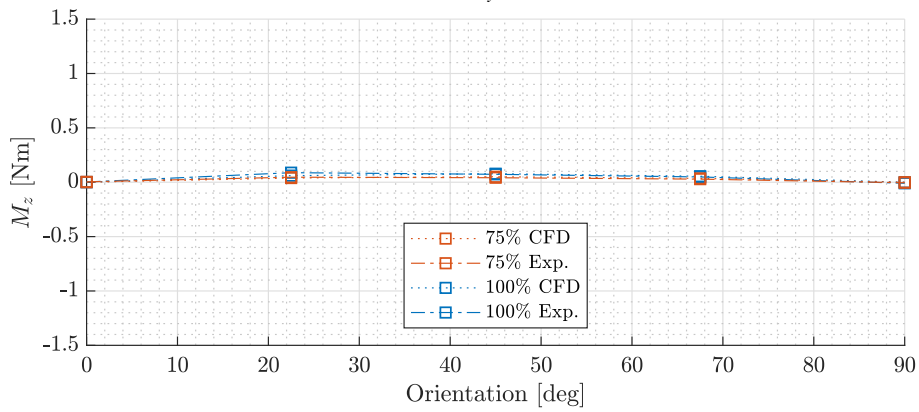
F.1.3 Experiment comparisons



(a)  $M_x$



(b)  $M_y$



(c)  $M_z$

**Figure F.3:** Experimental and CFD results of moments for currents equal to the experimental current generation capacity of 75 % and 100 %, and five orientations of the Model Leg.

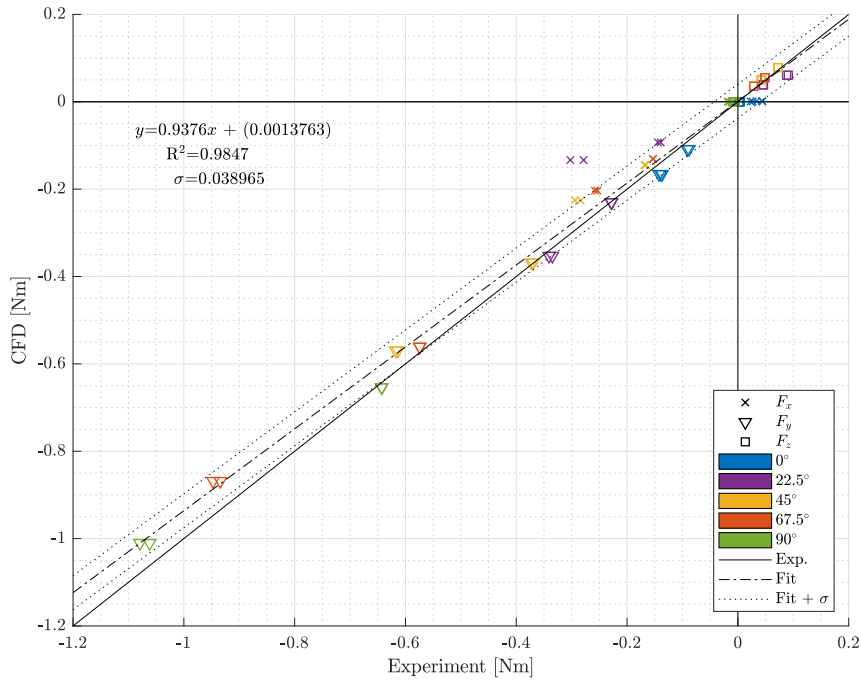


**Figure F.4:** All scenarios' moments results from experiments vs. CFD analysis for Model Leg.

$\theta$ [°]	$Q$ [%]	$F_x$ [N]	$F_y$ [N]	$F_z$ [N]	$M_x$ [Nm]	$M_y$ [Nm]	$M_z$ [Nm]
0.0	75	0.30	0.00	0.00	0.001	-0.108	0.000
22.5	75	0.70	-0.37	-0.35	-0.093	-0.230	0.039
45.0	75	1.23	-0.61	-1.04	-0.145	-0.368	0.051
67.5	75	2.04	-0.60	-1.78	-0.131	-0.561	0.036
90.0	75	2.47	-0.00	-1.86	-0.000	-0.654	0.000
0.0	100	0.46	0.00	0.01	0.001	-0.166	0.000
22.5	100	1.07	-0.53	-0.53	-0.133	-0.353	0.061
45.0	100	1.90	-0.95	-1.60	-0.225	-0.570	0.078
67.5	100	3.16	-0.94	-2.76	-0.204	-0.868	0.055
90.0	100	3.82	0.00	-2.91	0.000	-1.010	-0.000

**Table F.5:** Model Leg final results for all directions.

## F.2 Full Model results

### F.2.1 Convergence analysis

$N$	$\theta$ [°]	$F_x$ [N]	$F_y$ [N]	$F_z$ [N]	$M_x$ [Nm]	$M_y$ [Nm]	$M_z$ [Nm]
15	0.0	7.08	-0.02	-20.49	-0.009	-1.817	-0.003
15e	0.0	7.04	0.02	-20.50	0.007	-1.811	0.004
16	0.0	7.13	0.00	-20.53	-0.000	-1.822	-0.006

**Table F.6:** Convergence analysis Full Model.

### F.2.2 Transient analysis

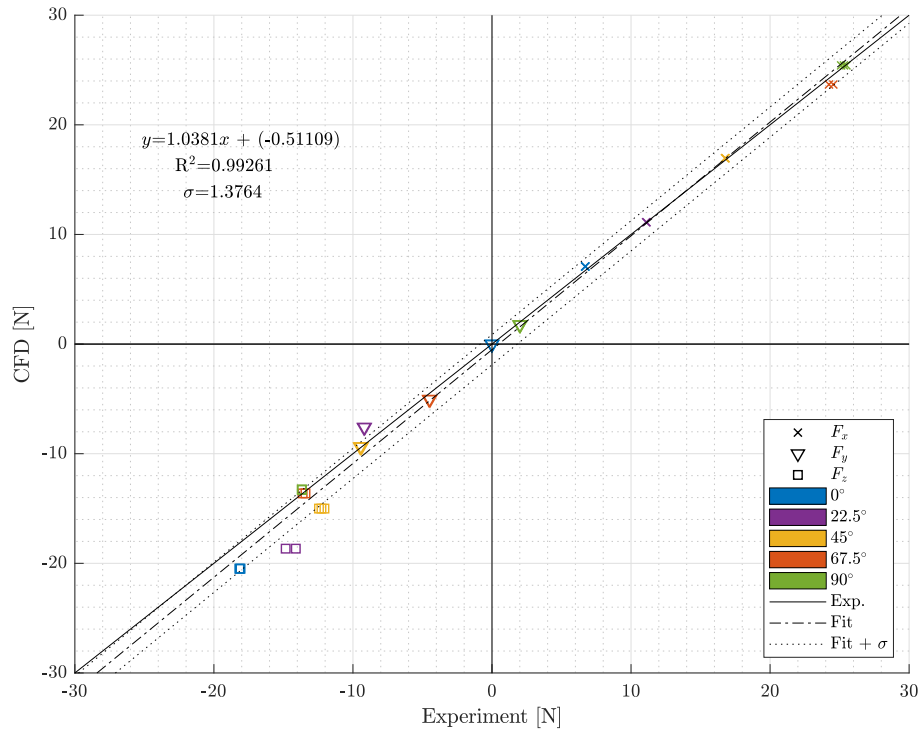
State	$F_x$ [N]	$F_y$ [N]	$F_z$ [N]	$M_x$ [Nm]	$M_y$ [Nm]	$M_z$ [Nm]
Steady	7.66	0.09	-19.38	0.017	-1.832	-0.019
Transient	7.31	0.01	-18.92	0.007	-1.761	0.010

**Table F.7:** Transient analysis Full Model with  $Q = 100\%$  at  $0^\circ$ .

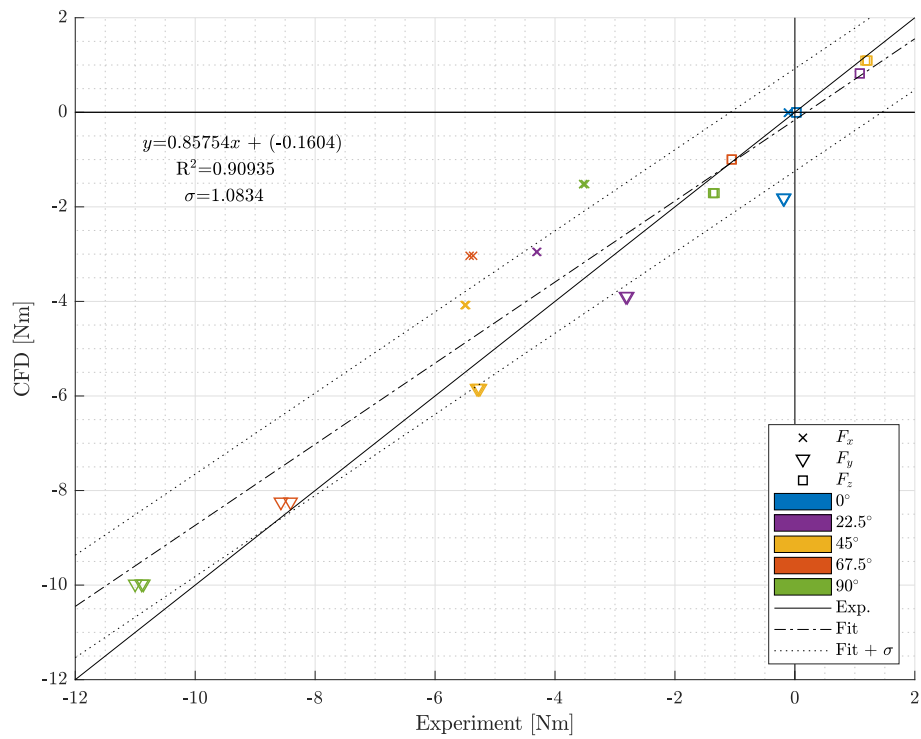
### F.2.3 Experiment comparisons

$\theta$ [°]	$F_x$ [N]	$F_y$ [N]	$F_z$ [N]	$M_x$ [Nm]	$M_y$ [Nm]	$M_z$ [Nm]
0.0	7.08	-0.02	-20.49	-0.009	-1.817	-0.003
22.5	11.12	-7.59	-18.66	-2.953	-3.894	0.822
45.0	16.95	-9.37	-15.01	-4.078	-5.839	1.094
67.5	23.68	-5.04	-13.62	-3.035	-8.242	-0.998
90.0	25.42	1.76	-13.28	-1.519	-9.977	-1.710

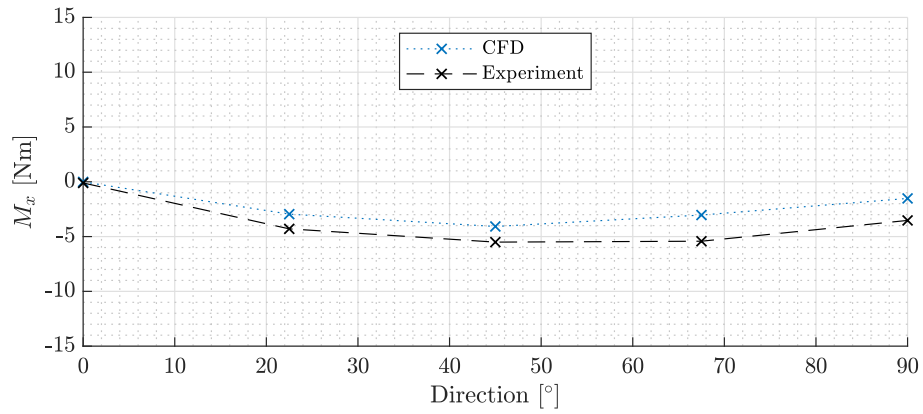
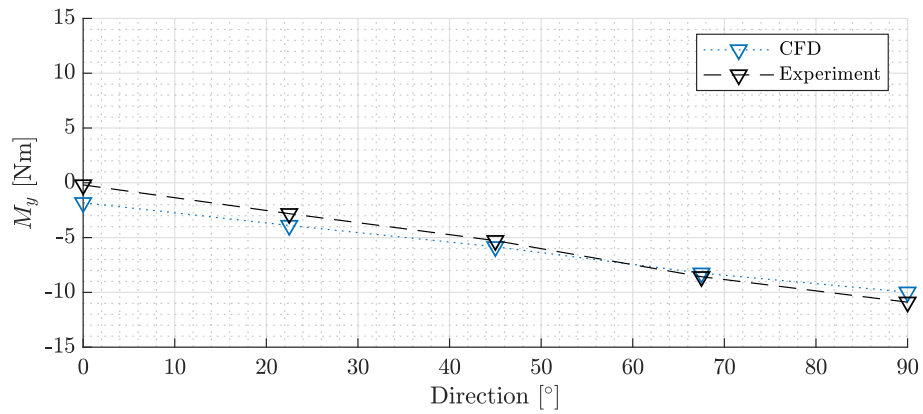
**Table F.8:** Full Model final results for all directions.



**Figure F.5:** Correlation between forces from experiments and CFD analysis for Full Model.



**Figure F.6:** All scenarios' moments results from experiments vs. CFD analysis for Full Model.

(a)  $M_x$ (b)  $M_y$ 

**Figure F.7:** Experimental and CFD results of moments for a current equal to the experimental current generation capacity of  $Q = 100\%$ , and five orientations of the Full Model.



# G. Drag coefficients from DNV

In this appendix, drag coefficients for comparison with the FPP Model Leg, Full Model and Full Scale FPP are determined. Only drag coefficients in the  $x$ -directions are calculated,  $C_{D,x}$ .

## G.1 Model Leg

Chosen drag coefficients from Det Norske Veritas, 2010 are estimated for a rough comparison of the Model Leg results. The purpose of this comparison is to determine whether drag coefficients determined in Det Norske Veritas, 2010 can be used to give a rough estimate of the forces acting on a structure of similar, though not exact, resemblance to the cases in Appendix E of Det Norske Veritas, 2010.

The forces are calculated from the following equation and values in Table G.1.

$$F_x = 0.5\rho C_{D,x} D u^2 z \quad (\text{G.1})$$

As only a rough comparison is performed, only the length and width of the web of the leg are used.

The value of  $C_{D,x}$  from the lengths  $L$  and  $D$  are what will be determined from the recommended values in Det Norske Veritas, 2010, and the calculated forces are compared to experimental results. The lengths are determined for each case depending on the orientation of the Model Leg.

Constant	Symbol	Value
Density of water	$\rho$	1000 kg/m <sup>3</sup>
Velocity	$u$	0.35 m/s
Height of leg	$z_L$	0.267 m
Length of web of leg	$l$	0.165 m
Width of web of leg	$w$	0.06 m

**Table G.1:** Values used in this appendix.

The outtakes from Det Norske Veritas, 2010 shown in Figure G.1 are chosen as they are judged to resemble the Model Leg the most.

The results of the calculated drag coefficients and forces in the  $x$ -direction,  $F_x$ , for each case are shown in Table G.2.

Case 4. Rectangle with rounded corners, is in these calculations calculated with non-rounded corners ( $R/D=0$ ). As the Model Leg does not have sharp right angles, it is a simplification from which it is expected that the drag coefficients are larger than in the experiment and CFD results. This proves also to be the case.

Case 7. Rounded nose section, is a fine estimation of the shape of the Model Leg at  $0^\circ$  on the front side, but would cause more separation and therefore a slightly higher drag than results for the Model Leg.

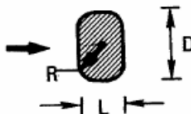
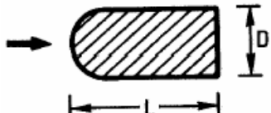
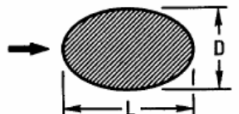
4. Rectangle with rounded corners 	L/D	R/D	$C_D$	L/D	R/D	$C_D$
	0.5	0	2.5	2.0	0	1.6
		0.021	2.2		0.042	1.4
0.083		1.9	0.167		0.7	
0.250		1.6	0.50		0.4	
1.0	0	2.2	6.0	0	0.89	
	0.021	2.0		0.5	0.29	
	0.167	1.2				
	0.333	1.0				
$Re \sim 10^5$						
7. Rounded nose section 	L/D			$C_D$		
	0.5			1.16		
1.0			0.90			
2.0			0.70			
4.0			0.68			
6.0			0.64			
8. Thin flat plate normal to flow 	$C_D = 1.9, Re > 10^4$					
14. Ellipse 	D/L			$C_D (Re \sim 10^5)$		
	0.125			0.22		
0.25			0.3			
0.50			0.6			
1.00			1.0			
2.0			1.6			

Figure G.1: Chosen cases from Det Norske Veritas, 2010.

No.	$\theta$ [°]	$D$ [m]	$L$ [m]	$L/D^*$ [-]	Re [-]	$C_{D,x}$ [-]	$F_x$ [N]
4	0	$w$	$l$	2.75	21000	1.47	1.44
4	90	$l$	$w$	0.36	57750	2.5	6.75
7	0	$w$	$l$	2.75	21000	0.69	0.68
8	90	$l$			57750	1.9	5.13
14	0	$w$	$l$	0.36*	21000	0.45	0.44
14	90	$l$	$w$	2.75*	57750	1.75	4.72
Exp.	0						0.43
Exp.	90						3.95
CFD	0						0.46
CFD	90						3.82

Table G.2: Values used in each drag case. Values marked with '\*' in the  $L/D$  column are  $D/L$ .

Case 8. Thin flat plate normal to flow, is a rough representation of the Model Leg at  $90^\circ$ , and also yields a higher drag, as the Model Leg is slightly more streamlined than a simple flat plate.

Case 14. Ellipse is the drag case that seems to fit the results best. In comparison to the other two cases, the Ellipse takes into account that the back of the Model Leg is more streamlined than a simple square, and geometrically resembles the Model Leg better than the other cases, wherefore the closest results have also been obtained for this case. It should be noted that the drag coefficient for the  $90^\circ$  orientation is estimated based on the tendencies of the increase in value in the given  $D/L$  relations, where  $0^\circ$  orientation was linearly interpolated.

## G.2 Full Model

For the Full Model and the Full Scale FPP, inspiration has been taken from Thomsen, Ferri, and Kofoed, 2017 in order to estimate a drag coefficient. The Full Model is divided into smaller parts, which resemble the shapes of DNV cases from Figure G.1.

It was found in the previous section that the legs resemble an ellipse quite well, wherefore they are represented by same. The rounded nose case is well equipped to represent the same part on the Full Model, and the whole shelf is for simplicity represented as a rectangle. Figure G.2a shows the submerged part of the Full Model, and Figure G.2b shows the Full Model with DNV-parts applied.

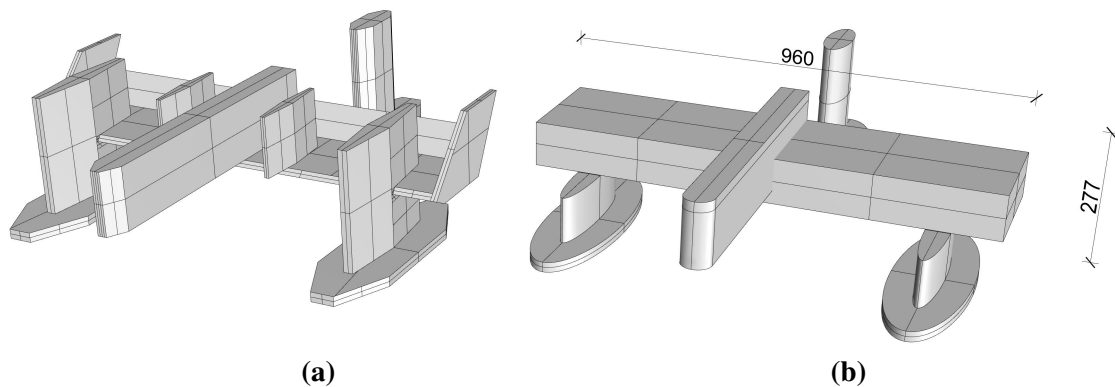


**Figure G.2:** Full Model divided into parts resembling cases from Det Norske Veritas, 2010. [Thomsen, Ferri, and Kofoed, 2017]

The values used to calculate  $F_x$  on each part are shown in Table G.3.

The  $C_{D,x}$ -value in the table for the shelves have been corrected by a reduction factor of 0.8, as the ends fully abut onto another surface. [Det Norske Veritas, 2010, Table 6.2]

As it is seen from Table G.3, the sum of the forces on the different parts is overestimated when compared to the experimental and CFD results by a factor 1.5-1.6. This was expected, as the geometry of the parts of the Full Model deviates from the cases in Det Norske Veritas, 2010, and also the interaction between parts is only partially taken into consideration.

The drag coefficient for the whole model is calculated based on a weighting of the drag coefficients of the different parts,  $C_{D,x_i}$ , with their respective areas,  $A_i = D_i z_i$ . The reference

Part	Case	$n$ [-]	$D_i$ [m]	$L_i$ [m]	$z_i$ [m]	$(L/D)_i$ [-]	$C_{D,x_i}$ [-]	$F_{x,i}$ [N]
Back leg bottom	14	1	0.160	0.377	0.021	0.42*	0.51	0.10
Back leg web	14	1	0.060	0.165	0.256	0.36*	0.44	0.41
Front leg bottom	14	2	0.160	0.485	0.021	0.33*	0.40	0.16
Front leg web	14	2	0.049	0.263	0.098	0.19*	0.24	0.14
Shelf	4	2	0.450	0.293	0.094	0.65	1.84	9.53
Nose	7	1	0.060	0.660	0.130	11.00	0.64	0.31
$\sum_{i=1}^N$								10.66
Experiment								6.71
CFD								7.08

**Table G.3:** Drag on parts of Full Model. Case is reference to case from Det Norske Veritas, 2010 and  $n$  is amount of the type of parts. Values marked with '\*' in the  $L/D$  column are  $D/L$ .

area,  $A_{ref} = 0.96 \text{ m} \cdot 27.7 \text{ m} = 0.266 \text{ m}^2$ , that will be used will however be a simplified frontal area, i.e. the total width multiplied by the submerged depth.

$$C_{D,x} = \frac{\sum_{i=1}^N (C_{D,x_i} A_i)}{A_{ref}} \quad (\text{G.2})$$

From this equation  $C_{D,x} = 0.66$  for  $A_{ref} = 0.266 \text{ m}^2$  for the Full Model.

### G.3 Full Scale FPP

The drag coefficient for the Full Scale FPP is determined in the same way as for the Full Model. The Full Scale FPP is divided into parts as shown in Figure 7.9. Values to determine  $F_x$  on each part are shown in Table G.4.

Part	Case	$n$ [-]	$D_i$ [m]	$L_i$ [m]	$z_i$ [m]	$(L/D)_i$ [-]	$C_{D,i}$ [-]	$F_{x,i}$ [kN]
Back leg bottom	4	1	12.0	25.0	4.0	2.08	1.60	39.4
Back leg web	4	1	7.0	14.0	20.0	2.00	1.60	114.8
Front leg bottom	4	2	12.0	30.0	4.0	2.50	1.51	74.3
Front leg web	4	2	3.5	25.0	7.0	7.14	0.89	22.4
Shelf + Floaters	14	2	38.0	19.5	13.0	0.51	2.00	1012.7
Nose	4	1	7.0	18.8	13.0	2.69	0.64	29.8
$\sum_{i=1}^N$								1293.4
CFD								1059.0

**Table G.4:** Drag on parts of Full Scale FPP. Case is reference to case from Det Norske Veritas, 2010 and  $n$  is amount of the type of parts.

Equation (G.2) is once again used with  $A_{ref} = 2364 \text{ m}^2$  to obtain  $C_{D,tot} = 1.07$  for the Full Scale FPP.





**AALBORG UNIVERSITET**  
STUDENTERRAPPORT